GFZ

Helmholtz-Zentrum
POTSDAM

HELMHOLTZ-ZENTRUM POTSDAM
DEUTSCHES
GEOFORSCHUNGSZENTRUM

Maximilian Semmling

Altimetric Monitoring of Disko Bay using Interferometric GNSS Observations on L1 and L2

Scientific Technical Report STR12/04

www.gfz-potsdam.de

HELMHOLTZ
GEMEINSCHAFT

Imprint

Helmholtz Centre Potsdam
GFZ German Research Centre for Geosciences

Telegrafenberg
D-14473 Potsdam

Printed in Potsdam, Germany
June 2012

ISSN 1610-0956

DOI: 10.2312/GFZ.b103-12049
URN: urn:nbn:de:kobv:b103-12049

This work is published in the GFZ series
Scientific Technical Report (STR)
and electronically available at GFZ website
www.gfz-potsdam.de > News > GFZ Publications

Altimetric Monitoring of Disko Bay using Interferometric GNSS Observations on L1 and L2

vorgelegt von
Diplom-Physiker
Maximilian Semmling
aus Görlitz

Von der Fakultät VI - Planen Bauen Umwelt
der Technischen Universität Berlin
zur Erlangung des akademischen Grades
Doktor der Naturwissenschaften
Dr. rer. nat.

genehmigte Dissertation

Promotionsausschuss:

Vorsitzender: Prof. Frank Neitzel
Berichter: Prof. Roman Galas
Berichter: Prof. Olaf Hellwich
Berichter: Prof. Steffen Schön

Tag der wissenschaftlichen Aussprache: 30.03.2012

Berlin 2012
D 83
Scientific Technical Report STR 12/04

für Elsa

"... wer da sucht, der findet ..."
Lukas 11,10

Abstract

A coastal experiment was realised to study GNSS reflections from the Arctic Ocean. The ground-based setup was located on Disko Island near Godhavn (Qeqertarsuaq) 69.271694° N, 53.543487° W. Reflection events were recorded between Nov. 2008 and Jan. 2009 at low elevation angles, that qualify for interferometric analysis. In previous experiments with smooth surface conditions coherent carrier phase observations were retrieved with centimeter precision. For this experiment with rough ocean conditions such a retrieval fails. A new aspect in this study is the influence of wind-driven waves, sea-ice and icebergs on long-term observation of the Arctic Ocean. An altimetric method is developed, that is applied reliably under these influences.

The GORS receiver is introduced that has so-called Master and Slave correlators to acquire interferometric data. The interferometric phase lacks in sufficient coherence. Conventional approaches to resolve the phase ambiguity fail. But Doppler frequency retrievals discriminate the ocean surface height using pseudo-stationary reflection states.

A Tracking Retrieval and a Spectral Retrieval of the Doppler frequency are developed. An important difference between both retrievals arises from an increased ocean roughness. Simulations show that Tracking Retrieval fails if the surface standard deviation increases above 5cm, whereas Spectral Retrieval only collapse if the standard deviation reaches 50cm and more. Applying both retrievals to the observed data, the difference is remarkable. Tracking Retrieval requires coherent observations, therefore only 145(17) events on L1(L2) are suitable during the last 4 out of 60 days in the experiment. By contrast Spectral Retrieval can be applied on all 60 days covering 2157(450) events on L1(L2).

A continuous altimetric time series results from Spectral Retrieval. A temporal resolution of 20min is achieved for the height estimates if all 36 daily recurring events are available. A tide spectrum based on this time series is derived for the Godhavn location, resolving multiple tide constituents (e.g. S2, M2, K1). Dominance of coherent phase observations during the last 4 days indicates the transition of ocean surface from open-water to an increased ice cover that is validated by ice charts. In-situ validations for altimetric results are not available. Heights from Spectral Retrieval are compared to an ocean surface model which is made up by a Geoid offset (EGM-96) and ocean tides from a respective arctic model (AODTM-5). The deviation from surface model is not isotrop, a large offset occurs in southern direction that vanishes for the eastern and western events. The standard deviation is 18cm to 1.77m (L1) and 26cm to 1.55m (L2) depending on the event track. A dispersion of height estimates on L1 and L2 is not observed. Formal precision of Spectral Retrieval for events lasting 20min lies at 50cm (L1) and 70cm (L2). As model deviation exceeds formal precision, uncertainties of the model in different parameters are analysed. A relevant bias appears for uncertainties in tropospheric model and for undulations of the Geoid (each up to 20cm). A minor bias is predicted by ionospheric model ($<$4cm) and phase windup calculations ($<$6cm).

The stability of Spectral Retrieval motivates also for airborne application, a proof-of-concept is given within the Zeppelin experiment.

Kurzfassung

Ein Experiment wurde an der Küste der Disko Insel nahe Godhavn (Qeqertarsuaq) bei 69,271694° N und 53,543487° W aufgebaut um GNSS Reflektionen über dem Arktischen Ozean zu untersuchen. Ein durchgängiger Datensatz wurde zwischen Nov. 2008 und Jan. 2009 aufgezeichnet, der sich aufgrund der niedrigen Elevationswinkel für eine interferometrische Analyse eignet. In vorangegangenen Experimenten bei glatter Oberfläche wurden kohŕente Trägerphasen mit einer Präzision im Zentimeterbereich abgeleitet. In diesem Experiment bei rauer Ozeanoberfläche versagt diese Ableitung. Ein neuer Aspekt dieser Studie ist der Einfluss der windinduzierten Wellen, des Meereises und der Eisberge auf Langzeitbeobachtungen des Arktischen Ozeans. Eine Altimetriemethode wurde entwikkelt, die zuverlässig anwendbar ist unter diesen Einflüssen.
Der Einsatz des GORS Empfänger ermöglicht die Aufzeichnung interferometrischer Daten durch sogenannte Master und Slave Korrelatoren. Der interferometrischen Phase fehlt es an ausreichender Kohärenz. Bekannte Ansätze zur Lösung der Phasenmehrdeutigkeit scheitern. Aber durch eine Analyse des Dopplers für Reflektionen in pseudo-stationären Zuständen kann der Meeresspiegel bestimmt werden.
Eine Verfolgungs- bzw. eine Spektralanalyse der Dopplerfrequenz werden unterschieden. Dieser Unterschied ist relevant bei einer erhöhten Ozeanrauigkeit. Simulationen zeigen, dass die Verfolgung scheitert falls die Standardabweichung der Oberfläche 5cm übersteigt. Während die Spektralanalyse erst abbricht falls die Standardabweichung 50cm und mehr erreicht. Die Anwendung der beiden Analysen auf die experimentellen Beobachtungen bestätigt diesen Unterschied. Die Verfolgungsanalyse benötigt kohärente Beobachtungen, nur 145(17) Ereignisse auf L1(L2) in den letzten 4 Tagen des 60 Tage umfassenden Datensatzes sind dafür geeignet. Die Spektralanalyse dagegen kann an allen 60 Tagen angewandt werden, wobei 2157(450) Ereignisse auf L1(L2) abgedeckt werden.
Eine durchgehende altimetrische Zeitreihe ergibt sich für die Spektralanalyse, deren zeitliche Auflösung bei etwa 20min liegt, falls alle 36 wiederkehrenden Ereignisse verfügbar sind. Darauf aufbauend wurde ein lokales Gezeitenspektrum abgeleitet, das mehrere Konstituenten (z.B. S2, M2, K1) auflöst. Die Dominanz kohärenter Beobachtungen während der letzten 4 Tage zeigt den Übergang vom offenen Ozean zur Eisbedeckung an, der durch Eiskarten belegt ist. Eine in-situ Validierung der altimetrischen Ergebnisse ist nicht verfügbar. Die Höhen werden mit einem Modell verglichen, dass sowohl den Geoidabstand (EGM-96) als auch Gezeiten (AODTM-5) berücksichtigt. Die Abweichung vom Modell ist nicht isotrop verteilt, ein großer Abstand tritt in südlicher Richtung auf, der allerdings für Ereignisse im Osten und Westen verschwindet. Die Standardabweichung ist 18cm bis 1.77m (L1) und 26cm bis 1.55m (L2) in Abhängigkeit des Ereignisverlaufs. Eine Dispersion der Höhenabschätzung zwischen L1 und L2 wurde nicht beobachtet. Die formale Präzision der Spektralanalyse für ein 20-minütiges Ereignis liegt bei 50cm (L1) und 70cm (L2). Aufgrund der Modellabweichung wurden Unsicherheiten verschiedener Modellparameter untersucht. Ein relevanter Fehler ergibt sich für das troposphärische Modell und für Undulationen des Geoids (je bis zu 20cm). Geringeren Einfluss haben das ionosphärische Modell (<4cm) oder der berechnete Windup Effekt (<6cm).
Die Stabilität der Spektralanalyse begründet auch eine fluggestützte Anwendung, einen Machbarkeitsnachweis liefert das Zeppelin Experiment.

Acknowledgments

A major part of this work is based on the GPS SIDS (Sea-Ice and Dry Snow) project. Contributions to this part in particular to the *Godhavn* experiment are gratefully acknowledged here. Many thanks go to Achim Helm for encouraging my initial work on GPS reflections and for his efforts to develop the GORS receiver. Thanks a lot to Georg Beyerle for his advice on nearly all questions, for scientific guidance and his efforts during the SIDS project. I feel grateful to Galina Dick and Zhiguo Deng for providing tropospheric delays and precise positioning, to Torsten Schmidt for inquiry of ECMWF data, to Markus Ramatschi for the data management and for remarks on the *Godhavn* location, to Tilo Schöne for providing SWH retrievals from EnviSat. Next to my colleagues at GFZ my thanks go to Salvatore d'Addio (ESA) for initiating and pushing the project, to Antonio Rius and Estel Cardellach (IEEC) for important discussions on phase observations, flight experiments and all the support especially during my stay at the IEEC, to Fran Fabra (IEEC) for the train of thoughts and the train of sushi that we shared, to Serni Ribó (IEEC) for the preparations and installations during the SIDS campaign and for the smaller campaign at *la Mola*, to Norbert Jakowski and Christoph Mayer (DLR) for the TEC estimates and to Martin Sørensen (DMI) for support at the setup and for sending fotos.
Advances in the altimetric method and its test in a flying setup are based in particular on *Zeppelin* campaigns, that were prepared and conducted with my colleagues at GFZ during the last years. Many thanks go to Jens Wickert for pushing the project and for the photogrammetric ground-truth he provided, to Georg Beyerle who taught the GORS receiver to fly, to Ralf Stosius for the certification managment and for visualising the flights, to Achim Helm who initiated the first flight and provided a location for the reference station at EADS, to Maorong Ge for remarks on signal acquisition and for the precise trajectory he computed, to Werkstatt at GFZ for integrating the hardware and many kinds of assistance they provided for the preparations. Gratefully acknowledged are our partners, the GSOC team for fruitful discussions on the flight setup and ZLT for flying with us on such an impressive and unique airship.
Next to successful experiments much effort was needed for data analysis and writing. I am grateful for support on those crucial aspects by: Steffen Schön (IFE) for guidance in modelling GNSS observations and crucial discussion on error estimation, Roman Galas (IGG) for mentoring at university with links to seminars and workshops, Christina Arras (GFZ) for remarks on latex and ionospheric refraction and Jamila Beckheinrich (GFZ) for correcting and further fruitful discussions.

Scientific Technical Report STR 12/04
DOI: 10.2312/GFZ.b103-12049

Contents

Scientific Technical Report STR 12/04
DOI: 10.2312/GFZ.b103-12049

Chapter 1

Introduction to Reflection Ranging

Studying radio signals transmitted by the *Sputnik* satellites was one of the earliest scientific applications in cosmonautics [Garriott and Bracewell, 1961]. Soon *Doppler* observations of spaceborne transmitters gave rise to the *Transit* system for satellite navigation, the ancestor of todays Global Navigation Satellite Systems (GNSS) [Parkinson et al., 1995]. Already for the first navigation satellites geodetic applications were proposed, for a review see [Yionoulis, 1998].

Ocean reflections of modern GNSS signals stimulated an altimetric application, that is described in the concept of reflectometry [Martin-Neira, 1993]. In contrast to GNSS positioning, that determines the height of the receiver in-situ, GNSS reflections are used for altimetry of the reflecting surface in remote sensing. In this chapter we will start highlighting an analogy between GNSS positioning and GNSS reflectometry. Signal path ranging is the common principle for both disciplines. The term reflectometry comprises other applications, e.g. soil moisture determination using the power of the reflected signal, that does not involve the signal path. Therefore the term reflection ranging will be used here to be more specific.

The analogy assists to understand the receiver layout for reflection ranging, that is usually based on other GNSS receivers. The analogy fails to model the complexity of reflecting surface. A similar challenge is encountered for RaDaR altimetry, where further analogies can be found. Predominantly water surfaces have been used for reflection ranging. Going from continental waters to the ocean, the complexity of the reflecting surface increases. It rises even more, when the state of the ocean changes between open-water, sea-ice coverage and iceberg occurrence. Fundamental characteristics of ocean roughness will be given in this introduction. Its main focus lies in the methodology of reflection ranging. At the end of this chapter we will review on previous experiments to GNSS reflection ranging. Based on a conclusion and classification of the previous experiments, a starting point for the current work is defined and the scientific challenge is formulated.

A practical advice concerning various acronyms and expressions in the text: a list of acronyms (in `typewriter` style) and a glossary of expressions (in *italic* style) can be found in the Appendix.

Scientific Technical Report STR 12/04
DOI: 10.2312/GFZ.b103-12049

1.1 GNSS Reflections

Global navigation satellite systems GNSS were originally designed to determine the range between a transmitting satellite X and a receiver R. The instantaneous determination of ranges to at least four satellite provides estimates for GNSS positioning. The user actually measures a transit time Δt of the signal from X to R. The measured transit time corresponds to the so called pseudorange, i.e. a range between X and R that is still biased especially by the receiver clock error. A reliable pseudorange is derived from code measurements. The delay of the code phase since transmission is determined at the receiver. Models describing code phase measurements can be found in textbooks, e.g. [Misra and Enge, 2001] Sec. 4.1.1.
Reflections of GNSS signals are a source for Radio Detection and Ranging (RaDaR). A common acronym for this application is GNSS-R. To do ocean altimetry, we will concentrate on the ranging of the specular reflection. Reflected signals in combination with direct signals can be used to determine the height of the reflecting surface. It is not the total transit time, but the excess time of the reflected signal w.r.t. the direct signal, that is crucial for reflection ranging. Measurements of the code phase have been studied in this sense in various experiments, a comprehensive overview on code altimetry is given in [Rius et al., 2010]. Code phase measurements require fundamental modifications compared to common GNSS receivers, such a dedicated receiver is described in [Nogues-Correig et al., 2007]. Measurements using the public C/A code have a precision of about 1m (cf. p.210 [Misra and Enge, 2001]), so the precision of C/A code reflection ranging is also restricted to the meter level. Other codes with a better precision have been tested, e.g. in a flight experiment [Lowe et al., 2002], but those codes are not accessible for the public. A better accuracy is achieved with the carrier phase, which is measured typically with an accuracy of 1cm (cf. p.210 [Misra and Enge, 2001]). In the next part we will consider a simple model describing carrier phase measurements for reflection ranging.

1.1.1 Carrier Phase

The reflection ranging is conceptually similar to a baseline estimation in relative positioning. A 1-d model for precise positioning, which is analog to the following description of reflection ranging, can be found in Sec. 6.1 [Misra and Enge, 2001]. For the positioning case two receivers R and R' are located on a plane with a relative distance b. For the reflection case the receiver R is situated above a plane reflecting surface with the vertical distance h. An image of the receiver R' can be found below the surface with the same vertical distance h. In both cases the transmitter X is far above the scene, so that incident rays are assumed to be parallel and have an equal elevation E, see Fig. 1.1.
The carrier phase ϕ_{R} refers to the direct signal and $\phi_{\mathrm{R'}}$ to the reflected signal. The phase difference between both can be written as a relative phase Δ and an integer ambiguity N, $\phi_{\mathrm{R'}} - \phi_{\mathrm{R}} = \Delta + N$. According to Fig. 1.1 the phase difference is modelled,

$$\Delta + N = \frac{2h}{\lambda} \sin E. \tag{1.1}$$

In this simple model an explicit dependence on the vertical distance h is given. It illustrates altimetry for a plane surface, in absence of signal refraction. A general problem that

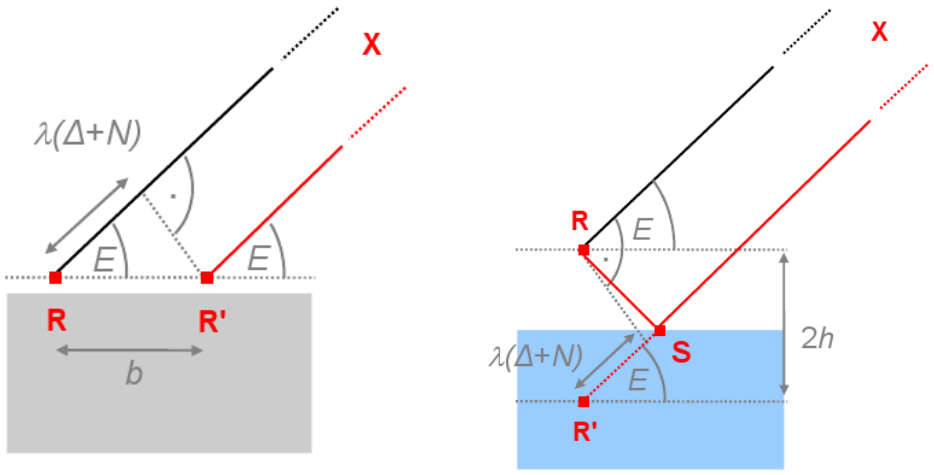

(a) **(b)**

Figure 1.1: Analogy of relative positioning **(a)** and reflection ranging **(b)**. The receiver R' is just an image of R for the reflection case. A specular reflection in S is assumed.

emerges, more or less grievous, for all altimetric strategies is the resolution of the phase ambiguity. We consider this problem here regarding only one transmitting satellite. A system of multiple satellites for reflectometry involves multiple reflection points and it is not considered here. Based on the configuration shown in Fig. 1.1, we assume that the receiver is in a fixed position on ground and dynamics of the reflecting surface can be neglected. Then the distance $2h$ between R and R' is constant. If both receiver and transmitter position were fixed, the observed phase Δ would not change and there would be no possibility to separate Δ and the ambiguity N in order to estimate h.
Fortunately the geometry changes and equations for different epochs t_0 and t_1 can be set up

$$\begin{aligned} \Delta_0 + N &= \frac{2h}{\lambda} \sin E_0, \\ \Delta_1 + N &= \frac{2h}{\lambda} \sin E_1. \end{aligned}$$

A vertical distance $h' = 2h/\lambda$ is substituted and the system can be solved for the unknowns h' and N in matrix notation,

$$\begin{bmatrix} h' \\ N \end{bmatrix} = \frac{1}{\sin E_1 - \sin E_0} \begin{bmatrix} -1 & 1 \\ -\sin E_1 & \sin E_0 \end{bmatrix} \begin{bmatrix} \Delta_0 \\ \Delta_1 \end{bmatrix}.$$

The form is analog to the expression for relative positioning (cf. [Misra and Enge, 2001] eq.(6.3)) and the same conclusion can be drawn. If geometry changes little between t_0 and t_1, the term $[\sin E_1 - \sin E_0]^{-1}$ yields a large error in the altimetric estimates even for

precise measurements Δ_0, Δ_1.
As a consequence long intervals of observations $t_1 - t_0$ with a significant change in geometry would be favourable for a high precision. The concept is rigorously applied for precise relative positioning but two major problems appear w.r.t. reflection ranging. First the accessible geometry for reflections is often restricted to only a small range of elevations and second to resolve a single ambiguity N a continuity in the phase is required between t_0 and t_1.
If the phase is continuous the observation of the acquired field is coherent. In Chapter 7 [Beckmann and Spizzichino, 1987] a definition of a coherent field is given, as it occurs for GNSS reflections. There it is also revealed, that surface roughness leads to a gradually incoherent field. We will see that GNSS reflections for a rough surface like the ocean in general do not provide continuous phase observations. This limitation is a crucial factor when we do ocean altimetry using carrier observations. In the next part statistical characteristics of the rough ocean surface are introduced.

1.1.2 Characteristics of Roughness

The ocean surface on a large (global) scale is influenced by *Geoid* undulations, by ocean tides and ocean currents. They form the ocean topography and are described by deterministic models. Displacements $\xi(x, y)$ from the surface on a small scale (x,y much smaller than the Earth radius) are highly variable and deterministic models are missing. So we differ here between the deterministic ocean topography and a statistical ocean roughness. According to [Robinson, 2004] a statistical description of roughness is given by three measures for the displacement ξ:

- the standard deviation σ_ξ
- the autocorrelation length scale l_ξ
- the mean square slope $\bar{S}^2_\xi$

The perception of surface roughness depends on the wavelength of the signal used for observations. A surface can be rough if wavelengths in the visual range are chosen for sensing but it is still smooth when radio wavelengths are chosen. A relation between the standard deviation of the surface and the wavelength λ_L of the L-band carrier is given by the Fraunhofer Criterion, cf. [Ulaby et al., 1982]

$$\hat{\sigma} \quad = \quad \frac{\lambda_\mathrm{L}}{32 \sin E}, \tag{1.2}$$

where E denotes the elevation dependence. We use it here, to estimate a limit for σ_ξ that still preserve phase coherence in the reflected carrier. That means, for the roughness of the observed surface we claim $\sigma_\xi < \hat{\sigma}$. The term roughness already implies a small autocorrelation length (<100m), compared to topographic lengths (>100m). We will not provide a statistical description of the surface including l_ξ and $\bar{S}^2_\xi$. Statistical models assuming a isotropic distribution of scatterers, e.g. a Gaussian model, fails to describe ocean roughness in a coastal setup. A theoretical approach towards scattering of radio

signal for a rough surface is provided by [Beckmann and Spizzichino, 1987]. An approach focusing on methods for ocean remote sensing is given in [Robinson, 2004], Sec. 9. In the following part we will review different experiments that were conducted for altimetric purposes using the carrier of the GNSS signal.

1.2 Previous Experiments

Experiments using reflection ranging were conducted since more than a decade. We will not give a chronological summary but we will try to merge experiments to strategies that emphasize different aspects and problems. The focus lies on carrier observation. Related to their different acquisition, the following strategies are distinguished:

1. Continuous Tracking
2. Slant Interferometry
3. Multipath Interferometry
4. Occultation Interferometry
5. Codeless Interferometry

Only in the first strategy a carrier tracking of the reflection is used. Within the other strategies interferometric observation of the reflection are derived. A short description for each strategy follows including references that provide more details on the experiments for the interested reader.

1.2.1 Continuous Tracking

For the first strategy is an analog to relative positioning, see Fig. 1.1. It uses two antennas to separate the signals in different links. An up-looking link for the direct signal and a down-looking link for the reflected signal. The antennas are close together to minimize baseline corrections. Reflections are observed close to *Nadir* to shield the down-looking link from the direct signal. Phase data ϕ_{R}, ϕ_{R}, is tracked separately on the respective links. In this strategy it is assumed, that the phase of the reflected signal is continuous and can be tracked in the similar way, as it is done for the direct link. Such setups are usually mounted close to smooth waters to obtain coherent reflections.
This setup was chosen in a pond experiment, described in [Martin-Neira et al., 2002]. The perfectly specular conditions in this setup allows a relative phase tracking using two synchronised receivers.
A similar setup with two synchronised receivers was used on a bridge over the *Oosterschelde* estuary [Belmonte Rivas and Martin-Neira, 2006]. The significantly increased roughness in this experiment compared to a pond led to a temporary loss of coherence. A dedicated tracking loop for the reflected phase and a model-based extrapolation were introduced to compensate the loss. The phase ambiguity is resolved combining reflections from different satellites (Null Space Method). This strategy allows altimetry with cm precision for coherent observations.
A recent experiment at OSO used this strategy for tide observations. Two commercial Leica$^{\mathrm{TM}}$receivers were set up for continuous tracking. An extremely small vertical distance $\approx$1m and a low significant wave height <20cm turned out to be favourable [Löfgren et al., 2011].
In general corrections of signal refraction or the Earth's curvature are not necessary for such a setup with a small vertical distance and the reflection close to *Nadir*. However the

strategy is restricted to a few dedicated locations e.g. bridges, an application in remote sensing is not feasible.

1.2.2 Slant Interferometry

The second strategy differs from the analogy given in Fig. 1.1. The separate phase tracking for the reflected signal is not essential, an interferometric acquisition can be used instead. Then slant observations are possible and the vertical distance can be increased. Coherence of the interferometric phase is not guaranteed, of course. The signals are acquired by a single or multiple antennas. In all setups the relative code delay between direct and reflected signals is corrected, i.e. a modification of common receiver layouts is required.
A demonstration of altimetry using an interferometric phase acquisition was reported over *Crater Lake* in Oregon, USA [Treuhaft et al., 2001]. This location provided specular conditions but at a large vertical distance. A single receiver was setup in an outlook position high above the lake. The single antenna was tilted to detect the superposition of direct and reflected signals. The reflection occurred off *Nadir* at slant elevations between 7° to 24°. The ambiguity and tropospheric delay were estimated for selected phase tracks of 12min length. Height profiles were derived under the constraint that the slope in the profile is close to zero (Minimum Slope Method). For those profiles an altimetric precision of 2cm was achieved.
An altimetry experiment 118m over the Baltic Sea was conducted at *Königstuhl* cliff on Rügen island, Germany [Helm, 2008]. Using the Minimum Slope Method height profiles were derived. In contrast to the *Crater Lake* experiment significant wave heights >1m occurred. Coherent phase observation were detected at grazing elevations between 1° to 15°. The vertical distance of the receiver to the surface and the grazing incidence required a detailed refraction model. The bias could be corrected with a ray tracing based on local refractivity profiles. Below 4° the correction failed. There tropospheric refraction dominated signal propagation with little sensitivity to the height of the ocean surface.

1.2.3 Multipath Interferometry

In the third strategy the reflection is detected as multipath during a geodetic observation. One antenna is used that looks in *Zenith* direction. For the ground-based setup with a vertical distance <50m, a correction of the relative code delay is not required. Carrier multipath results from the tracking of the disturbed direct signal, a separate tracking of the reflection is impossible. Interferometric fringes in the `SNR` occur typically at slant elevations and below, where coherence is less disturbed. A proof of ocean altimetry using the multipath of geodetic observations is given by [Anderson, 1999]. The measurements were conducted at *Scripps Pier*, ≈10m above the surface. The 1Hz sampling of the `SNR` is sufficient for interferometry at vertical distances <50m between receiver and surface. A ray tracing was used to model the refracted signals between 2° to 7° of elevation. The derived pattern propagation factor can be fitted to the `SNR` observation without a remaining phase ambiguity. A linear dependence between the frequency of fringes and the antenna height above the surface emerges. Total height estimates have a standard deviation of 12cm and are validated with tide gauge observations. A critical refraction bias for this small vertical distance occurs only below 2°. A sensitivity to ocean roughness was not observed, the

coherence of fringes at grazing angles is preserved.
Geodetic observations were also studied w.r.t. soil and snow reflections [Larson et al., 2008] [Larson et al., 2009]. Fringes in SNR then occur even at higher elevations and a ray tracing is obsolete. In such a multipath setup the frequency of interferometric fringes directly relates to the vertical distance. More complex aspects for such observations occur due to subsurface reflections which can be neglected for a water surface.

1.2.4 Occultation Interferometry

In the fourth strategy reflections during *Radio Occultation* experiments are studied. In such an RO experiment a receiver, mounted on a LEO satellite, observes GNSS satellites when they rise or set on the local horizon. Those experiments are typically equipped with a single antenna looking to the horizon, where observations occur at grazing elevations. Then interferometric signatures between the direct and the reflected signals are detected even without a correction of the relative code delay.
A comprehensive view on reflections during *Radio Occultations* acquired during the ChaMP satellite mission is given in [Beyerle et al., 2002]. The interferometric frequency shift due to reflection can be derived (Radio Holographic Method). Ray tracing calculations show a linear dependence between the interferometric shift and the height of the reflecting surface. The altimetric sensitivity, however, is low due to the small grazing angles.
An elegant way to use the interferometric phase unambiguously in such an experiment is described in [Cardellach et al., 2004]. A collapse of interference occurs when direct and reflected signals coincide at tangent incidence. For RO events the phase can be tracked to the collapse where it anchors to zero. Profiles of the interferometric phase then directly relate to the total height of the reflecting surface, a resolution of ambiguities is not required. Crucial problems emerge due to fluctuations in the refractivity. For low fluctuation over Antarctica a topographic profile of an ice shelf was derived.

1.2.5 Codeless Interferometry

The last strategy is a completely different approach, it goes without identification of a specific PRN code but it provides straight interferometric correlation of the direct and reflected signal. This innovative strategy to obtain interferometric observations is described in [Rius et al., 2011]. Strictly speaking it produces GNSS code observation rather than carrier observation. The innovation lies in the straight and codeless correlation of the direct and the reflected signal. A precision in the correlation is achieved that corresponds to proprietary codes without using the *Replica* of the code. The configuration of antennas resemble the coherent tracking strategy. But due to the straight correlation an unambiguous delay between the signals is obtained from the peak of the interferogram without tracking. This strategy will not be included into comparison as further research is needed to evaluate the potential of this promising approach. In general one can remark that problems occur to discriminate similar GNSS transmitters as discrimination via CDMA breaks down. As least for a ground-based setup the probability of *Jamming* is increased.

1.2.6 Scientific Challenge

Before the main questions for this thesis will be raised, a conclusion of the previous experiments is given. The strategies differ in characteristic parameters, e.g. the vertical distance h, the satellite elevation E or the expected limit of surface roughness, see the Fraunhofer Criterion eq.(1.2). Those characteristics taken from the previous experiments are compared in Tab. 1.1,

strategy	*platform*	*h [m]*	*antenna setup*	*E [deg]*	*observable*	*σ [cm]*	*refractive correction*	*error range*
Coherent Tracking	e.g. bridge	<50	zenith and nadir	90...30	phase	<1	non	cm
Slant Interferometry	mountain, cliff	>50	tilted	25...2	phase	<1...9	ray tracing, zenith delay	cm
Multipath Interferometry	e.g. pier	<50	zenith	30...2	SNR	insensitive	ray tracing, non	dm
Occultation Interferometry	satellite	~4E5	horizon	<1	phase	unknown	ray tracing	dm

Table 1.1: Comparison of different altimetric strategies.

With these characteristics of ocean roughness in mind, the first and most important question arise for the *Godhavn* experiment. The setup realised at *Godhavn* is dedicated for Slant Interferometry. The vertical distance and the range of elevation lie in a typical range, see Tab. A.3 in the Appendix. A crucial point for this strategy is the sensitivity of carrier phase observations to ocean roughness. A precision of 2cm was reported for a smooth surface [Treuhaft et al., 2001] but the altimetric retrieval breaks down if roughness σ_ξ exceeds the cm scale [Helm, 2008], cf. the Fraunhofer Limit $\hat{\sigma}$. The ocean roughness is the major restriction for Slant Interferometry so far.

Is it possible to find an altimetric method for ocean roughness beyond the Fraunhofer Limit?

During the two months period of continuous observations a remarkable change of surface roughness is expected due to the formation of sea-ice. The *Freeboard* height of the sea-ice may effect the altimetric results.

Can we observe the onset of sea-ice formation and an increasing *Freeboard* height?

Continuous observations in previous experiments lasted for four days at most [Helm, 2008]. The long-term experiment, that will be considered here, gives us the opportunity to study the ocean during two months. A continuous altimetric time series is pursued.

Is it possible to resolve ocean tides from the altimetric time series?

Reflection ground tracks for Slant Interferometry can extend several kilometers. An effect of ocean topography is expected in this range. In particular the steep coast line at *Godhavn* is predestined for considerable *Geoid* undulations along the reflection ground tracks.

Can we prove an effect of *Geoid* undulations in the altimetric results?

The influence of tropospheric refraction is significant for Slant Interferometry. Ray tracing calculations have been successful in particular for the elevation range encountered at *Godhavn*. An uncertainty in the tropospheric correction will remain.

Which altimetric bias persists due to the uncertainty in the tropospheric model?

For comparable previous experiments an ionospheric effect on the interferometric signal was neglected. The `GORS` receiver that run at *Godhavn* is able to record events on two different carriers `L1` and `L2`. Additionally a basic ionospheric model is available for the ray tracing.

Is there a dispersion in the altimetric results and is the bias predictable by the ionospheric model?

Slant Interferometry was conducted ground-based so far. Potential future applications that were discussed for `GNSS` reflections, e.g. tsunami detection [Stosius et al., 2010], require airborne or spaceborne experiments. Valuable findings were made for Occultation Interferometry but its unfavourable geometry is not capable for dedicated altimetric missions.

Can we use Slant Interferometry on a flying platform?

The introduction ends with these questions, that guides through the following chapters and will be resumed in the discussion.

Chapter 2

Godhavn Experiment

The capability for sea-ice remote sensing is one of the most promising applications of GNSS reflections. To explore this application the *Godhavn* experiment was designed. It was one part of the GPS SIDS project initiated by ESA and conducted by IEEC, GFZ and other partners. The motivation for the coastal setup including a characterization of the recorded reflection events will be provided in the first part of this chapter. The roughness conditions in the *Godhavn* area will be analyzed afterwards focusing on the occurrence of wind driven waves, an increasing sea-ice coverage and the probability of iceberg appearance. The last part of the chapter is designated for an essential component of the experiment - the receiver. Based on the common principle of GNSS receiver design the interferometric operation of the GORS receiver will be explained and observations provided by the receiver will be defined.

2.1 Coastal Setup

A ground-based location on the coast was chosen. It allows a long-term monitoring of sea-ice reflections over a small area, in contrast to flights with an aircraft that are limited in time but covers a larger area. The location was chosen to fulfill the following requirements:

- appearance of sea-ice reaching a complete coverage,
- specular reflections in a remote distance to the receiver,
- a large field of view on the ocean surface,
- a shelter for the equipment with Internet connection for data transfer.

Such a location was found near *Godhavn* on *Disko Island*, in Western Greenland. The island lies in the south-eastern part of Baffin Bay, see Fig. 2.1.
An annually recurring sea-ice coverage usually occurs in *Disko Bay* from late December until May as will be described in Sec. 2.2. *Disko Island* has steep cliffs on its southern coast that are well suited to detect specular reflections. Due to sparse vegetation there is a large field of view. The equipment, consisting of a GOLD-RTR receiver from IEEC and a GORS receiver from GFZ was installed in facilities of the Danish Telecom on a cliff at Lyngmarksfjeld 69.2717° N, 53.5435° W, see the topographic map in Fig. 2.2

Scientific Technical Report STR 12/04
DOI: 10.2312/GFZ.b103-12049

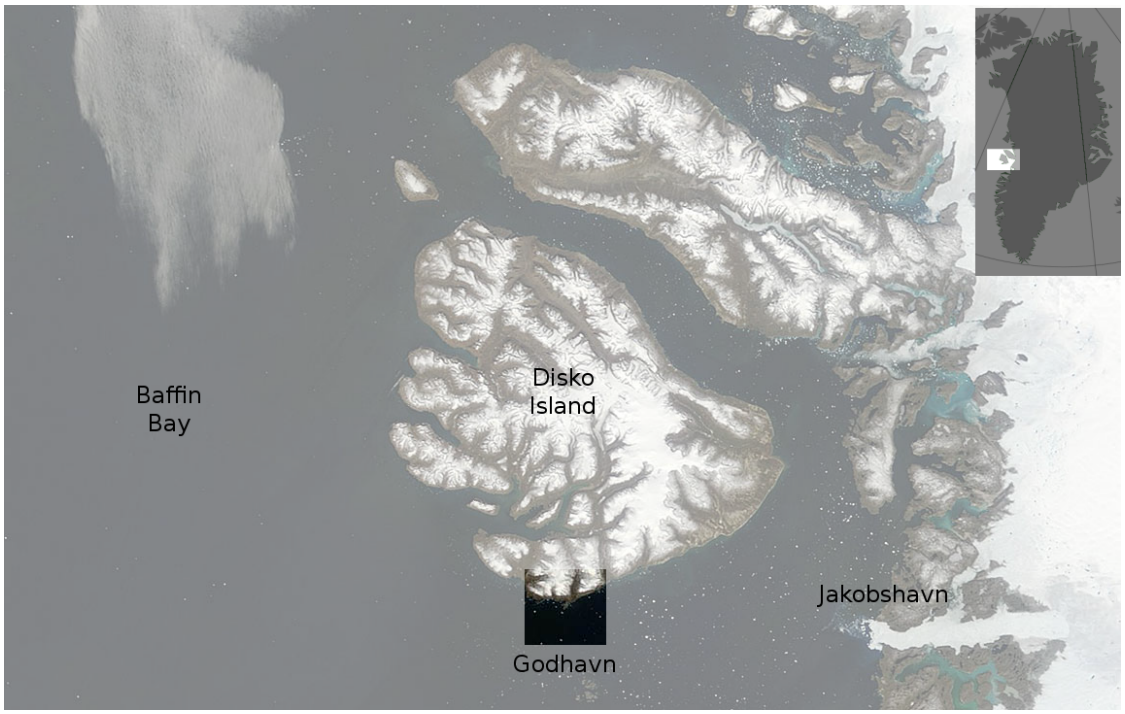

Figure 2.1: Setup localization on *Disko Island*, Western Greenland. The observation area near *Godhavn* is close to a glacier at Jakobshavn, icebergs can be spotted. `MODIS` image provided by `NASA`, 2006.

Different antennas were set up. The up-looking and horizon-looking antennas of the `GOLD-RTR` receiver for the direct and the reflected signal, respectively, and a tilted antenna of the `GORS` receiver for a combined acquisition of direct and reflected signal. A solution for the up-looking `GOLD` link was estimated with the `EPOS` software [Gendt et al., 1998] in precise point positioning, see Tab. A.1 in the Appendix. The baseline to the tilted `GORS` link was derived in relative positioning, see Tab. A.2. The position of the `GORS` antenna results with cm precision and will be the reference for the receiver position, see Tab. A.3.

2.1.1 Reflection Events

A reflection event in the present meaning is a continuous observation of a single transmitting satellite. The direct signal is tracked in code and carrier without interruptions and the reflected signal is acquired interferometrically. An unperturbed direct link to the satellite is required and a specular reflection is assumed. Then an interference between the direct and reflected signal can be observed. More details on interferometric observations are given in Sec. 2.3. For the moment we focus on the characteristics of the events e.g. length and distribution on ground, that arise from the experimental settings. The direct signal of the event has a reference in sky plots, as shown in Fig. 2.3(a) for 09/11/18.
The sky plot shows that the number of reflection events in such a ground-based setup is

(a)

(b)

Figure 2.2: The setup location at the coast near *Godhavn*. **(a)** On the topographic map the location and the boresight direction of the tilted antenna are indicated. **(b)** The antenna mount with the antennas of the `GOLD-RTR` receiver and the tilted antenna of the `GORS` receiver is shown on the picutre. The view is in boresight direction looking over *Disko Bay*. Close to the coast line icebergs occur (indicated by red spots).

limited to only a fraction of the tracks. To find corresponding reflection traces a planar surface model is applied, that will be explained later (cf. Sec. 3.1). An apriori height H_A of the reflecting surface must be assumed. It is given next to the azimuth and elevation mask in Tab. A.3 (Appendix). A minimum distance of the reflecting point from the receiver is required to obtain events that are located predominantly over the ocean. This

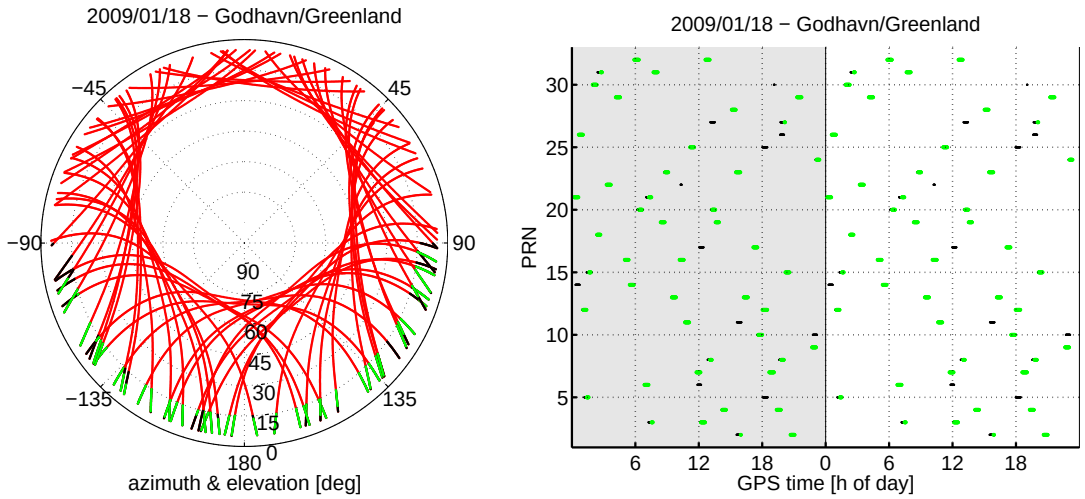

(a) **(b)**

Figure 2.3: **(a)** Sky plot of the events. Tracks that are only in range for direct observations are red. The black tracks have corresponding traces on the reflecting surface, i.e. these are potential reflection events. Tracks in green are those events that were actually recorded. **(b)** Reflection events over GPS time for two successive days.

minimum distance translates into a maximum elevation. Furthermore a minimum elevation for recorded events was set to limit a coupling between the direct and reflected signal, a phenomenon that will be described later in Sec. 2.3. The masks result in a fan-shaped sector of reflection events over the ocean, as shown in the ground plot in Fig. 2.4(a).
The shown traces have a 1min time resolution. They are dense close to the receiver but sparse at larger distances, i.e. the resolution on the surface decreases with a decreasing elevation angle. Starting at the coast line in eastern direction an azimuth mask was applied that ends at the coastline in western direction. A clockwise order of the reflection events is set, counting the events from East over South to West. In total there are up to 56 traces of different reflection events recorded per day. The maximum extension of a trace in the given elevation mask is about 5km, see the example in Fig. 2.4(b). The assumed footprint of a specular reflection event is the entity of all Fresnel Zones (1st order) that belong to the trace, the radial extension is about 5500m and the transversal one is up to 80m. The sequence of all events per day is shown in Fig. 2.3(b).
Events were recorded serially, only one event at the same time. Parallel acquisition of reflection events was not yet implemented in the GORS prototype. Even a serial recording covers the majority of potential reflection events. Comparing the events for two successive days, we see that reflection events recur with a period of ≈23h56min. The exact satellite dependent repeat time in the GPS constellation are given in [Agnew and Larson, 2007]. A statistic overview for events per day is given in Tab. 2.1.
Only <10% of visible GPS tracks yield potential reflection events in such a coastal setup. A serial recording of reflections, i.e. only one event at the same time, using azimuth and elevation masks is sufficient to cover the majority of potential events. Nearly all the reflection events, that were selected by the mask and recorded, lie in the area of interest

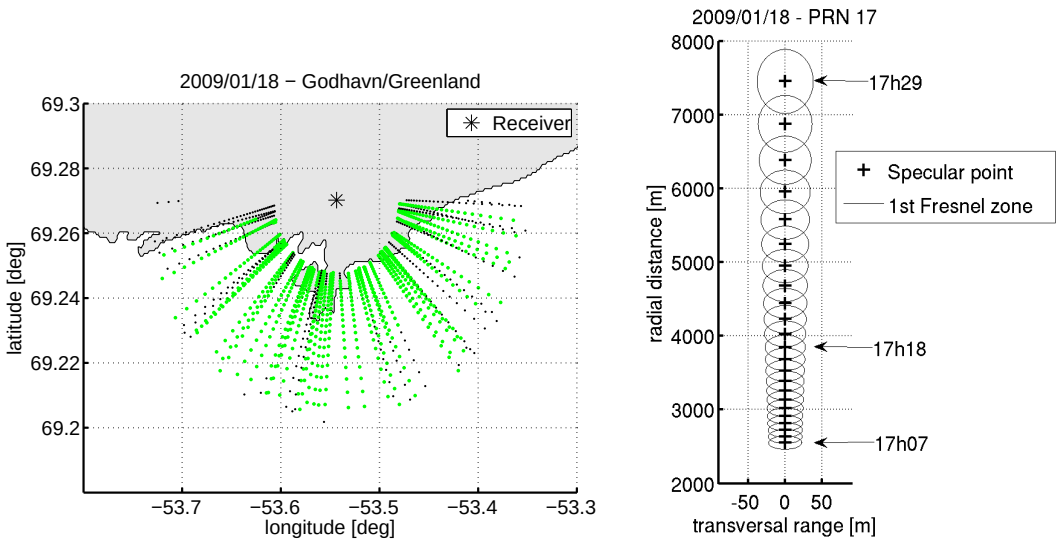

Figure 2.4: Ground plots of specular reflection traces. **(a)** All events over latitude and longitude (different scales on both axis). The traces run either towards the receiver or away from it depending on the rising or setting mode of the transmitter. Satellites appear over the ocean at different azimuth angles and lead to a fan-shape distribution of the reflection events. Black traces refer to potential events, green traces to events that were actually recorded. **(b)** Selected event of PRN 17 over radial distance and transversal range (different scales on both axis). The origin of the radial distance lies on the planar surface below the receiver. The Specular point and the first Fresnel Zone are plotted every minute of the setting event, see time tags.

	events [min]	part [%]
signal in range	16218	100.0
reflection in range	1374	8.5
reflection recorded	994	6.1
recorded over the ocean	942	5.8

Table 2.1: Statistics of the events per day.

over the ocean.

2.2 Ocean Roughness

Disko Bay has open access to the Atlantic Ocean and wind driven waves will significantly contribute to ocean roughness. Since the setup lies north of the Arctic Circle, influenced by currents, a sea-ice season occurs that changes the ocean roughness. During the whole year a large number of icebergs pass through *Disko Bay*, that influences the roughness with unknown consequences for GNSS reflections. In the following the presence of all three factors, wind driven waves, sea-ice and icebergs, is studied.

2.2.1 Wind Driven Waves

Ocean roughness relevant for L-band scattering is predominantly generated by wind driven waves in the gravity regime. Spaceborne radar altimeters are used to measure the Significant Wave Height SWH over the open ocean. The SWH has no statistical meaning that directly relates to ocean roughness. However according to [Robinson, 2004] p.411 we assume

$$\mathtt{SWH} \approx 4\,\sigma_\xi,$$

where σ_ξ is the standard deviation of the ocean surface displacement ξ. Estimates of SWH in Baffin Bay during the time of the experiment are shown in Fig. 2.5.

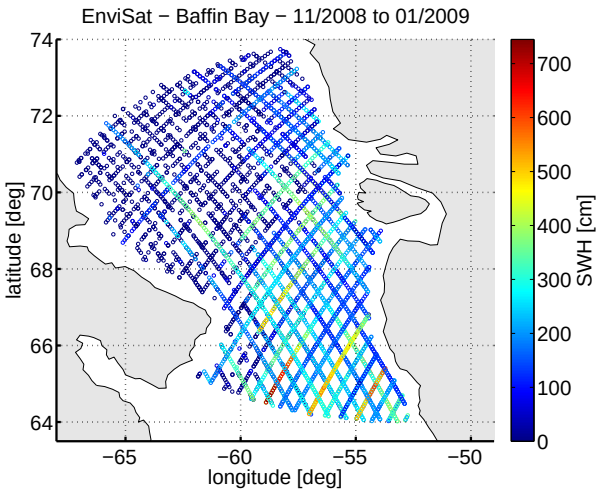

Figure 2.5: Significant Wave Height in Baffin Bay during Nov. 2008 and Jan. 2009, obtained from the radar altimeter on EnviSat.

The north western part of Baffin Bay shows a smaller roughness, due to the presence of sea-ice there. Estimates from the coastal region were excluded as those estimates have a large standard deviation. In general the retrieval of ocean parameters at the coast is difficult. Corresponding echos received by spaceborne radars (radar altimeters, scatterometers) are corrupted by land reflections. An extrapolation of SWH to the coastal regions has to consider local characteristics. The bathymetry and the fetch length, i.e. the distance on the ocean where the wind drives the wave, are characteristic. We expect SWH at *Godhavn* to be significantly below the maximum of 7m as indicated in Fig. 2.5. Unfortunately there is no ancillary in-situ data available for wave heights. Thus we use the surface wind to assess the occurrence of wind driven waves. A plot showing the horizontal components during the campaign is shown in Fig. 2.6.

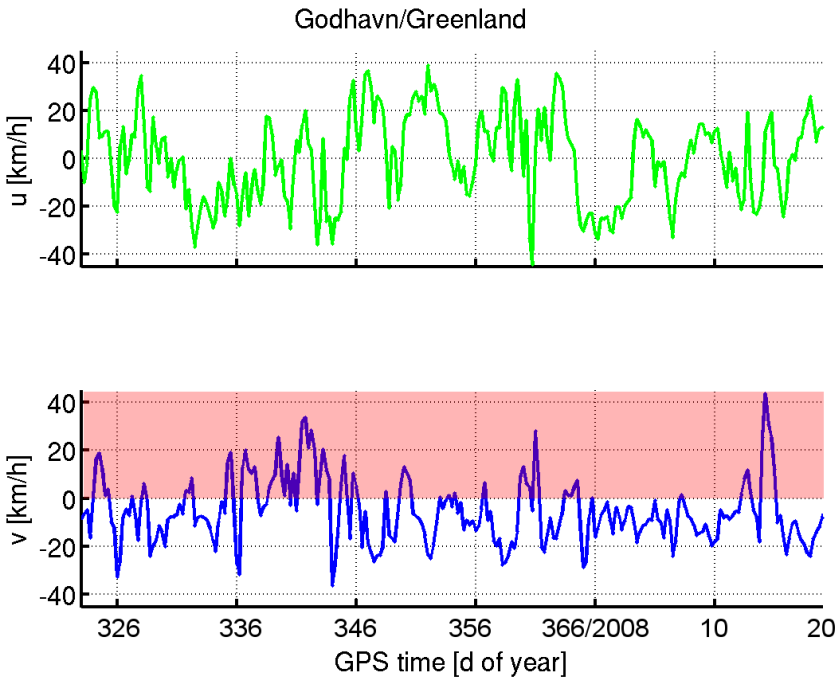

Figure 2.6: Horizontal surface wind velocity vs. day of year. According to meteorological conventions, u component is positive for a west to east flow (west wind) and v component is positive for south to north flow (south wind). The data refer to *Disko Bay* and was obtained from operational `ECMWF` analysis in post-processing all available measurements were assimilated. The resolution of the model is 0.5°x0.5° and 6h in time.

Due to the long fetch an increased wave height is expected for south wind, when the wind drives the waves towards the coast. South wind corresponds to $v > 0$, see shaded area Fig. 2.6. A strong south wind occurs in the beginning of Dec. between `DoY` [336...346]/2008 and at the significant peak on `DoY` 14/2009.

2.2.2 Sea-ice

The wave induced ocean roughness will be affected by sea-ice presence. The term sea-ice refer to frozen sea water in contrast to icebergs and shelf ice that also appear on the ocean but originate from the continents and consist of fresh water. Sea-ice can either be drifting with the wind and ocean currents (drift ice) or it can be fastened to the land (fast ice). During the experiment in Jan. 2009 sea-ice developed at *Godhavn*, as it is shown in Fig. 2.7.

The sea-ice coverage is densified in the first half of Jan 2009. Starting at the open water stage (09/01/03), spread drift ice occurs (09/01/10), the coverage increases to close drift ice (09/01/13) and finally reaches a compact coverage at the end of the experiment (09/01/19). A difference in roughness is expected between the open water stage and compact drift ice. The compactly ice covered ocean surface will be smoother than the wind driven open water surface and the dynamics of roughness vanish when slowly drifting ice dominates the surface.

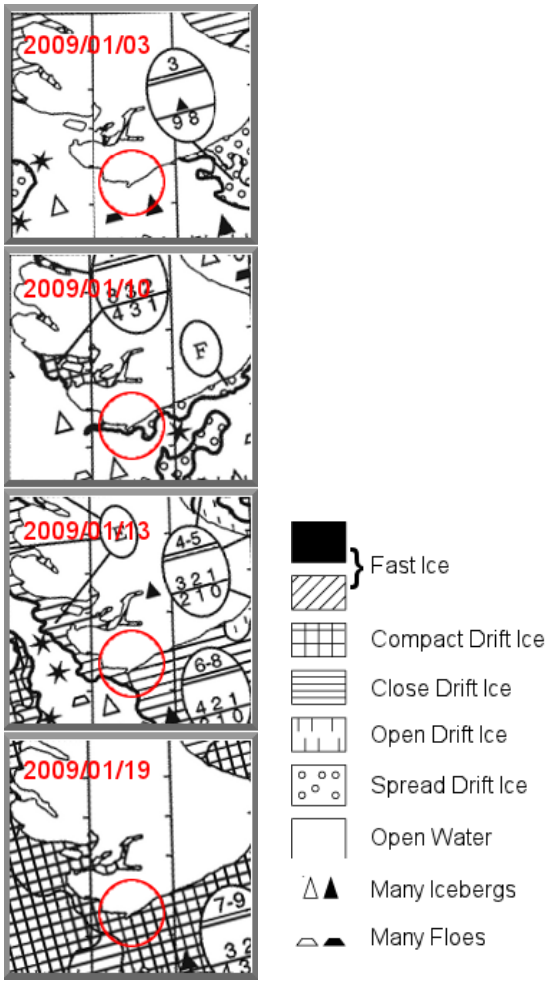

Figure 2.7: Ice charts showing the sea-ice coverage on the southern coast of *Disko Island* in Jan. 2009. The sea-ice maps have a coarse resolution, the coastal area is marked with a read circle centered at the *Godhavn* peninsula. The data was provided by `DMI`, for more information see `http://ocean.dmi.dk/polarview/`.

2.2.3 Icebergs

In contrast to the smoothing of the ocean surface in an early stage of sea-ice development, icebergs will increase ocean roughness or even affect ocean topography. The icebergs concentration in *Disko Bay* is very high throughout the year [Hansen et al., 2001]. A major iceberg source is Jakobshavn Isbrae the largest outlet glacier on Greenland, it drains 6.5% of Greenland's ice sheet area. The drifting icebergs passes at *Godhavn* on their path through *Disko Bay*, see Fig. 2.8.

According to different size categories, icebergs will influence the specular reflecting ocean surface differently. The definition of those categories is given in [Diemand, 2003]. Growlers the smallest category with a height <1m and a length <5m are small w.r.t. the footprint of the reflection. Their motion will be coupled

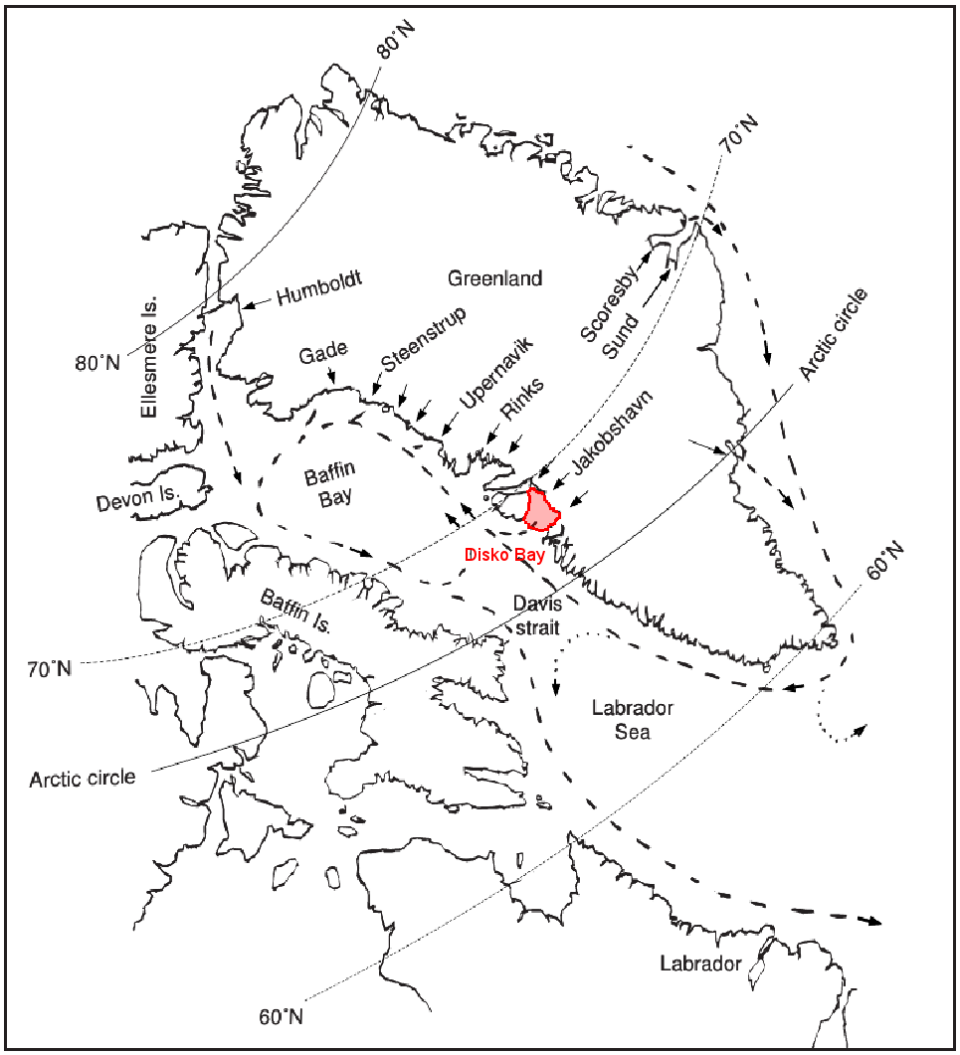

Figure 2.8: Sources and drift paths of North Atlantic icebergs. Image was adopted from [Diemand, 2003].

to the ocean waves. We expect an increase of roughness (L-band regime) but not a complete loss of specular signal propagation. The largest category of icebergs with heights >75m and lengths >200m are relevant obstacles within the footprint of the reflection. Their motion is not affected by ocean waves and the drift speed due to currents normally does not exceed $1 ms^{-1}$. A permanent loss of specular signal propagation can be expected due to the size and the irregular shape of large icebergs.
The size distribution of icebergs will vary between the extreme categories and either an increase of roughness or a complete loss of the specular reflection will occur. According to the mean size of icebergs that is reported for *Baffin* Bay, height 60m and length 100m [Diemand, 2003], a complete loss of the specular event can be expected, due to the reflection track crossing such an iceberg.

Such a crossing is unpredictable. Satellite remote sensing is insufficient to localize icebergs within a certain reflection event during the *Godhavn* experiment. Satellite images cover instantaneously a large area but visual remote sensing was not possible due to the absence of sun light during the arctic winter at *Godhavn*. Actually a coincidence of radar images and GNSS reflection events is necessary to validate the loss of specular reflection with the occurrence of icebergs. Such radar data is sparse, a consistent localization of icebergs using radar data and GNSS reflection events was not possible. A request in advance to acquire radar data is necessary.

2.3 Interferometric Receiver

The GORS receiver is an interferometric receiver, that was i.a. developed for GNSS reflections [Helm et al., 2007]. On the one hand it provides observations of the direct signal comparable to geodetic receivers. On the other hand it provides interferometric observations of the reflected signal. The term interferometric means, that the receiver does not track the carrier of the reflected signal but detects the difference between the direct and the reflected signal by superposition.
The acquisition of an interferometric signal requires a modified architecture of the receiver. The GORS receiver is based on a commercial receiver board from Javad^{TM}. A description of implemented acquisition and tracking algorithms is proprietary software. In literature a general description of signal acquisition (cf. [Borre et al., 2007]), the code delay tracking (e.g. [Misra and Enge, 2001] Sec. 9.5) and the carrier phase tracking (e.g. [Misra and Enge, 2001] Sec. 9.6) can be found. Particular aspects of interferometric receivers will be described here and are summarized by a scheme in Fig. 2.9.

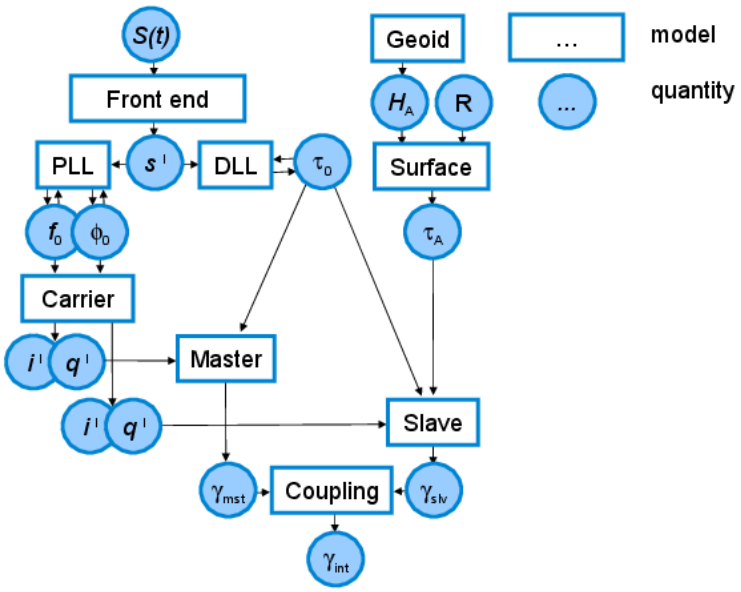

Figure 2.9: Scheme of interferometric processing in the receiver.

A single front-end is used to acquire the GPS signal $S(t)$. The receiver front-end provides a digitally sampled signal $s[l]$. After the sampling in the front-end, the acquisition and tracking of the direct signal follow. A carrier phase lock-loop PLL and code delay lock-loop DLL track the *Doppler* frequency f_0, the carrier phase ϕ_0 and the code delay τ_0 of the direct signal, as we will see. After the removal of the carrier there is an in-phase component $i[l]$ and an quad-phase component $q[l]$ of the sampled signal. The code is modelled twice. On the one hand the *Master* code uses τ_0 from the DLL and on the other hand the *Slave* code

uses $\tau_0 + \tau_A$ from an delay open-loop tracking DOL.
The *Slave* code is determined in an open-loop, i.e. the loop is steered by an external model. It feeds an apriori delay of the reflection w.r.t. the direct signal τ_A. The model is based on external *Geoid* data that provides an apriori ocean height H_A. More details on the apriori delay and the planar surface model can be found in Sec. 3.1.
The correlation using a *Master* and a *Slave* code is the specific solution of the GORS receiver for interferometric acquisition. The signal correlation with the carrier and code models results in a *Phasor* γ_{mst} for the *Master* and a *Phasor* γ_{slv} for the *Slave*. As the name indicates *Master* and *Slave* are not independent. For small delays τ_A even a coupling between tracked and interferometric observations occur. To obtain pure interferometric observations γ a decoupling is necessary.

2.3.1 Antenna Polarisation

Signals transmitted by GPS satellites have a right-handed circular polarisation (RHCP). There are different reasons to use a circular polarisation. A first reason is the changing constellation of transmitting satellites. This change causes a variable orientation of transmitting and receiving antenna. If the transmitted signals were linearly polarised and the receiver antenna had also a linear polarisation, a relative orientation of both antennas would exist, where no signal reception is possible. This phenomenon is well-known for the emission of a linear oscillator, see [Meschede, 2002] Sec. 7.6.6.
A second reason is an ionospheric effect on signal polarisation, the so-called Faraday Rotation. Electromagnetic waves propagating in the ionosphere interact with free electrons and the Earth's magnetic field with the result that the polarisation vector of the electric field is rotated [Rignot, 2000]. If linearly polarised signals were transmitted, the best orientation of transmitting and receiving antennas would depend on the state of the ionosphere. That would be an undesirable constraint.
A third reason for circular polarisation is the mitigation of multipath reflections. The RHCP signal that was transmitted becomes left-handed circularly polarised (LHCP) upon reflection with small incidence angles. Being matched to the RHCP signal, a GPS antenna has an inherent multipath mitigation [Yang and Porter, 2005]. An equivalent mitigation of multipath is not possible using linearly polarised signals.
The circular polarisation of the signal is well suited to transmit an optimum signal power on the direct signal path but it mitigates the signal that is reflected at small incidence angles. The coastal setup at *Godhavn* offers reflection events at large incidence angles, i.e. low elevations, see Fig. 2.3(a). At low elevations, the direct signal has an elliptical polarisation. That means, it contains both polarisations RHCP and LHCP. Upon reflection at large incidence angles the signal has still an elliptical polarisation.
Therefore direct and reflected signals are in parts right-handed polarised and can be received with a single RHCP antenna in the *Godhavn* setup. The antenna was tilted versus the ocean to optimize the gain for reflected signals, while tracking at least 4 satellites on the direct signal path.

2.3.2 Front-End

The GORS receiver acquires signals transmitted by GPS satellites on L1 and L2 carriers. The description of signals in the following is based on the description in [Misra and Enge, 2001]. Only civil code *Replica* of C/A and L2C code are used for correlation on L1 and L2, respectively. Each satellite transmits on the same L-band carriers, a specific PRN code is assigned to the satellite. This discrimination method of different transmitting satellites is called code division multiple access CDMA. In general the transmitted signal is written

$$S(t) = \sqrt{2P^{(k)}}\, D^{(k)}(t-\tau^{(k)})\, x^{(k)}(t-\tau^{(k)}) \cos\left[2\pi(f_{\mathtt{L}} + f_{\mathtt{D}}^{(k)})t + \phi^{(k)}\right]. \quad (2.1)$$

The superscript (k) denotes the satellite. The transmitted power P, the navigation data D, the PRN code x, the code delay τ, the *Doppler* frequency $f_{\mathtt{D}}$ and the carrier phase ϕ depend on the observed satellite. The frequency of the L-band carrier $f_{\mathtt{L}}$ is independent of the satellite. The transmitted signal cannot be processed directly, since a conditioning of the signal by the receiver front-end is necessary. This step comprises a down conversion from the L-band to a IF-band and a digital sampling of the signal. The gain is automatically adjusted by the front-end, the according values are available but were not recorded for the experiment. Neglecting the gain control the digital signal provided by the front-end can be written

$$s[l] = \sqrt{P}^{(k)} D^{(k)}(lT_s - \tau^k) x^{(k)}(lT_s - \tau^{(k)}) \cos[2\pi(f_{\mathtt{IF}} + f_{\mathtt{D}}^{(k)})lT_s + \delta\phi^{(k)}] \quad (2.2)$$

$$\delta\phi^{(k)} = \phi^{(k)} - \phi_{\mathtt{IF}} + \phi_{\mathtt{BPF}}. \quad (2.3)$$

The sample index is l and the sampling period is denoted T_s. For C/A code sampling T_s is typically 1ms. The phase ϕ is affected by offsets $\phi_{\mathtt{BPF}}$ from the band pass filter and $\phi_{\mathtt{IF}}$ due to down conversion to the IF band. The offsets are independent of the satellite (cf. [Misra and Enge, 2001] Chapter 9) but depend on the front-end. An unknown offset arise for example in the interferometric phase if different front-ends are used to sample the direct signal and the reflected signal. In the *Godhavn* experiment only one front-end was used and no offset in the interferometric phase arises.

2.3.3 Carrier Alignment

In signal processing often a complex representation with two carrier models is used. The in-phase and quad-phase model of the carrier are written

$$\sqrt{2}\cos(2\pi(f_{\mathtt{IF}} + f_0)lT_s + \phi_0),$$
$$\sqrt{2}\sin(2\pi(f_{\mathtt{IF}} + f_0)lT_s + \phi_0).$$

We assume that the parameters of the carrier (f_0,ϕ_0) are tracked for a specific satellite. The superscript (k) of satellite can then be left out for the following expressions. The cos and the sin terms are in-phase and quad-phase models of the IF carrier with a phasing of $\pi/2$, respectively. The parameters f_0 and ϕ_0 are provided by the PLL tracking and refer

code	f carrier [MHz]	chip rate [kHz]	bit rate [Hz]	period [ms]
C/A	1575.42	1023.0	50	1
L2C	1227.60	1023.0	50	1500
CM	1227.60	511.5	25	20
CL	1227.60	511.5	-	1500

Table 2.2: Comparison of C/A and L2C code characteristics.

to the direct signal. The in-phase and quad-phase models are used for a carrier *Wipeoff*, the signal $s[l]$ is bitwise multiplied with both components. Fast variations of the signal carrier are stopped but interferometric variations remain. After a low pass filter the *Wipeoff* results can be written in-phase and quad-phase

$$i[l] = \sqrt{P}D(lT_s - \tau)x(lT_s - \tau)\cos(2\pi(\Delta f)lT_s + \Delta\phi), \quad (2.4)$$
$$q[l] = \sqrt{P}D(lT_s - \tau)x(lT_s - \tau)\sin(2\pi(\Delta f)lT_s + \Delta\phi), \quad (2.5)$$

where only residuals $\Delta f = f_D - f_0$ of the *Doppler* and $\Delta\phi = \delta\phi - \phi_0$ of the carrier phase remain. The code and data bit modulation of the signal is not affected. A correlation with the code and a demodulation of the data bit follow before a *Phasor* $\gamma = I + iQ$ is obtained. A preview to the results of the C/A code *Master* correlation, Fig. 2.10(a), shows that the GORS receiver tracks the carrier of the direct signal. The Q component vanishes, only the noise level remains. The signal amplitude $\sqrt{I^2 + Q^2}$ is completely tracked in the in-phase component. Fluctuations in I with a period of ≈40s indicate a disturbance of tracking due to multipath. The multipath amplitude at the end of the setting event, at a large radial distance see Fig. 2.4(b). The results for L2C, Fig. 2.10(b), show the same tracking characteristics but are less affected by multipath.

2.3.4 Code Characteristics

There are differences between both civil codes C/A and L2C that are used by the GORS receiver. Before we go on with a description of the *Master* and *Slave* correlation those differences have to be considered. Innovations of the L2C code are described in [Cho et al., 2004]. Some important characteristics comparing the civil codes are picked in Tab. 2.2. The advantage of L2C is the combination of two codes, the CM code with a moderate period and the CL code with a long period. The long code has better correlation properties but the moderate code has faster acquisition properties. Both codes are combined to the L2C code using time multiplexing, as described in [Fontana et al., 2001]. The time multiplexing doubles the chip rate and bit rate. The GORS uses only the CL code for correlation, the CM code modulation with an additional data bit is ignored. Only half of the transmitted power P_{L2C} can then be used, as a consequence the *Phasor* amplitude compared with the noise level for L2 is lower than for L1. The decreased multipath signature for L2 tracking results could be explained by different correlation properties of CL.

2.3.5 Master Correlation

We have already concluded the signal alignment with the carrier model from Fig. 2.10. The alignment with the *Master* code model, written $x(lT_s - \tau_0)$, results in a correlation peak at τ_0. A correct alignment require that fading of the direct signal is small w.r.t. the strongest reflection. Then the largest peak at (τ_0, f_0) refers to the direct signal and τ_0 can be tracked by a `DLL`. The code correlation leads to a code *Wipeoff*. To preserve phase coherence within the summation, the *Wipeoff* is done for I and Q components separately

$$\begin{aligned} I_0 &= \frac{1}{L}\sum_{l=1}^{L} x(lT_s - \tau_0)\, i[l], \\ Q_0 &= \frac{1}{L}\sum_{l=1}^{L} x(lT_s - \tau_0)\, q[l]. \end{aligned}$$

The *Master* output of the receiver are the correlation sums I_0 and Q_0 at the delay τ_0. In the nomenclature of code tracking this output corresponds to the *Prompt* correlation, not all tracking parameters (e.g. from early or late correlators) are provided. For the `GORS` receiver the coherent integration time in the correlation sum is $L\,T_s = 5$ms. The data modulation period on `C/A` is 20ms, i.e. the data bit flips still can be corrected as follows

$$\begin{aligned} D &= \mathrm{sign}(I_0), \\ I_{\mathrm{mst}} &= I_0\, D, \\ Q_{\mathrm{mst}} &= Q_0\, D. \end{aligned} \tag{2.6}$$

Because the correlation on `L2` is restricted to the `CL` code no navigation data need to be corrected there. The corrected correlation sum are merged to a complex *Phasor* observation $\gamma_{\mathrm{mst}} = I_{\mathrm{mst}} + iQ_{\mathrm{mst}}$. Plots for `L1` and `L2` observations are found in Fig. 2.10.

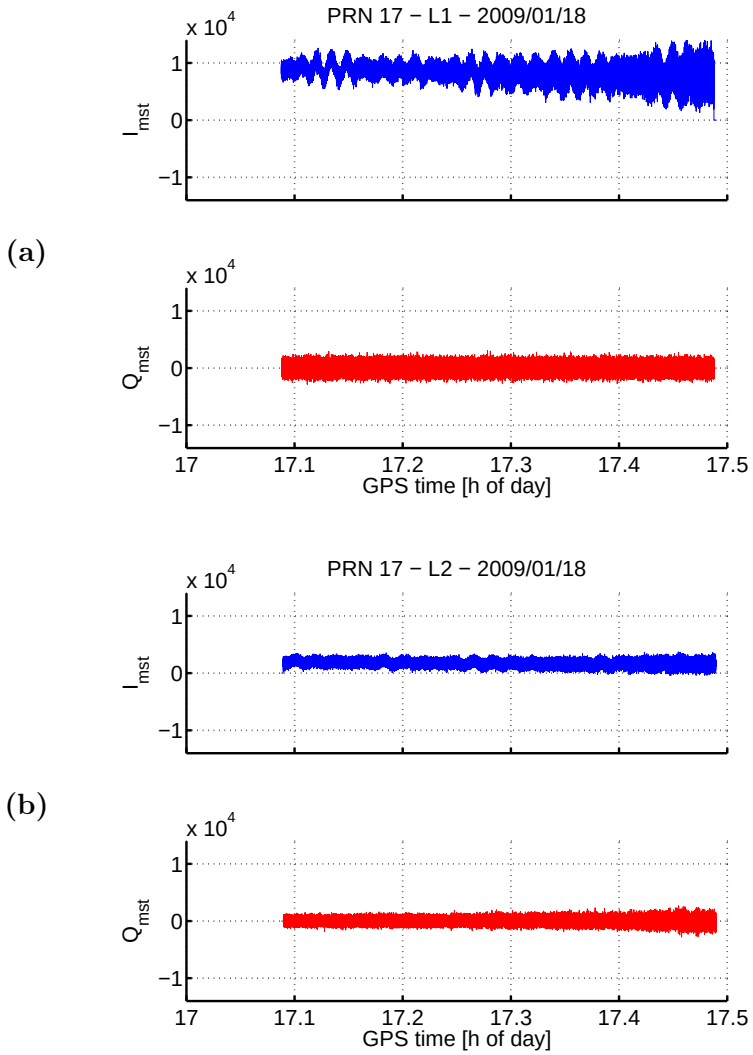

Figure 2.10: *Phasor* components of the *Master* tracked in *Doppler*, phase and code delay, **(a)** on L1 and **(b)** on L2. A reference for the ground track is given in Fig. 2.4(b).

2.3.6 Slave Correlation

An open-loop tracking is used to align the *Slave* code model, written $x(lT_s - \tau_0 - \Delta\tau)$, to the reflected signal. The delay of the direct signal is τ_0. The delay of the reflected signal will be larger $\tau_0 + \Delta\tau$. The *Slave* model is shifted relative the *Master*, the delay $\Delta\tau$ is approximated by the apriori delay τ_A. A scheme indicating the shift is shown in Fig. 2.11. In the scheme it is assumed that the direct signal is unperturbed and only a single specular reflection occurs. That yields the triangular shape of the waveform. It is related to the autocorrelation function of the code

$$\Lambda(\tau) \quad = \quad \begin{cases} 1 - \frac{|\tau|}{\tau_c} & -\tau_c \leq \tau \leq \tau_c, \\ 0 & \text{else.} \end{cases}$$

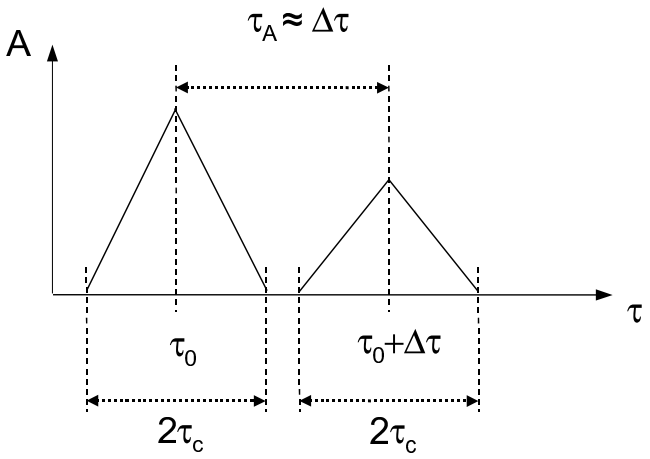

Figure 2.11: Scheme of waveforms from a direct and a specularly reflected signal. The correlation amplitude A in the τ domain is plotted. The width of the waveform is approximated by width of the autocorrelation τ_c. The delay $\Delta\tau$ is approximated with an apriori model τ_{A}. The amplitudes of the waveforms are arbitrary.

The support of the autocorrelation function, i.e. those delays with a correlation different to zero, spans two chip lengths τ_c around the maximum. The apriori delay τ_{A} is used to shift the *Slave* model $x(lT_s - \tau_0 - \tau_{\mathrm{A}})$ to the reflected waveform. A code delay open-loop (`DOL`) updates the apriori delay in real-time. In other words the receiver is open to use external delays that are instantaneously provided to create the *Slave* model. The external delay is given by the following model

$$\tau_{\mathrm{A}} = \frac{2}{c_0} h \sin E, \tag{2.7}$$

with c_0 the speed of light, E the transmitter elevation and h the vertical distance. This vertical distance between the receiver and the reflecting surface is $h = H_{\mathrm{R}} - H_{\mathrm{A}}$, where the apriori height of the reflecting surface H_{A} is obtained from a *Geoid* model like e.g. `EGM-96`. More details about the apriori estimation are provided in Sec. 3.1. For correlation the in-phase and quad-phase signals $i[l]$ and $q[l]$ are used, cf. eq.(2.5). Apriori, the carrier at (f_0,ϕ_0) is used, changes of the *Doppler* and carrier phase at the reflected peak are not tracked in real time. To preserve phase coherence within the summation, the *Wipeoff* is done again separately for I and Q components

$$\begin{aligned} I_1 &= \frac{1}{L}\sum_{l=1}^{L} x(lT_s - \tau_0 - \tau_{\mathrm{A}})\, i[l], \\ Q_1 &= \frac{1}{L}\sum_{l=1}^{L} x(lT_s - \tau_0 - \tau_{\mathrm{A}})\, q[l]. \end{aligned}$$

The `GORS` receiver outputs the correlation sums I_1 and Q_1 at the delay $\tau_0 + \tau_{\mathrm{A}}$. The sampling period of the *Phasor* is again 5ms. For `C/A` code correlations, the navigation data D can be wiped off in post-processing, using D obtained from eq.(2.7),

$$
\begin{aligned}
I_{\mathrm{slv}} &= I_1\, D, \\
Q_{\mathrm{slv}} &= Q_1\, D.
\end{aligned}
$$

Finally the *Phasor* $\gamma_{\mathrm{slv}} = I_{\mathrm{slv}} + iQ_{\mathrm{slv}}$ is obtained on `L1` an `L2`, as shown in Fig. 2.12.

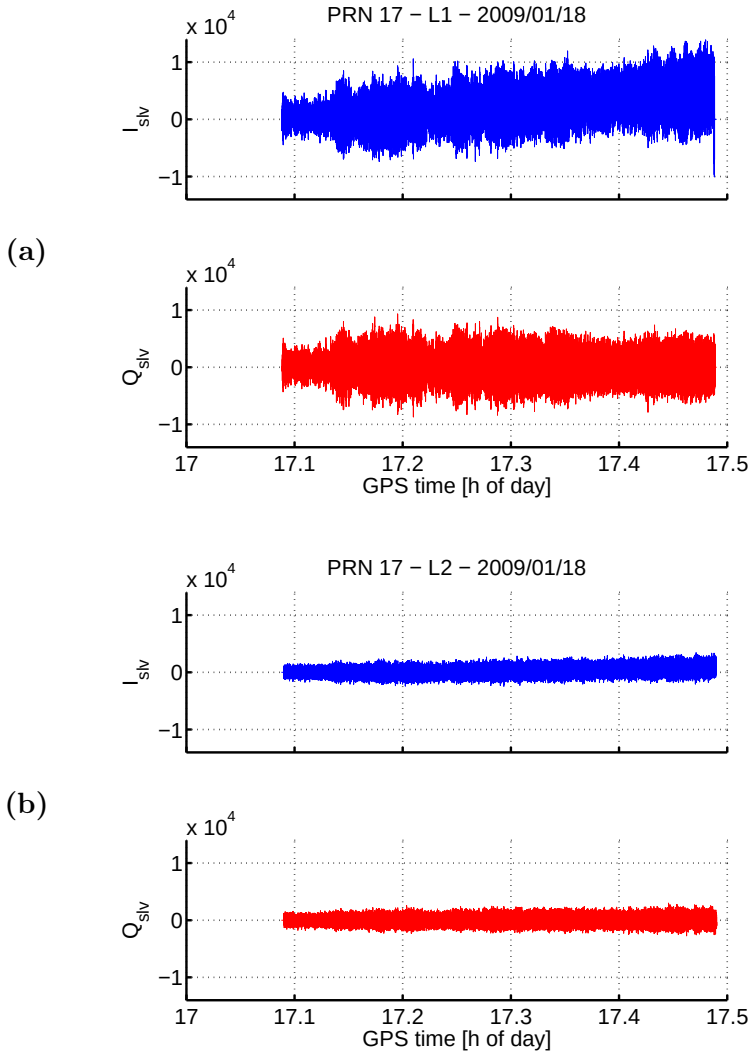

Figure 2.12: Phasor components of the *Slave* in an open-loop tracking of the code delay, **(a)** on `L1` and **(b)** on `L2`.

In contrast to the *Master*, the *Phasor* amplitude of the *Slave* is distributed almost equally to the in-phase and quad-phase components. A drift occurs in-phase, that is related to a coupling of *Master* and *Slave* correlations. The large quad-phase amplitude shows that the carrier of the reflected signal is not tracked. Interferometric oscillations around zero occur that indicates a frequency shift f_{int} but those oscillations cannot be resolved on time scale of an event in Fig. 2.12.

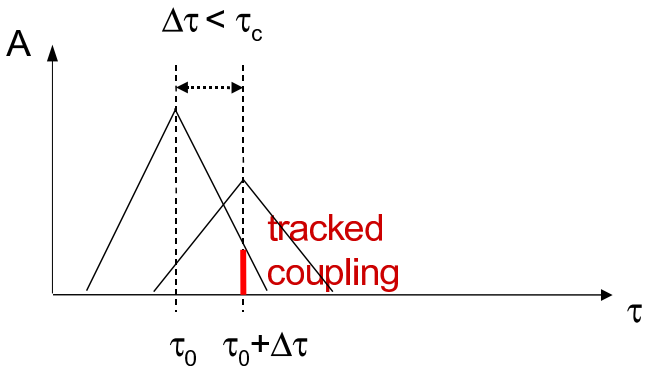

Figure 2.13: Scheme of the coupling at short delays. The delay $\Delta\tau$ is below the code chip length τ_c. Components from the tracked direct waveform affect the *Slave* observations.

2.3.7 Coupling

The range of in-phase and quad-phase values in Fig. 2.12 is almost equal, an increase of the in-phase value occurs at the end of the event. The offset indicates that parts of the signal are tracked. A coupling of interferometric *Slave* observations and tracked *Master* observations occur. In Fig. 2.13 the coupling of tracked components from the direct waveform to the *Slave* observations is indicated.
The trigger is the excess delay $\Delta\tau$ which decreases below the code chip length $\tau_c = 1\mu$s. It is an artefact that originates from the finite code chip length and perturbs interferometric observation at short delays. The decrease of the delay τ_{A} below one chip for the example is shown in Fig. 2.14.
For the delays in the example, a decoupling of *Slave* observations from tracked components is possible. The derivation of the decoupled interferometric *Phasor* starts with eq.(2) in [Treuhaft et al., 2001]. A complex *Phasor* for correlations, that includes the direct and the reflected waveforms, is modelled by

$$\gamma(\tau_i) = e^{i\phi_0}\left[A_d\,\Lambda(\tau_i-\tau_0) + A_r e^{ik_0(L_r-L_d)}\Lambda(\tau_i-\tau_0-\frac{L_r-L_d}{c})\right]. \qquad (2.8)$$

The model is implemented at an arbitrary delay τ_i. The signal path length and the amplitude are written $L_{r/d}$ and $A_{r/d}$ with subscripts for the reflected or direct signal, respectively. The wavenumber $k_0 = c_0/f_0$ relates to the carrier frequency of the direct signal. The triangular autocorrelation function of the code is $\Lambda(\tau)$. The given model implies a tracking of f_0, additionally for the `GORS` receiver we claim, that the phase is tracked at ϕ_0, i.e. the factor $e^{i\phi_0}$ vanishes. The *Master* which is properly tracked at the correlation peak (τ_0,f_0,ϕ_0) is then written

$$\gamma_{\mathrm{mst}}(\tau_0) = A_d + A_r e^{ik_0\Delta L}\Lambda(\Delta\tau).$$

The signal path difference was substituted $\Delta L = L_r - L_d$ and the excess delay is then $\Delta\tau = (L_r - L_d)/c_0$. Properties of the autocorrelation were used, $\Lambda(0) = 1$ and $\Lambda(-\tau) = \Lambda(\tau)$. The *Slave* tracks the code in open-loop assuming $\Delta\tau \approx \tau_{\mathrm{A}}$, the tracking of the carrier remains unchanged (f_0,ϕ_0). The *Phasor* reads

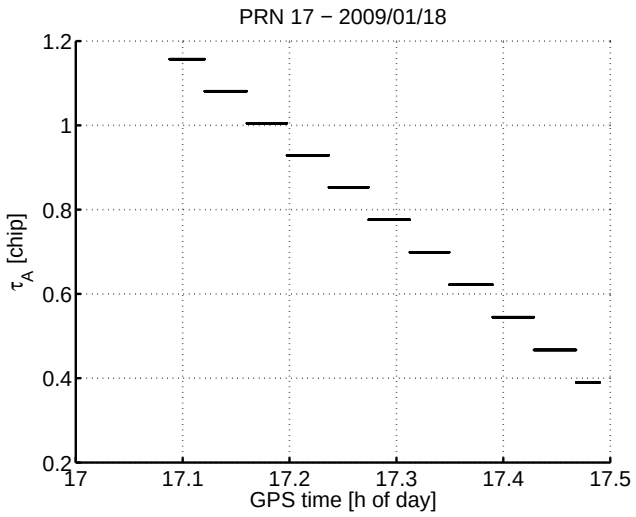

Figure 2.14: Apriori delay vs. time of the reflection event. The delay decreases continuously during the event. Steps occur due to the coarse resolution of the apriori model. More than 80% of the event is affected by coupling.

$$\begin{aligned} \gamma_{\mathrm{slv}}(\tau_0 + \tau_{\mathrm{A}}) &= \left[A_d \Lambda(\tau_{\mathrm{A}}) + A_r e^{ik_0 \Delta L} \Lambda(\tau_{\mathrm{A}} - \Delta\tau)\right] \\ &\approx \left[A_d \Lambda(\Delta\tau) + A_r e^{ik_0 \Delta L}\right]. \end{aligned}$$

The open-loop assumption $\Delta\tau \approx \tau_{\mathrm{A}}$ was used in second line. An interferometric *Phasor* γ_{int} that is decoupled from the tracked direct waveform arises from a combination of the *Master* and *Slave Phasor*

$$\begin{aligned} \gamma_{\mathrm{int}} &= \frac{\gamma_{\mathrm{slv}} - \Lambda(\Delta\tau)\gamma_{\mathrm{mst}}}{1 - \Lambda^2(\Delta\tau)} \\ &= A_r e^{ik_0 \Delta L}, \end{aligned}$$

where the second line follows by substitution of the models γ_{mst} and γ_{slv}. The model for the interferometric *Phasor* then only depends on the amplitude of the reflection A_r and the interferometric path ΔL. The decoupled interferometric *Phasor* is shown in Fig. 2.15.

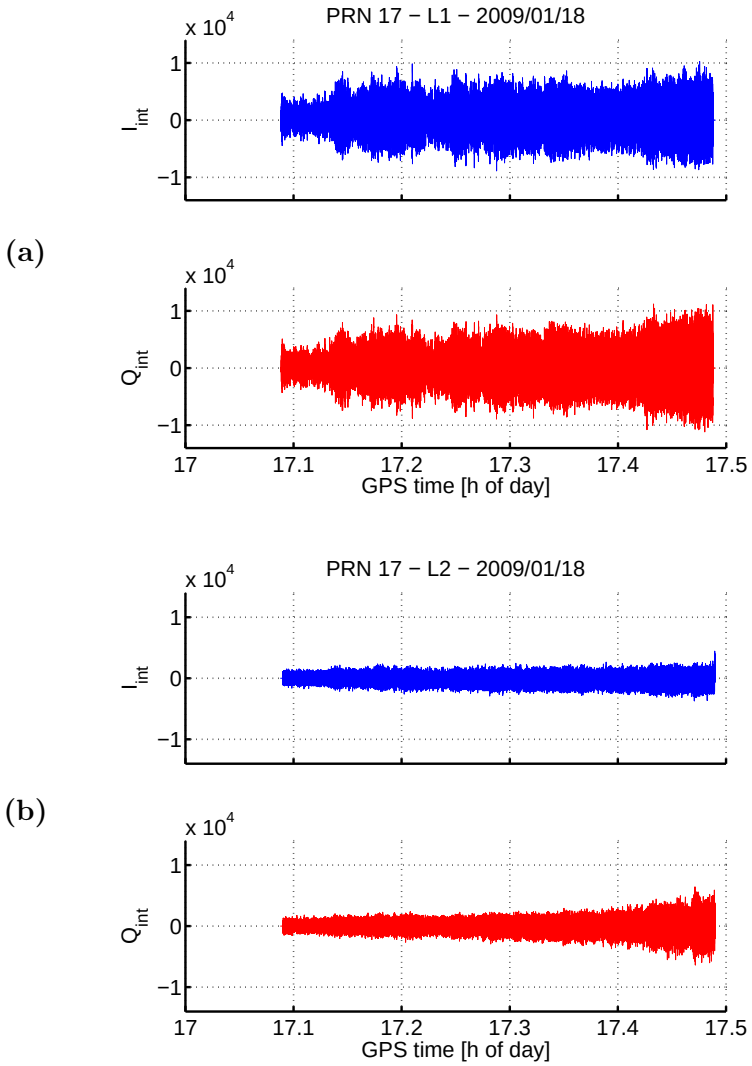

Figure 2.15: Components of the interferometric *Phasor*, **(a)** on L1 and **(b)** on L2.

The plots in the time domain show no drift anymore. For convenience interferometric observations, e.g. the *Phasor*, the *Doppler* frequency or the path, are written γ, f and L in the following parts, the annotation 'int' is left out.

2.3.8 Spectral Representation

The *Phasor* representation in the time domain, that was considered in the last part is insufficient to reveal the interferometric information. A spectral representation in the frequency domain reveals more information as we will see. The Fourier Transform Γ of the complex *Phasor* γ is determined by

$$\Gamma(\nu) = \int e^{-i\,2\pi\nu t}\gamma(t)dt. \tag{2.9}$$

The Fourier Frequency ν differs from the *Doppler* Frequency that is regarded in the further retrievals. The Fourier Frequency is positive if the signal path is increasing, the *Doppler* Frequency in contrast is negative if the signal path is increasing. As a convention the *Doppler* is used in the observations and plots. The Fourier Frequency is only needed for the formal description. The spectra vs. the *Doppler* Frequency derived from γ_{int} on L1 and L2 are shown in Fig. 2.16.
Each spectrum has a dominating interferometric peak. For L1 a secondary peak occurs at zero that is caused by multipath, the larger interferometric peak is at $f \approx 0.9$Hz. For L2 the interferometric peak is at $f \approx 0.7$Hz, a peak characteristic for multipath is absent. This absence might be due to different correlation properties but it will not be investigated here. The interferometric peaks can be validated using the model in eq.(2.7). The apriori delay approximates the interferometric path $L \approx c_0 \tau_{\text{A}} = 2h \sin E$. An estimate of the interferometric *Doppler* is then given by,

$$\begin{aligned} f &= -\frac{1}{\lambda_{\text{L}}} \frac{dL}{dt} \\ &= -\frac{2h}{\lambda_{\text{L}}} \cos E \, \frac{dE}{dt}. \end{aligned} \tag{2.10}$$

For the event in Fig. 2.16 the following estimates are used, the vertical distance $h \approx 670$m, an elevation $E = 10^\circ$ and a mean elevation rate of the setting satellite dE/dt of approximately 10° in 25min. Considering the different carrier wavelengths λ_{L} we obtain $f \approx 0.81$Hz for L1 and $f \approx 0.63$Hz for L2. The interferometric model roughly agrees with the peaks obtained in the spectra. However the difference of about 10% in observation and model estimation is too large for a reasonable height estimation. A precise model of the interferometric path and strategies to invert the ocean height will be presented in the Method chapter.

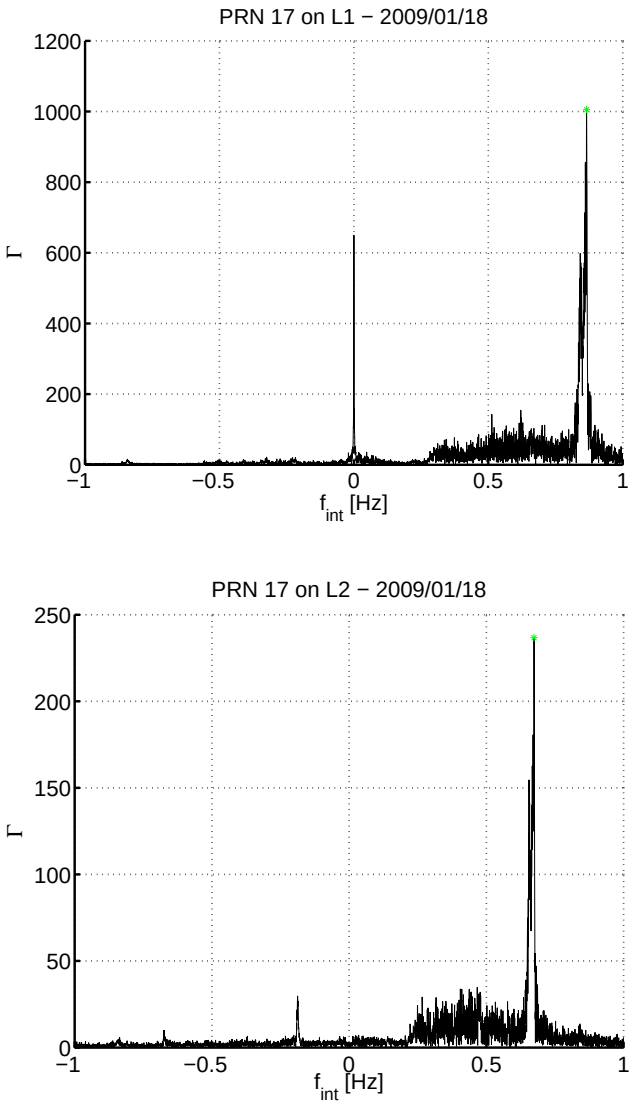

Figure 2.16: Spectra derived from the complex *Phasor* γ_{int}, **(a)** on `L1` and **(b)** on `L2`. Due to complex values in the time domain the spectra have contribution for positive and negative frequencies. The peaks provide interferometric observations.

Chapter 3

Altimetric Method

The most important question, that shall be answered in this thesis, asks for an altimetric method in case of a rough ocean surface. The ranging with GNSS signals in such a method requires a precise description of the signal path. The first part of this method chapter is therefore dedicated to the model of the optical phase path. Using ray tracing, direct and reflected paths are calculated and an interferometric path can be defined by their difference. The dependency of the modelled interferometric path on the surface height is analyzed for a later height estimation.
The estimation of the surface height using a signal path model and the interferometric observations is the crucial point of the altimetric method. An empirical tracking of surface height changes is the first approach. It is comparable to the Continuous Tracking strategy, ray tracing calculations are not considered. The restricted coherence required an alternative approach. A height estimation, using the residual *Doppler* frequency in pseudo-stationary reflections states, is developed. A Tracking Retrieval and a Spectral Retrieval of the *Doppler* will be distinguished.

3.1 Signal Path

The interferometric signal is determined by the propagation along the direct and the reflected path as we saw in the last part. The precision for altimetric results that are derived from the signal is dependent on a precise model of the propagation. A detailed model of atmospheric refraction and the Earth's curvature, that is described below, allows a ray tracing of the direct and the reflected signal. A scheme of the signal path model is shown in Fig. 3.1.
The model yields the optical phase path of the direct signal L_d and for different states of the reflected signal L_r^j. Three major parts of the model can be distinguished, the surface curvature, the refractivity and finally the rays.
Precision in the surface model is reached step by step. Starting with the line-of-sight from the receiver R to the transmitter X, the azimuth α and the elevation E of the satellite in R are determined. To adjust a spherical model to the ocean surface, an apriori specular point A is calculated and its distance d to the receiver on the apriori surface is derived. The height H_A of the apriori ocean surface is approximated by a *Geoid* model. The point A on a plane is only a rough estimate for the reflection. But it is the basis for a more

Scientific Technical Report STR 12/04
DOI: 10.2312/GFZ.b103-12049
Deutsches GeoForschungsZentrum GFZ

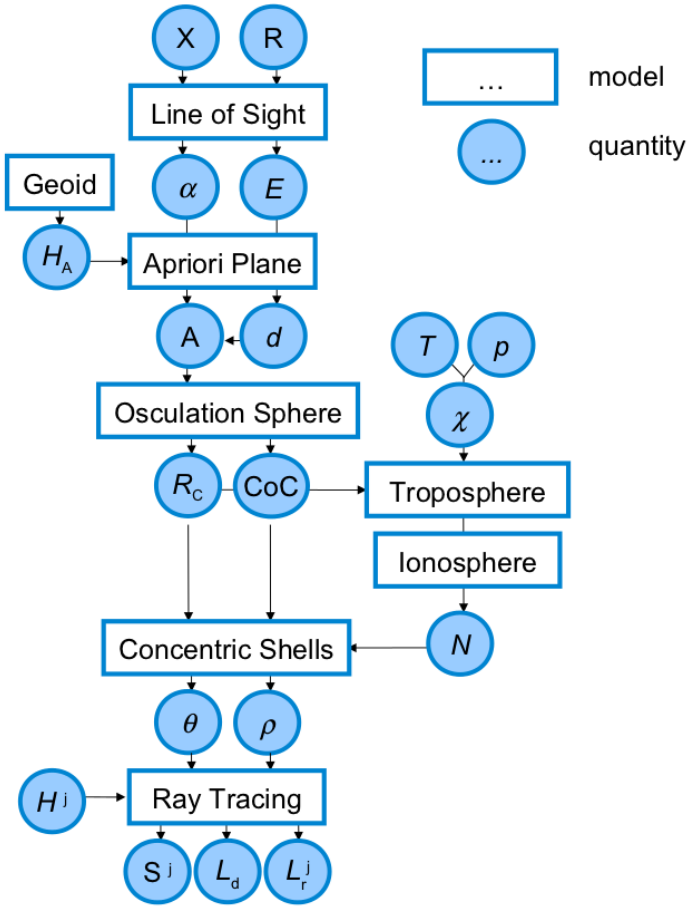

Figure 3.1: Scheme of the signal path model.

precise spherical model. An *Osculation* sphere that meets the ellipsoid at A models the curvature precisely. The center of curvature (CoC), the radius of curvature R_c and the curvature centered (CC) frame are defined.
The tropospheric refractivity is modelled using meteorological parameters, i.e. the temperature T, the pressure p and the specific humidity χ. If necessary a model of dispersive refraction in the ionosphere is added. The total refractivity N is computed in concentric shells above the spherical surface.
Using the spherical symmetry of the model, the ray propagation can be described quasi-analytically. The trace of the ray is parameterized by the radius ρ and an angle θ in the CC frame. The direct path is well defined. For the reflected path different states at height levels H^j are calculated. Next to the path lengths, the coordinates of different specular points S^j are computed.

3.1.1 Line-of-Sight

Azimuth and elevation of the transmitter X are determined in the receiver position R. A precise position R is determined, see Tab. A.3. To calculate the position X broadcast ephemerides are used. Geocentric coordinates $\vec{r}$ are provided based on ITRS. The line of sight vector from R to X in the according geocentric (GC) frame reads $\Delta\vec{r} = \vec{r}_{\mathrm{X}} - \vec{r}_{\mathrm{R}}$. To derive azimuth and elevation the vector has to be transformed to topocentric coordinates (TC). A right-handed orthogonal system is given by the Up (U), East (E), North (N) frame. The transformation to the TC frame then reads,

$$\vec{\Delta} = \mathbf{R_y}(-\phi_{\mathrm{R}})\mathbf{R_z}(\lambda_{\mathrm{R}})\Delta\vec{r}, \tag{3.1}$$

where $\mathbf{R}$ denotes the rotation w.r.t. the Earth axis in ITRS. Geodetic longitude λ_{R} and latitude ϕ_{R} of the receiver are derived from $\vec{r}_{\mathrm{R}}$. The azimuth α and the elevation angle E of the transmitter in R are then written,

$$\begin{aligned} \alpha &= \mathrm{atan2}(\Delta_{\mathrm{E}}, \Delta_{\mathrm{N}}), \\ E &= \arctan\left(\frac{\Delta_{\mathrm{U}}}{\sqrt{\Delta_{\mathrm{E}}^2 + \Delta_{\mathrm{N}}^2}}\right). \end{aligned} \tag{3.2}$$

The four-quadrant-arcus-tangent atan2 ensures a well defined azimuth. The TC coordinate in Up, East, North direction are Δ_{U}, Δ_{E} and Δ_{N}, respectively. A specular reflection is assumed, i.e. the incident ray, the surface normal and the scattered ray as well as the direct ray lie in the same propagation plane, see Fig. 3.2.

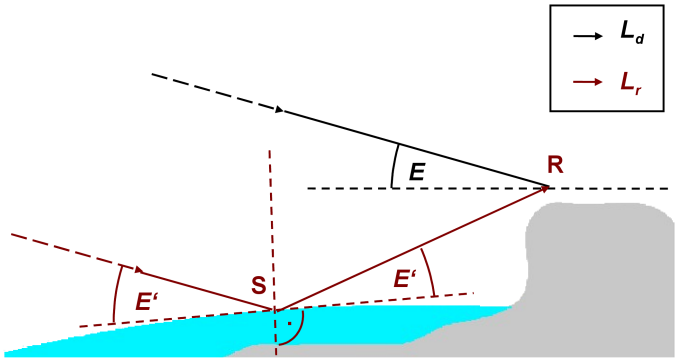

Figure 3.2: Geometry of a specular reflection in a coastal setup. The curvature of the ocean surface affects the geometry. The optical phase path is denoted L_r for the direct signal and L_d for the reflected signal.

According to the law of reflection in the specular point S the elevation of the transmitter and the receiver are equal. If the curvature of the surface is considered, the satellite elevation in the receiver position E will differ from the elevation in the specular point E'. To find a precise specular point, the ocean curvature needs to be modelled. In a first step a planar surface model assuming an apriori height is described. It provides two pieces

of information, the delay to be set between *Master* and *Slave* correlators and an apriori reflection point to find the *Osculation* sphere.

3.1.2 Apriori Plane

An apriori specular point A on a planar surface is derived. The planar surface is defined tangent to the ellipsoidal curvature at R. The deviation between A and the real specular point S is small if it is close to the receiver $\overline{\mathrm{RS}} \ll R$, where R denotes the Earth radius. A scheme of the planar approximation is given in Fig. 3.3.

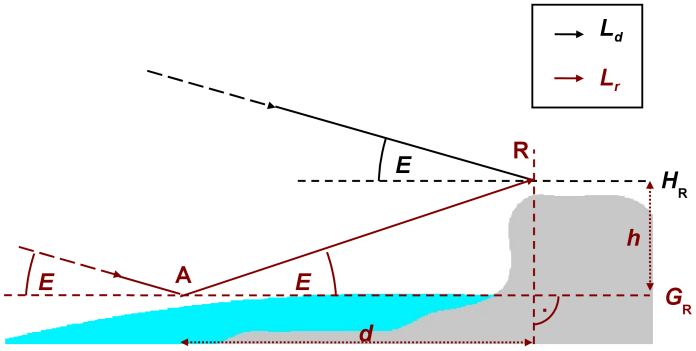

Figure 3.3: Reflection geometry for a planar surface model. An apriori specular point can be derived. For simplicity *Geoid* undulations are neglected. The optical phase path is denoted L_r for the direct signal and L_d for the reflected signal.

The elevation angles E, E' are equal. The planar assumption allows us to define a vertical distance h. It refers to the difference between the ellipsoidal height at the receiver and the *Geoid* undulation there $h = H_\mathrm{R} - G_\mathrm{R}$. The deviation between G_R and G_A is neglected. An estimate of G_R is provided by `EGM-96`. The distance on the plane between A and the projection of R is then written

$$d = \frac{h}{\tan E}.$$

The distance d and the azimuth α in the planar approximation are sufficient to derive spherical coordinates, ϕ and λ for A. A detailed deduction from spherical geometry can be found in the Appendix B.

3.1.3 Osculation Sphere

The apriori model is insufficient for precise altimetry but a *Osculation* sphere can be defined in vicinity of A. This sphere locally fits the curvature of the ellipsoid, as shown in Fig. 3.4. A curvature centered (`CC`) frame is centered in the origin of the *Osculation* sphere, the so-called center of curvature `CoC`. From the geocentric `GC` frame we go to the curvature centered `CC` frame. The transformation vector $\Delta\vec{r}$ will be derived step by step. The starting point is the surface of the `WGS-84` reference ellipsoid, given by

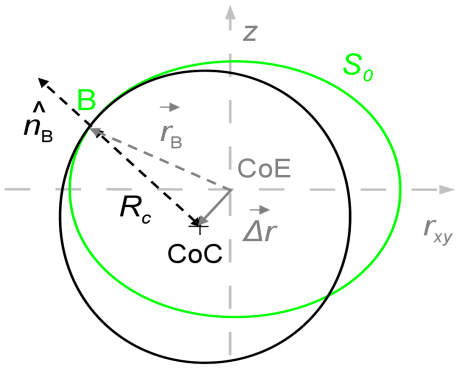

Figure 3.4: *Osculation* of the sphere (black) and the ellipsoid (green). The transformation from GC to CC frame is given, here for simplicity the section equals the meridian plane.

$$\begin{aligned} S_0(x,y,z) &= \frac{x^2}{a^2}+\frac{y^2}{a^2}+\frac{z^2}{b^2} \\ &= 1, \end{aligned}$$

where the semi-major axis is denoted a and the semi-minor axis is b. The apriori reflection point A lies not on the ellipsoid but we find the base point B by projection of A on the surface S_0

$$\vec{r}_{\mathrm{B}} = \frac{\vec{r}_{\mathrm{A}}}{r_{\mathrm{A}}} R(\phi_{\mathrm{A}}), \tag{3.3}$$

where the Earth's radius given by the ellipsoid as a function of the geodetic latitude is denoted $R(\phi)$. The *Osculation* is located in B, i.e. B lies on the sphere and the ellipsoid as well. The transformation of GC coordinates $\vec{r}$ to CC coordinates $\vec{\rho}$ is written

$$\begin{aligned} \vec{\rho} &= \vec{r} - \Delta\vec{r}, \\ \Delta\vec{r} &= \vec{r}_{\mathrm{B}} - \hat{n}_{\mathrm{B}} R_c, \end{aligned}$$

where $\hat{n}_{\mathrm{B}} = \vec{n}_{\mathrm{B}} \left|\vec{n}_{\mathrm{B}}\right|^{-1}$ is the unit vector normal to the ellipsoid that is obtained as follows

$$\vec{n}_{\mathrm{B}} = \left[\begin{array}{ccc} \frac{x_{\mathrm{B}}}{a} & \frac{y_{\mathrm{B}}}{a} & \frac{z_{\mathrm{B}}}{b} \end{array} \right]^T, \tag{3.4}$$

with the GC components of B denoted $(x_{\mathrm{B}}, y_{\mathrm{B}}, z_{\mathrm{B}})$. The radius of the *Osculation* sphere R_c is called radius of curvature. Due to Earth's oblateness R_c is dependent on the location of A and on the orientation of the reflection plane, which is given by the satellite azimuth α. Two perpendicular components, a North-South-component M and an East-West-component N are considered

$$\begin{aligned} R_c &= \left(M^{-1}\cos^2\alpha + N^{-1}\sin^2\alpha\right)^{-1}, \\ M &= a^2b^2\left(a^2\cos^2\phi_{\mathrm{A}} + b^2\sin^2\phi_{\mathrm{A}}\right)^{-\frac{3}{2}}, \\ N &= a^2\left(a^2\cos^2\phi_{\mathrm{A}} + b^2\sin^2\phi_{\mathrm{A}}\right)^{-\frac{1}{2}}, \end{aligned}$$

where a, b are the semi-major and semi-minor axis of the ellipsoid, α is the satellite azimuth and ϕ_{A} is the latitude of the apriori point. A complete deduction of R_c can be found in [Rodgers, 2000]. The parameters of the *Osculation* sphere changes during the reflection event. For a typical event in our Arctic setup, that extends about 5km in North-South direction cf. 2.4(b), R_c lies in the range [6392.093 . . . 6392.454]km and the distance $\Delta\vec{r}$ is about [35.602 . . . 35.933]km.
The transformation form GC to CC coordinates does not change lengths, i.e. the estimation of ellipsoidal height is done in the CC frame without loss of generality. The assumption, that A and the true specular point S are close together $|r_{\mathrm{A}} - r_{\mathrm{S}}| \ll R_c$, allows us to relate the ellipsoidal height of the surface H to the CC radius of S

$$\rho_{\mathrm{S}} = R_c + H.$$

The according CC vector $\vec{\rho}_{\mathrm{S}}$ in the propagation plane is determined by computing the path of the direct signal L_d and the reflected signal L_r, see Fig. 3.5.

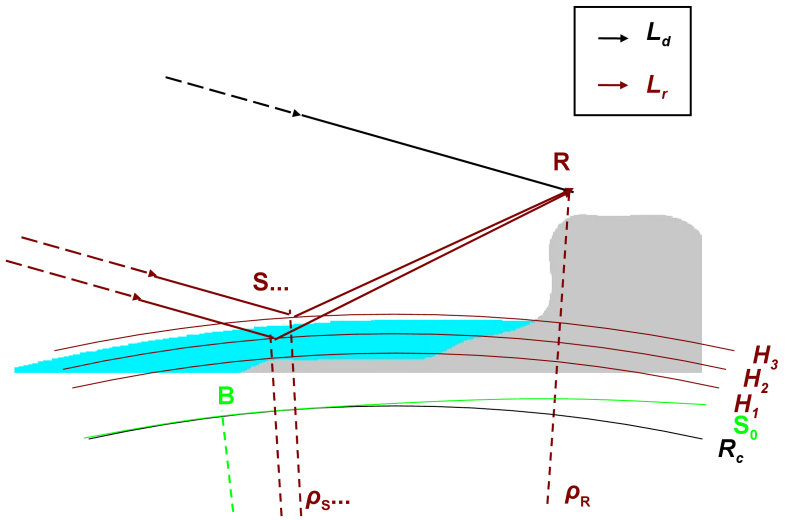

Figure 3.5: Geometry for reflections at different height levels H^j above the *Osculation* sphere. The sphere fits the reference ellipsoid S_0 in the base point B. The location of S can differ from the *Osculation* at B.

For the propagation of the reflected signal, states with different heights H^j are set. The optical paths will be calculated using a comprehensive model of tropospheric and ionospheric refraction. In the CC frame a quasi-analytical model of the signal path in spherical concentric shells will be deduced.

3.1.4 Tropospheric Refraction

The refractive index n of atmospheric gases is only slightly larger than unity. For the highest density at sea level it reaches about 1.0003 and is even closer above. It is convenient to define the refractivity,

$$N = (n-1)\,10^6$$

According to [Bevis et al., 1994] the total refractivity can be modelled from meteorological parameters.

$$\begin{aligned} N &= k_1 \frac{p-e}{T} + k_2 \frac{e}{T} + k_3 \frac{e}{T^2}, \\ e &= \frac{\chi\, p}{\mu + (1-\mu)\,\chi}. \end{aligned}$$

The temperature T, the pressure p and the specific humidity χ in the troposphere are obtained from the ECMWF data base. The partial pressure of water vapour e is determined using the ratio of molar masses $\mu = M_v/M_d$, where M_v refers to water vapour and M_d to dry gases. Vertical profiles of the ECMWF parameters starting at R are shown in Fig. 3.6.

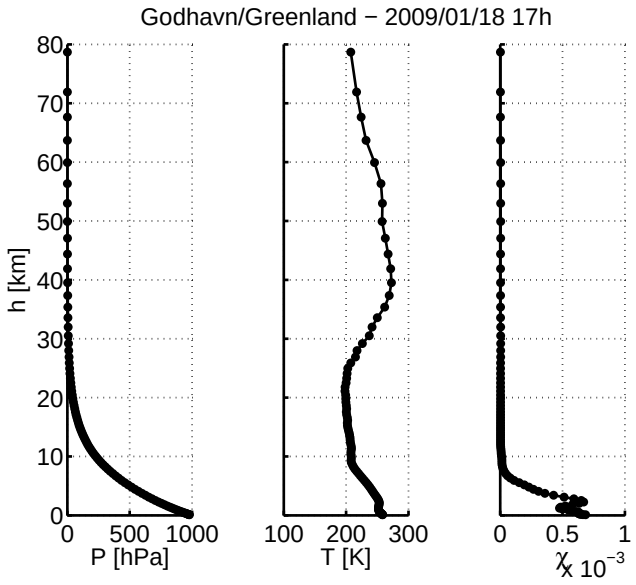

Figure 3.6: Profile of the atmospheric pressure, the temperature and the specific humidity at R for a reference epoch.

The parameters are defined at dedicated height levels $h_m \ldots h_n$ and on a grid with 0.5°x0.5° resolution in latitude and longitude. Above the receiver position ϕ_R, λ_R the refractivity $N^o(h)$ is deduced, see Fig. 3.7.

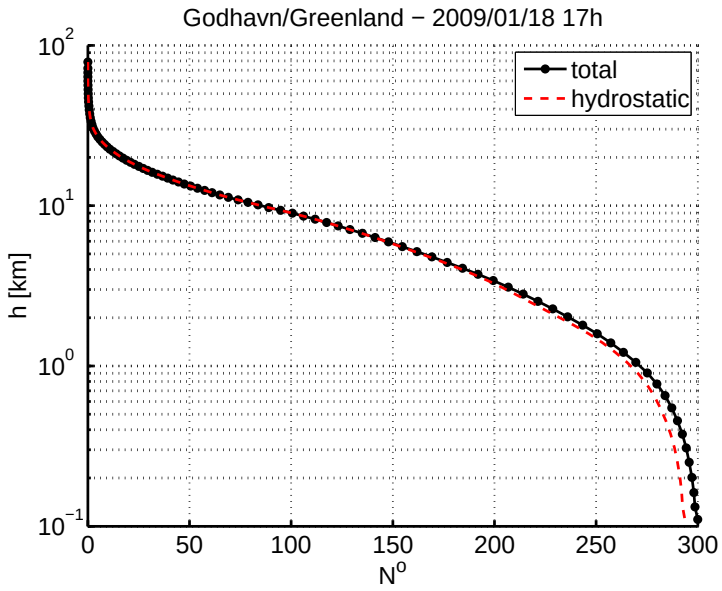

Figure 3.7: Derived profile of the non-dispersive refractivity for the reference epoch. The hydrostatic profile ignores contribution from water vapour. The logarithmic height scale shows that an influence of water vapour on the total refractivity profile appears below 1km.

The barometric height axis h_j of these profiles is uniformly defined w.r.t. the *Geoid*. The *Geoid* undulation G_A at the apriori point provides an ellipsoidal height axis $H = h + G_A$ which is more convenient for the `CC` frame. The profile is transformed to the new height axis, below and above the `ECMWF` boundaries $H_j < H_m, H_j > H_n$ the refractivity profile is extrapolated.

$$\begin{aligned} N^o(H_j) &= N^o(H_m)\, e^{-\frac{H_j - H_m}{\hat{H}}} \qquad j < m \\ N^o(H_j) &= N^o(H_n)\, e^{-\frac{H_j - H_n}{\hat{H}}} \qquad j > n \end{aligned}$$

A scale height of the atmosphere $\hat{H}$ is introduced. The extrapolation has a defined height resolution, a minimum height H_1 and a maximum height H_N (cf. Tab. A.4 in the Appendix). The ellipsoidal height axis H_j finally comprises the troposphere and ionosphere.

3.1.5 Ionospheric Refraction

For the ionosphere model we consider dispersive refraction. We assume an ionospheric structure consisting of time-invariant *F*- and *E-layers*. The distribution of the electron density in each layer is written

$$\eta(H_j) = \hat{\eta} \exp\left[\frac{1}{2}\left(\frac{H_j - H_0}{D}\right) - e^{-\frac{H_j - H_0}{D}}\right], \tag{3.5}$$

where the ellipsoidal height is denoted H_j. Empirical parameters H_0, $\hat{\eta}$, D were used (cf. Appendix Tab. A.5), that are based on similar calculations for *F*- and *E-layers* [Pierce, 1947]. The distribution η for both layers is shown in Fig. 3.8.

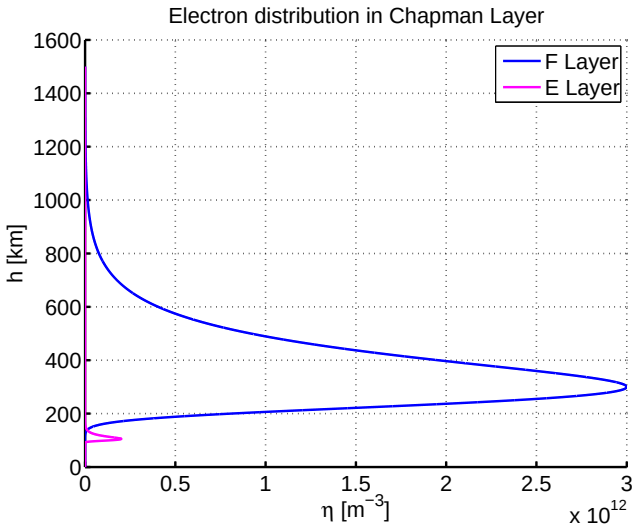

Figure 3.8: The distribution of free electron according to an *E*- and *F-layer*.

The dispersive refractivity is obtained by the following superposition of layers,

$$N^{\mathrm{E,F}}(H_j, f_{\mathrm{L}}) = -\frac{40.3}{f_{\mathrm{L}}^2}\left[\eta^{\mathrm{F}}(H_j) + \eta^{\mathrm{E}(H_j)}\right],$$

where f denotes the L-band carrier frequency. Two carriers have been considered in this method.

f_{L1} = 1575.42MHz GPS L1
f_{L2} = 1227.60MHz GPS L2

3.1.6 Concentric Shells

The non-dispersive and the dispersive refractivity profile N^o and $N^{\mathrm{E,F}}$ are combined to a total refractivity profile by superposition

$$N(H^j, f_{\mathrm{L}}) = N^o(H^j) + N^{\mathrm{E,F}}(H^j, f_{\mathrm{L}}). \tag{3.6}$$

The total refractivity profile covers altitudes from the surface level to the upper boundary of the ionosphere, as shown in Fig. 3.9.
The non-dispersive part vanishes above 100km at the boundary of the homosphere. The two peaks in the overlying heterosphere correspond to the *E*- and *F-layer*. The run of the profile is smooth but a comprehensive analytical description of the signal path is not possible. For a piecewise analytical description, the profile is interpolated to a uniform

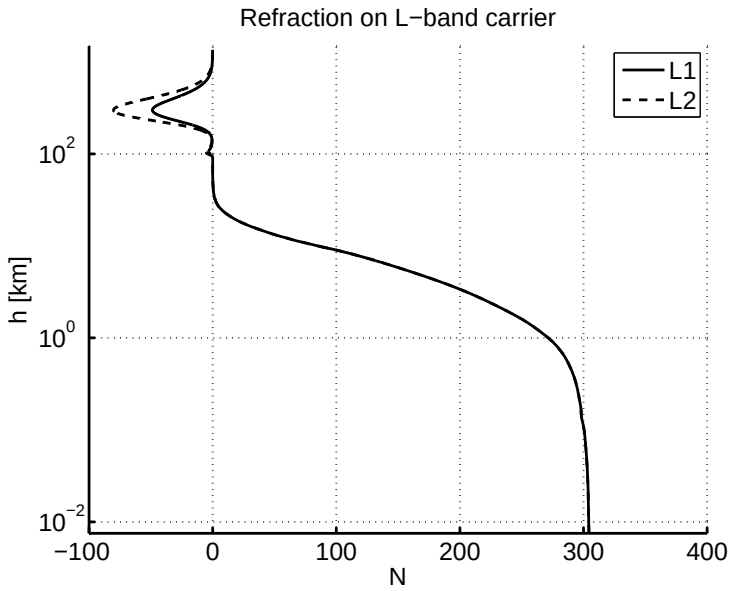

Figure 3.9: Total refractivity on both carriers `L1` and `L2`. A logarithmic height scale is used, non-dispersive refraction is decreasing with the height. Two peaks of the *E*- and *F-layer* are located at 105km and 300km altitude respectively.

step size $dN = 0.01$, that results in variable height steps dH. A lower threshold for dH is introduced to prevent large gradients. If in the troposphere (below 10km) for example, the shell thickness drops below 10m, leading to a large gradient, the according boundary point at H^j is removed from the profile. Two steps are fused then to limit the gradient. Different thresholds for the troposphere, stratosphere and ionosphere are set (cf. Appendix Tab. A.6). The smoothing allows to find a continuous distribution $N(\rho)$ between the discrete points of the profile $N(H_j)$. Spherical shells are defined. The shell boundaries are given by the height axis, the lower boundaries $b_j = H_j$ and the upper boundaries $a_j = H_{j+1}$. In between, the refractivity has a hyperbolic form and is written in the `CC` frame dependent on $\rho = H + R_c$.

$$\begin{aligned} N_l(\rho) &= \frac{\alpha_l}{\rho} + \beta_l, \\ b_l + R_c \leq \quad \rho &\leq a_l + R_c. \end{aligned}$$

The constants α, β are determined for every shell using continuous boundary conditions.

$$\begin{aligned} a_l &= b_{l+1} \\ \lim_{\rho \to a_l} N_l(\rho) &= \lim_{\rho \to b_{l+1}} N_{l+1}(\rho), \\ \lim_{\rho \to a_l} \frac{dN_l(\rho)}{d\rho} &= \lim_{\rho \to b_{l+1}} \frac{dN_{l+1}(\rho)}{d\rho}. \end{aligned} \tag{3.7}$$

The refractivity of adjacent shells is denoted $N_l(\rho)$, $N_{l+1}(\rho)$. The spherical symmetry of $N(\rho)$ in the CC frame and the restriction of propagation to a single plane suggest the use of polar coordinates. Integrals are found to trace the arc Θ and the optical phase path L within the shells, Fig. 3.10.

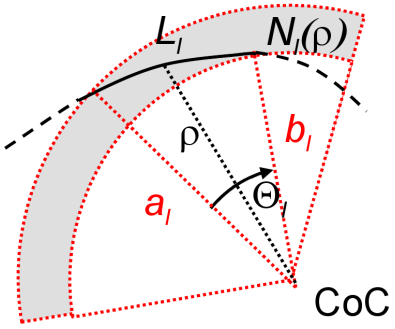

Figure 3.10: Optical phase path and arc within a shell with boundaries a and b.

3.1.7 Ray Tracing

Using the hyperbolic form of N_l, the signal path can be determined analytically. Trace integrals for the optical phase path L and the corresponding arc Θ are adopted from literature [Croft and Hoogasian, 1968]

$$\begin{aligned} \Theta_{a,b} &= \int_a^b d\rho \frac{P}{\rho\sqrt{(\rho\, n)^2 - P^2}}, \\ L_{a,b} &= \int_a^b d\rho \frac{\rho\, n^2}{\sqrt{(\rho\, n)^2 - P^2}}, \end{aligned} \tag{3.8}$$

where $n = n(\rho)$ is the refractive index and P denotes the so called impact parameter. It is defined $P = \rho\, n(\rho) \sin[\beta(\theta, \rho)]$, with β being the angle between the wave vector of the ray and the radius ρ. The notation using the impact parameter facilitates the integration. The angle β changes during propagation, whereas the impact parameter P is preserved along the ray. A proof can be found in literature p.130 [Born and Wolf, 1999]. The evolution of β and the corresponding impact parameter are shown in Fig. 3.11.
For the asymptotic ray P equals $\rho_0 \sin\beta_0$. The iteration of different trace paths leads to the wanted path with P invariant during propagation. In spherical symmetry the trace integrals are determined for each iteration analytically. Next to the direct ray also the incident and the scattered ray can be traced in this way. Fig. 3.12 shows the complete signal path for a reflection event.

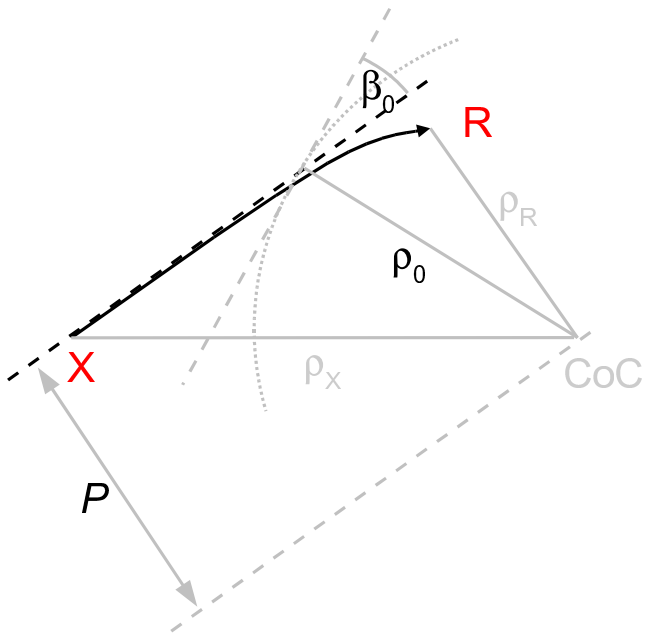

Figure 3.11: Propagation of the bended direct ray (solid black line) in the CC frame, with the corresponding asymptote for non-refractive propagation (dashed black line). The impact parameter P is then the distance of the asymptote from the CoC. The angle β_0 for an arbitrary point on the asymptote lies between the asymptotic wave vector and the radius ρ_0. The principle holds for incident and scattered rays as well.

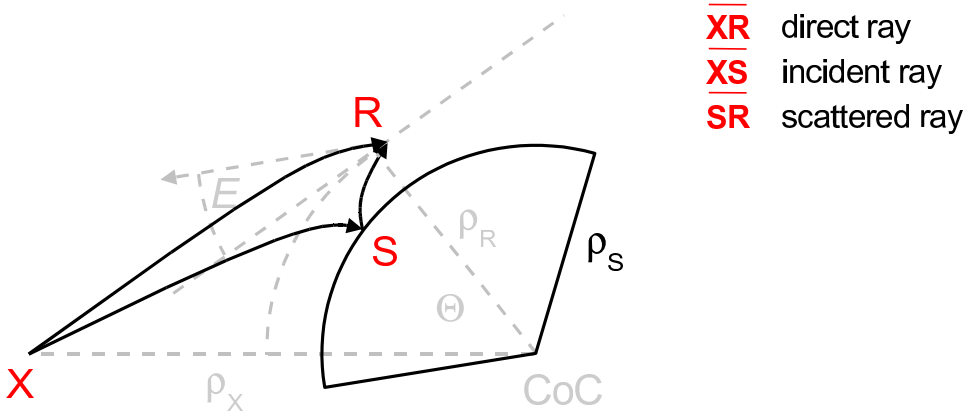

Figure 3.12: All rays of reflection event, i.e. direct, incident and scattered one. Each signal path is determined by an independent ray tracing.

Using a ray tracing algorithm, impact parameters P are determined for each ray and in each shell. Once P is known, total values of the optical phase path L and the corresponding arc Θ are obtained by summation shell by shell

$$\begin{aligned} \Theta &= \sum_i \Theta_{a_i,b_i} \\ L &= \sum_i L_{a_i,b_i}. \end{aligned} \tag{3.9}$$

The trace integrals in eq.(3.8) apply only for either monotonously rising or falling ρ. The trace path of the ray must be divided into parts with defined monotony considering the tangent point and the specular point of ray propagation. A case-by-case analysis of the trace path can be found in the Appendix B. The tracing of the direct ray provides the phase path L_d and the tracing of the incident and scattered ray are combined to the reflected phase path L_r. In contrast to the well defined direct path, the reflected path is calculated varying the surface height. Different states of the reflected signal at height levels H^j are considered in the ray tracing. The interferometric path is formed from the difference

$$L^j_{\text{int}} = L_r - L^j_d, \tag{3.10}$$

where the superscript j indicates the different surface heights. The subscript int is left out in the following parts and the interferometric path is simply L^j.

3.1.8 Linearity of the Model

In contrast to the planar model $L = 2\,(H_{\text{R}} - H)\,\sin E$, see Fig. 3.3, the ray tracing is not based on an explicit relation between the interferometric path L and surface height H. A forward modelling will be used to assess the height dependence of the ray tracing model. The vertical distance $h = H_{\text{R}} - H$ will be considered in the following to have a general reference height at the receiver H_{R} for both models. The planar signal path model $L(h)$ and the interferometric *Doppler* $f(h)$ are linear in h. For ray tracing models a linear relation was found as well. The multipath experiment in [Anderson, 1999] and the `RO` experiment in [Beyerle et al., 2002] show the linearity for completely different geometries. Comparing the planar and the ray tracing model we will prove linearity for the present experiment. The geometry is confined to the *Godhavn* setup, the vertical distance at *Godhavn* was about 670m. Ten equidistant levels h^j are fixed in the range [100...1000]m. The elevation range is set, according to the observations, to [5...15]deg. The corresponding paths L^j and the *Doppler* tracks f^j are plotted in Fig. 3.13 and Fig. 3.14 respectively.
For simplicity only signals on `L1` are considered, the same principles apply to `L2` observations. The paths obtained from ray tracing and planar models are similar. Deviations between both models are more obvious for the *Doppler*, especially at large vertical distances and low elevations. The *Doppler* will be important later on to obtain unambiguous observations. A *Doppler* track can easily be derived from the path

$$f = -\frac{f_{\text{L}}}{c_0}\frac{dL}{dt}. \tag{3.11}$$

The sign of the *Doppler* is fixed by convention. A transmitter departing from the receiver, as it is in the present example, causes a negative *Doppler*. The plots in Fig. 3.13 and 3.14

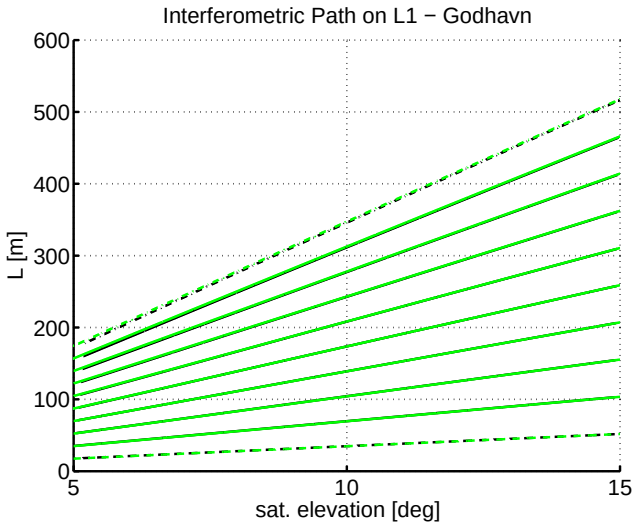

Figure 3.13: Interferometric path length vs. satellite elevation for discrete vertical distances $L(E, h^j)$. Results of the ray tracing model (black) and the planar model (green) are compared. The vertical distance varies between 100m (dashed line) and 1000m (dash-dotted line). The range of elevations (5...15deg) is restricted according to the *Godhavn* experiment.

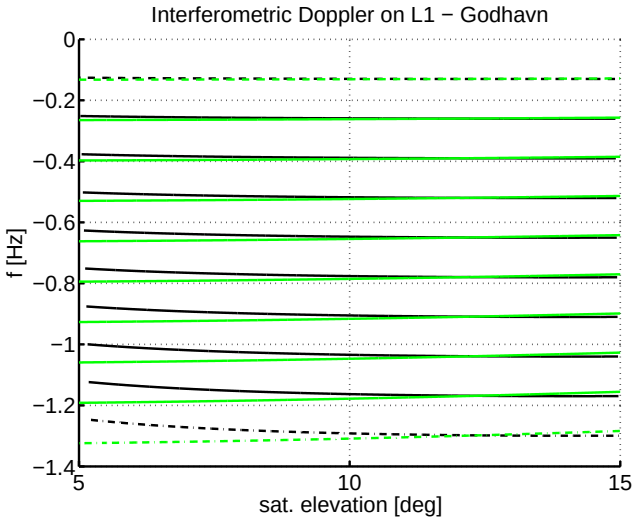

Figure 3.14: Interferometric *Doppler* frequency vs. satellite elevation for discrete vertical distances $f(E, h^j)$. Results of the ray tracing model (black) and the planar model (green) are compared. The vertical distance varies between 100m (dashed line) and 1000m (dash-dotted line). The range of elevations (5...15deg) is restricted according to the *Godhavn* experiment.

shows the elevation dependence $L(E)$, $f(E)$ for different states h^j. To plot explicitly the

relation $f(h)$, stationary states with a fixed elevation must be considered, see Fig. 3.15.

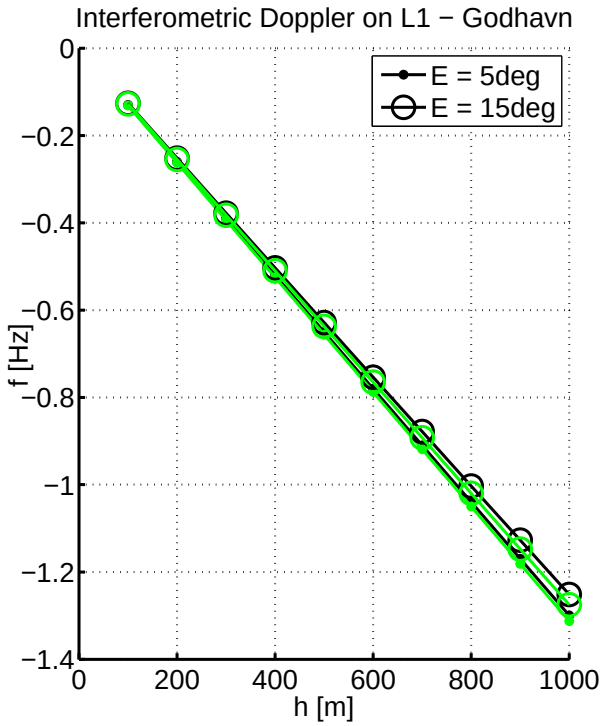

Figure 3.15: Interferometric *Doppler* frequency vs. vertical distance for minimum elevation 5° and maximum elevation 15°. In either case there is a linear relation $f(h)$ for the ray tracing model (black) and the planar model (green).

The plot reveals a linear relation for the planar model and for the ray tracing model. The slope df/dh for the ray tracing model lies in the range [1.30...1.25]mHz per meter between 5° and 15° of elevation respectively. Accordingly the reciprocal $\delta h/\delta f$ provides an estimate for the altimetric sensitivity of *Doppler* observations, it lies in the range [769...800]m per Hz for 5° and 15° respectively. Hence *Doppler* measurement with a precision below 1mHz are required to have a sub-meter altimetric precision. In contrast to the shown model real observations of the *Doppler* are corrupted by noise, so the precision for a single observation is low. The meaning of precise *Doppler* observations for altimetry will be clearer in the following part.

3.2 Height Estimation

This part is dedicated to different ways of height estimation. According to the last part the entire signal path model of the reflection event is modelled assuming discrete altimetric states H^j of the reflecting surface. For each state the excess path model $L(t, H^j)$ is unambiguously determined. Observations ϕ_{int}, on the contrary, are ambiguous and do not refer to a well defined surface height. Though two approaches to solve the ambiguity problem were made:

1. Use continuous phase tracks for an empirical tracking of the surface height leaving an unknown initial height

2. Define a state vector for discrete surface heights and retrieve an optimum height from a correlation with the residual *Doppler*

The first approach is actually a mimic of the Continuous Tracking that was used in previous experiments [Belmonte Rivas and Martin-Neira, 2006] and [Martin-Neira et al., 2002]. A scheme starting with the different approaches for the height estimation is shown in Fig. 3.16.

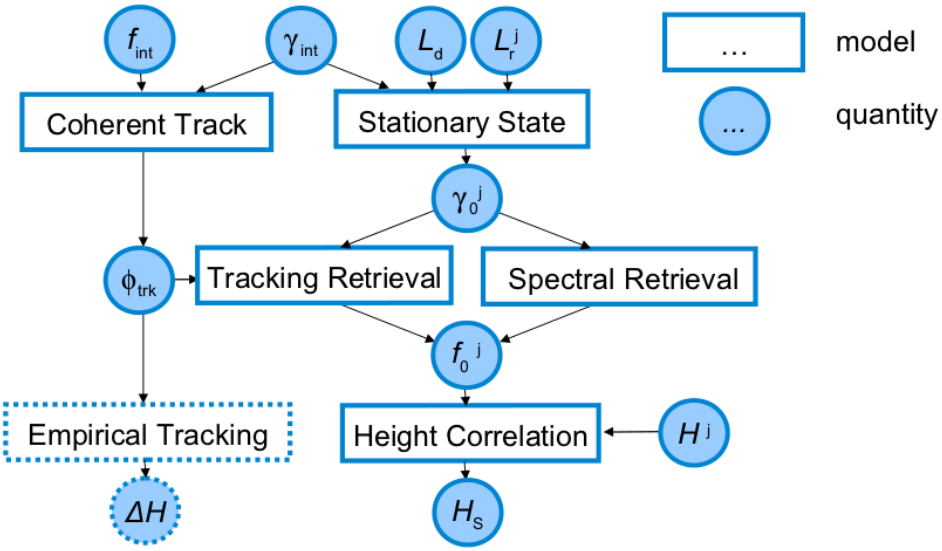

Figure 3.16: Scheme for height estimation. The approach, using continuous tracks for an empirical tracking of changes ΔH, leads not to satisfying results, indicated by dashed frames of the corresponding parts. The approach, starting with a vector of stationary states, splits up in two different retrievals, that both results in height estimates.

The interferometric *Phasor* γ_{int} is the basic observation that is used in both approaches. An estimate of a dominant frequency f_{int} is needed to extract continuous phase tracks. The tracked phase ϕ_{trk} was foreseen to derive height changes ΔH. Due to a lack of coherence this approach was not successful and is therefore rendered with a dotted line. However the

phase tracking algorithm filters out non-coherent observation, an important feature that is needed for the Tracking Retrieval in the second approach.
For the second approach a residual *Doppler* f_0^j is defined. It denotes the frequency residue that remains after model corrections in the *Phasor* γ_0^j. The phase ambiguity is avoided. For model corrections the phase path L_r and L_d, of the reflected and the direct signal respectively, are used. The residual *Phasor* γ_0^j is determined from the path model and the interferometric *Phasor*. The frequency residue f_0^j, that will be called residual *Doppler* in the following, is derived from range rates in a Tracking Retrieval or from the Fourier Transform in a Spectral Retrieval. A fit of f_0^j and the discrete height levels H^j is applied to prove the height correlation of the event and to estimate the specular ocean height H_s.

3.2.1 Phasor Representation

The resolution of phase changes is a requirement for the Continuous Tracking. The limits in the determination of phase changes are examined first. The representation of a *Phasor* using the amplitude A and the phase ϕ is written, $\gamma = A\,e^{-i\phi}$. The phase argument $\phi = \arg\{\gamma\}$ refers to the angle enclosed by the *Phasor* and the abscissa axis as shown in Fig. 3.17.

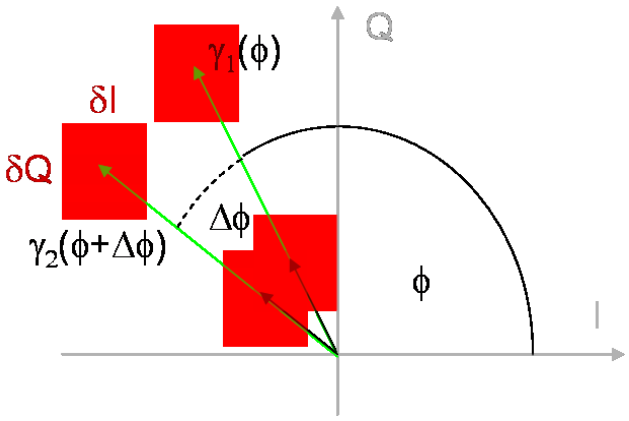

Figure 3.17: Phase argument definition in the complex plane. Fading of the *Phasor* amplitude influences the determination of the phase.

A distinction between phase arguments ϕ and $\phi + \Delta\phi$ is dependent on the amplitude $A = \sqrt{I^2 + Q^2}$. Fig. 3.17 shows an example comparing the *Phasors* $\gamma_1(\phi)$ and $\gamma_2(\phi+\Delta\phi)$. We assume constant uncertainties δI, δQ, that are uncorrelated and span an area as indicated in red. For small amplitudes the uncertainty areas of both *Phasors* overlap and the phase difference is undetermined. For larger amplitudes the *Phasors* are distinct, i.e. the phase difference $\Delta\phi$ can only be resolved when the amplitude is sufficiently large. The determination of phase changes is mainly corrupted by fading which means the loss of amplitude.

3.2.2 Continuous Track

Amplitude fading is a major restriction for Continuous Tracking. Amplitude thresholds, however, are insufficient to filter phase data. The SNR could be used as a threshold but only the amplitude is provided for the raw data, which is affected by the automatic gain control. An accessible threshold parameter for Continuous Tracking is the phase derivative variance. A Maximum Phase Gradient as a threshold to avoid abrupt changes in the phase is described in literature [Ghiglia and Pritt, 1998]. Gradients discussed there, refer to spacial phase variations of $\phi(\vec{r})$. In analogy phase rates can be considered to describe variations of $\phi(t)$. A Maximum Phase Rate must be larger than the interferometric frequency f_{int} to preserve any observation. An estimate for f_{int} can be derived from the spectrum of the interferometric signal. For a ground-based receiver less than 1000m above the reflecting surface and a small range of elevations $[5...15]^\circ$, f_{int} varies less than 0.1Hz, see Fig. 3.15. For a moving platform in contrast the deviation of a dominant frequency f_{int} is not possible. The empirical tracking is based on the assumption that the mean period of a phase cycle is related to the dominant interferometric frequency $T = f_{\text{int}}^{-1}$. The detection of completed phase cycle, i.e. one circulation of the *Phasor* in the complex plane, that agrees with the cycle period T, is the principle of the tracking algorithm. Fig. 3.18 shows examples for such phase cycles in the complex plane.

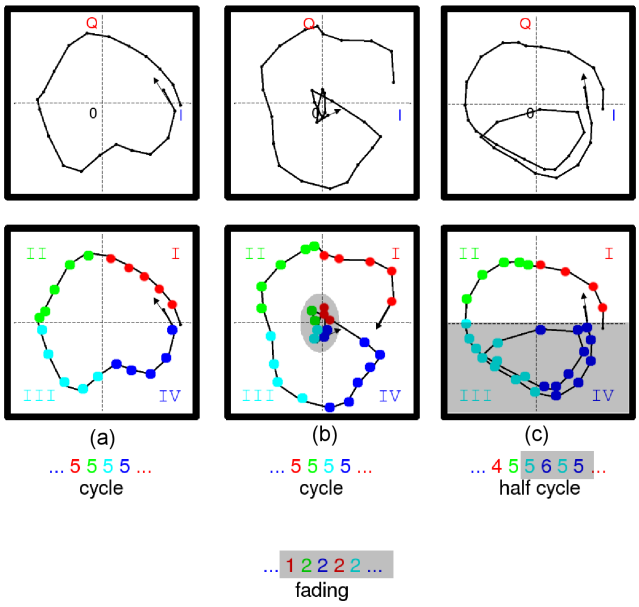

Figure 3.18: Scheme of Continuous Tracking for cycles in the complex plane. Three different scenarios are shown.

According to those examples the concept of the phase tracking algorithm will be explained. A running-mean-filter with a 50ms interval is applied to reduce the noise. For clarity in Fig. 3.18 only every tenth sample is shown, so the spacing between samples increased to $\Delta t = 50$ms. In part (a) we see a complete cycle over $N_a = 20$ samples which corresponds to a period $T_a = N_a\,\Delta t = 1000$ms and roughly agrees with $f_{\text{int}} \approx 1$Hz. The color-

coded sampling in the lower part shows that the samples are equally distributed over the quadrants. Hereby the cycle follows an ascending order (I,II,III,IV). The number of samples per quadrant is $N_q = 5$. Concluding the example we formulate two conditions for a continuous phase cycle that are necessary for the tracking algorithm:

1. the phase cycle passes through all quadrants of the complex plane either in ascending or descending order, i.e. I,II,III,IV,I,II... or IV,III,II,I,IV,III...

2. the expected samples within the phase cycle $N = T/\Delta t$ are uniformly distributed to the quadrants $N_q = N/4 \pm 0.1N$ with an empirical tolerance.

Those conditions limit the variance of the phase rate. The running-mean-filter smooths out variations on a scale below 50ms. The example in Fig. 3.18(b) shows how those conditions are violated if the signal fades, i.e. the amplitude permanently decreases to noise level. After a complete cycle with an ascending order (I,II,III,IV) and $N_q = 5$ for all quadrants, the order is lost and N_q decreases below the tolerated level. In such a case a correction of the phase cycle is impossible.
The example in Fig. 3.18(c) shows another violation of the conditions given above when a short decrease in amplitude occurs. The quadrant order is disrupted (I,II,III,IVIII,IV) as a half cycle occurs and quadrants are skipped. This phenomenon indicates a beat interference at slightly different frequencies. Then nodes of the beat envelope occurs where amplitude is shortly lost. In contrast to fading a single node causes no permanent loss of coherence.
The given examples are a case study, the algorithm continuously filters all samples of an event. When a crossing between the quadrants is detected and an ascending or descending order is found, cf. condition (1.), the samples of one complete cycle are clustered to the quadrants and condition (2.) is checked. If both conditions are met, a phase increment $\Delta_i = \pm 1$ is recorded for the last epoch of the cycle t_i. The tracked phase at t_i results from the sum over all previous cycles,

$$\phi_{\mathrm{trk}}(t_i) \quad = \quad \sum_{j<i} \Delta_j. \tag{3.12}$$

The spacing $t_i - t_{i-1} = T_i$ of epochs in the tracked phase is variable. It depends on the duration of the ith cycle. A regular time grid is achieved when we interpolate the tracked phase rate,

$$\frac{d\phi_{\mathrm{trk}}}{dt} \quad = \quad \frac{\Delta_i}{T_i}. \tag{3.13}$$

For a convenient plot of the time evolution the phase rate is used rather than phase observations. A permanent drift of the observations is avoided, only an offset rate occurs, as shown in Fig. 3.19.
The raw data was determined using a standard unwrapping operator,

$$\frac{d\phi_{\mathrm{raw}}}{dt} \quad = \quad \frac{d}{dt}\mathfrak{U}\{\arg(\gamma_{\mathrm{int}})\} \tag{3.14}$$

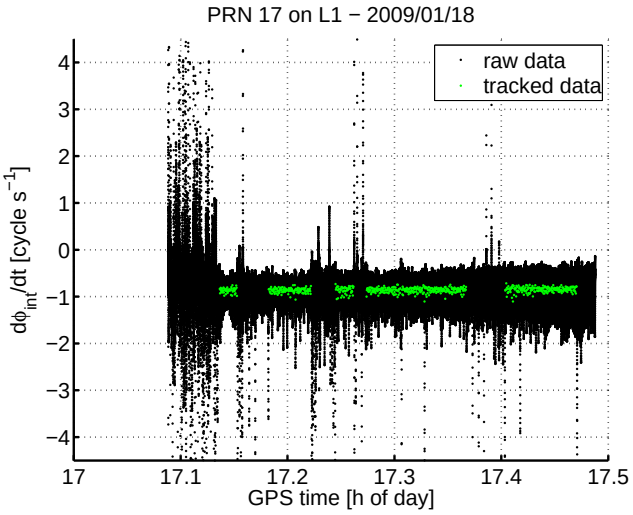

Figure 3.19: Phase rate data versus time of the event. Continuously tracked data (green) and raw data (black) are plotted.

The unwrap operation $\mathfrak{U}\{\}$ corrects the phase angle by adding $\pm 2\pi$, when jumps greater than the tolerance of π occur. Fig. 3.19 shows large gaps between tracked observations even for specular conditions, like for PRN 17 on 2009/01/18. Continuous tracks occur only in absence or large variations in the raw phase rate. From the phase tracking studies we conclude that an unwrapping to a continuous phase is only possible if the standard deviation of the phase rate is small, otherwise cycle slips will corrupt the phase observation. The Maximum Phase Rate must be set relative to f_{int}. An empirical tolerance used so far could be replaced by the standard deviation $\sigma(d\phi/dt)$. A threshold for the amplitude is not reasonable to detect coherent tracks, as can be seen in Fig. 3.20.
The empirical phase tracking actually yields two results. It acts as a filter, passing only coherent observations of the interferometric *Phasor* γ_{int}. Furthermore it acts as an unwrapping algorithm, summing up phase cycles in a continuous track ϕ_{trk}. Those phase tracks are continuous, i.e. changes in the phase are related to changes in the signal path. To derive relative changes of the surface height only few tracks are available. Due to fragmentation of continuous tracks, only short isolated height profiles could be derived. A validation of those isolated profiles is impossible, ancillary height information with a sufficient spacial resolution is not available. So the first approach based on a Continuous Tracking strategy is not useful to retrieve continuously height estimates of the ocean surface in the *Godhavn* experiment.

3.2.3 Stationary Reflection State

The loss of coherence, i.e. a failure of phase unwrapping can be avoided if the signal path model is introduced into the observation at the earliest point of the approach. A stationary reflection state can be created, if the temporal evolution of the phase observation is stopped using the temporal evolution of the phase model. A state vector for different realisations of the model can be constructed

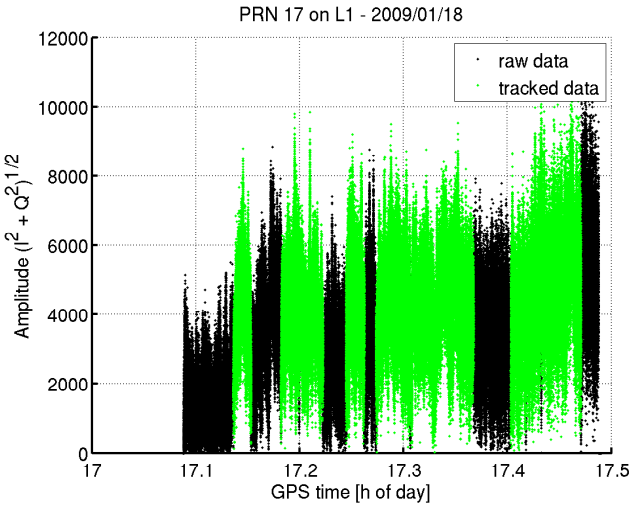

Figure 3.20: *Phasor* amplitude versus time of the event. Continuous tracks (green) and raw data (black) are plotted. The amplitude is not affected by the phase tracking algorithm just a filter effect is visible.

$$\gamma(H,t) \quad = \quad \begin{bmatrix} \gamma(H^1,t) \\ \vdots \\ \gamma(H^N,t) \end{bmatrix},$$

where $\gamma(H^j,t) = \gamma^j(t) = \exp[-ik_0\, L^j(H^j,t)]$ is the model for the jth state in *Phasor* representation. Fig. 3.21 shows the different states of the system in a simplified model. The interferometric observation is written $\gamma_{\rm int}(t) = A_r\, \exp[-ik_0\, L(t)]$ in *Phasor* representation. Then the vector of pseudo-stationary states is defined in *Phasor* representation as follows,

$$\begin{aligned} \gamma_0^j(t) &= \gamma_{\rm int}(t)\, \gamma^j(t)^* \\ &= A_r \exp[-ik_0\, (L(t) - L^j(t))]. \end{aligned} \tag{3.15}$$

It is a vector of pseudo-stationary states, as each state can have a time dependent residual $\gamma_0(t)$. The real stationary state is defined by the following two equivalent conditions,

$$\begin{aligned} \arg\{\gamma_0(H,t)\}|_{H=H_{\rm s}} &= \text{const.} \\ f_0(H)|_{H=H_{\rm s}} &= 0. \end{aligned} \tag{3.16}$$

A constant phase argument of γ_0 is equivalent with a vanishing residual *Doppler* f_0. If the *Doppler* vanishes a stationary state is reached at the desired height $H = H_{\rm s}$.
An example of observation and model that create a stationary state is shown in Fig. 3.22. Phase variations in the observation agree with the model.

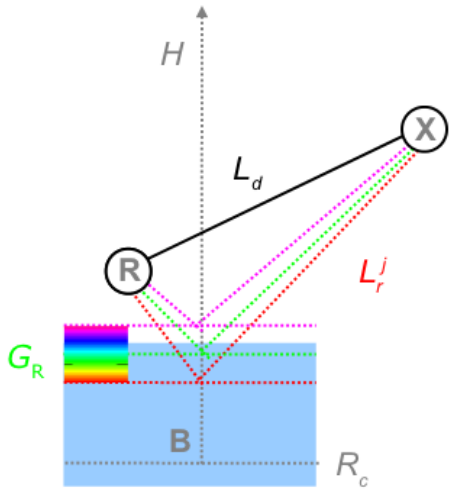

Figure 3.21: Direct and reflected paths of the signal are shown neglecting the Earth's curvature and refraction. The origin of the height axis lies in the base point B that osculates the ellipsoid, R_c denotes the radius of the osculating sphere. Different states with corresponding heights are color-coded. They range from a lower limit (red) to an upper limit (violet). As a reference height (green) the *Geoid* undulation G_R at the receiver position is used.

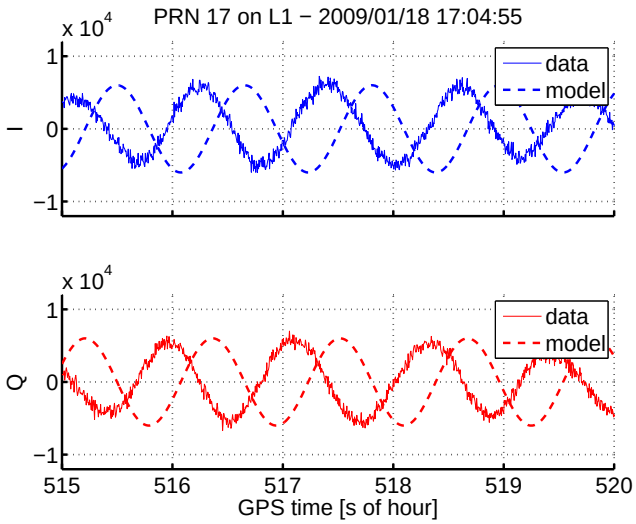

Figure 3.22: In-phase and quad-phase component vs. GPS time. Variations in a continuous track are plotted, the model is given by the dashed line, only the initial phase remains unmodelled

The first condition in eq.(3.16) is actually hard to prove, as the phase argument is ambiguous and the constant is unknown. The residual *Doppler* f_0^j is a suitable discriminator

for the stationary state. We propose two different retrieval for f_0^j, one in the time domain and another one in the frequency domain.

3.2.4 Tracking Mean Retrieval

The advantage of stationary states for reflection ranging are already known. The possibility of longer coherent integration intervals if phase observations are counter-rotated (to a stationary state) was already reported in [Caparrini et al., 2003]. For the retrieval in the time domain we use this advantage. An unwrapped residual phase is derived and coherently integrated afterwards. The risk of cycle slips in the unwrapped phase is reduced for a stationary state. The unwrapped residual phase is written

$$\phi_0^j(t) \quad = \quad \mathfrak{U}\{\arg(\gamma_0^j(t))\} + N. \tag{3.17}$$

The phase argument $\arg(\gamma_0^j)$ corresponds to a wrapped phase angle. A standard unwrapping is sufficient because the residual phase in a quasi stationary state will show only few wraps. The unwrap operation $\mathfrak{U}\{\}$ corrects the phase angle by adding $\pm 2\pi$, when jumps greater than the tolerance of π occur. The ambiguity N remains unknown. The samples $\phi_0^j(t)$ are coherently integrated up to $T_c = 1\text{min}$ to reduce the noise, cf. coherent integration in [Caparrini et al., 2003]. The residual *Doppler* is deduced from coherent tracks, that were described in the beginning of this section,

$$\begin{aligned} f_0^j &= -\left.\overline{\frac{\Delta\phi_0^j}{T_c}}\right|_{\text{tracks}} \\ &= -\frac{1}{n}\sum_{\text{tracks}}^{n}\frac{\Delta\phi_0^j}{T_c} \\ &= -\frac{1}{n\,T_c}\sum_{\text{tracks}}^{n}\Delta\phi_0^j. \end{aligned} \tag{3.18}$$

The mean indicated by the bar is an incoherent integration over n samples that covers different continuous tracks. The total duration over all tracks is $n\,T_c$ and $\Delta\phi_0^j$ is the unambiguous phase difference after coherent integration. The sign is chosen as a convention to obtain a positive *Doppler* observation for a decreasing phase path. The integrated residual phase is shown for different states in Fig. 3.23.
The slope of the track is characteristic for state and the residual *Doppler* is derived for each state. The states are pseudo-stationary, the slope is small compared to the phase rate data, that was shown Fig. 3.19, but in general the slope does not vanish completely. The *Doppler* range for `L1` is larger than for `L2`. The sections of the track used for the *Doppler* retrieval are depicted with colored markers. Gaps in the track correspond to incoherent observations, which are masked by the filter. A second event on 2009/01/14 is considered. Tracks for the residual *Phasor* for this event are shown in Fig. 3.24.
The comparison of both events in Fig. 3.23 and Fig. 3.24 shows, that the Tracking Retrieval fails when we underrun a minimum of coherence and the residual *Doppler* cannot

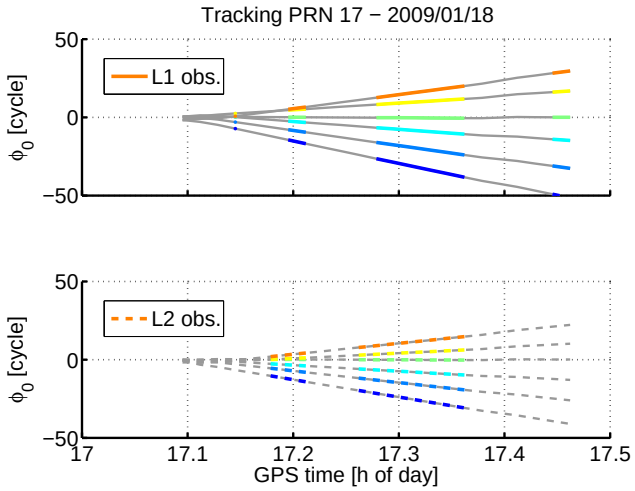

Figure 3.23: Residual unwrapped phase vs. GPS time, for a smooth ocean on 2009/01/18. The tracks refer to 6 different states. The color indicates the state. The colored markers refer to coherent observation, the gaps in between refer to incoherent parts. Coherence does not necessarily coincides for L1 and L2 observations. A residual *Doppler* is derived from the slope of each track.

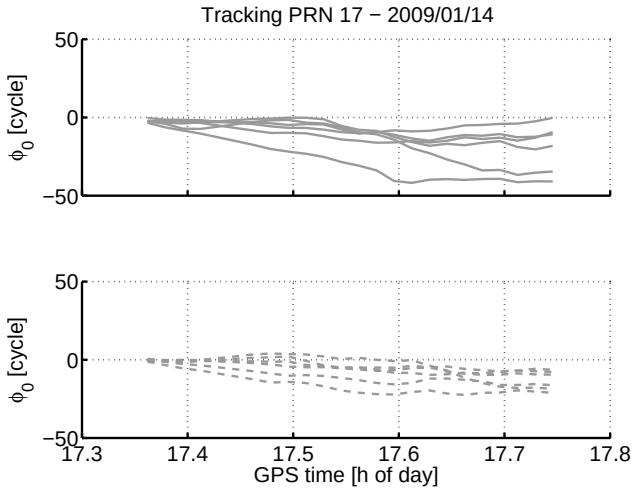

Figure 3.24: Residual unwrapped phase vs. GPS time, for a rough ocean on 2009/01/14. The tracks refer to 6 different states. No coherent observations were detected for this event. The slopes of the tracks are predominantly falling.

be estimated from the slope of a continuous track. Cycle errors, that occur in incoherent parts, distort the slope and cannot be corrected in those cases masked by the coherence filter. For the shown events the residual tracks are integrated to a 1min sampling to filter noise. The general weakness of the Tracking Retrieval is its dependence on continuous tracks. The problem of coherence is tightened in the time domain. In the following we will

see, that a transformation to the frequency domain will facilitate the determination of the residual *Doppler* f_0.

3.2.5 Spectral Maximum Retrieval

The second strategy starts also with the residual *Phasor* $\gamma_0(t)$. The Fourier Transformation is used to go to the spectrum in the frequency domain which is formally written as

$$\Gamma_0(\nu) \quad = \quad \left| \int_T dt\, \gamma_0(t)\, e^{-i\,2\pi\,\nu\,t} \right| . \tag{3.19}$$

Only the amplitude of the Fourier Transform is regarded. The duration of the whole event is denote T and ν is a frequency, that we call Fourier Frequency to distinguish it from the *Doppler* Frequency. The meaning of both frequencies is essentially the same but by convention the *Doppler* Frequency has opposite sign, i.e. $f = -\nu$. To understand the retrieval in the frequency domain, the Fourier Transform of constant residual *Phasor* γ_0 is considered

$$\begin{aligned} \Gamma_0(\nu) \quad &= \quad \left| \gamma_0 \int_T dt\, e^{-i\,2\pi\,\nu\,t} \right| \\ &\rightarrow \quad |\gamma_0\, \delta(\nu)| \,. \end{aligned} \tag{3.20}$$

For limes $T \rightarrow \infty$, i.e. a long duration of the event, the spectrum yields the Dirac-Delta-Distribution $\delta(\nu)$. This distribution vanishes for $f \neq 0$ but has a dominant peak at $f = 0$. The peak value of Γ_0 will be larger for longer intervals T. That means, a constant residual *Phasor* γ_0, which identifies a stationary state, can be detected by a characteristic peak at a residual *Doppler* $f_0 = 0$. The according estimate is derived from the maximum of the spectrum,

$$f_0^j \quad = \quad -\hat{\nu}^j|_{\max(\Gamma_0^j)} \tag{3.21}$$

where the transformation from ν to f is included. Spectra of the residual *Phasor* for a specular event on 2009/01/18 are shown in Fig. 3.25.
The states of the event are pseudo-stationary, a dominant peak in the spectra is obvious but in general the residual *Doppler* does not vanish completely. For both carriers `L1` and `L2`, the peaks are sharp and the residual *Doppler* is determined easily, according to eq.(3.21). Analog to the Tracking Retrieval, the second event on 2009/01/14 is considered. Spectra of the residual *Phasor* for this event are shown in Fig. 3.26.
The comparison of both events in Fig. 3.25 and Fig. 3.26 shows, that the Spectral Retrieval applies for both events. For the event on 2009/01/14 the peak height is significantly smaller. Next to the first-order maxima, secondary maxima exist. However, the residual *Doppler* can still be retrieved. The Spectral Retrieval persists, as we see, in cases when the Tracking

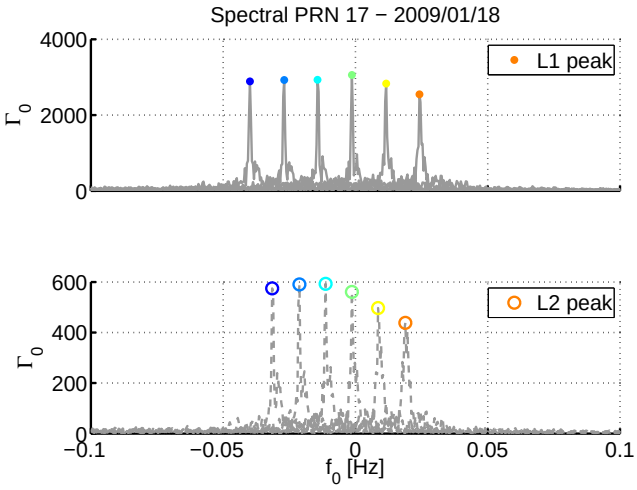

Figure 3.25: Spectra of the residual *Phasor* for a frequency interval around zero, for a smooth ocean on 2009/01/18. Residuals for `L1` and `L2` are shown. For each carrier 6 states are considered leading to 6 plotted spectra, the peak in each spectrum is color-coded.

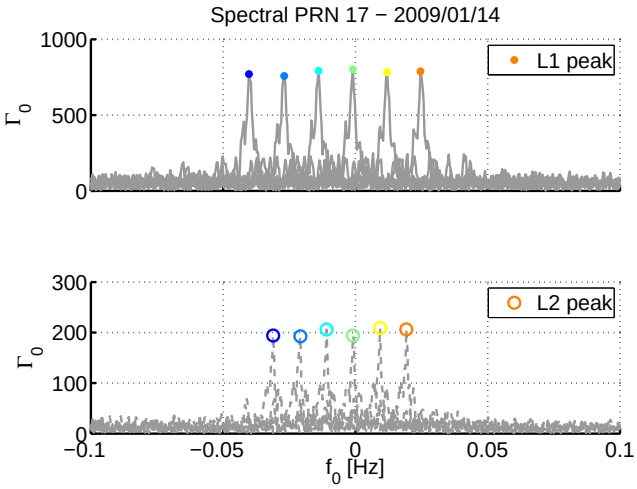

Figure 3.26: Spectra of the residual *Phasor* for a frequency interval around zero, for a rough ocean on 2009/01/14. Residuals for `L1` and `L2` are shown. For each carrier 6 states are considered leading to 6 plotted spectra, the peak in each spectrum is color-coded.

Retrieval fails. It is not restricted to continuous phase segments, according to eq.(3.19) the spectrum covers all observations of the event, a filter for coherent observations is not necessary. By design disturbing influences, e.g. secondary multipath reflections, will be separated from the first-order specular peak in the spectrum. The retrieval yields discrete estimates f_0^j for the states completely analog to the Tracking.

	H_s [m]	$\delta H/\delta f_0$ [m/Hz]
tracking L1	25.20	780
tracking L2	24.82	996
spectrum L1	25.23	777
spectrum L2	25.46	997

Table 3.1: Comparison of tracking and spectrum results.

3.2.6 Correlation of Surface Height and Residual Doppler

The linear relation $f(h)$ has already been examined for the planar and for the ray tracing model in Fig. 3.15. Going from the model to the residual *Doppler* f_0 linearity will be preserved, if the phase path residual equals the sum of phase path model and interferometric phase path

$$L_0^j \quad = \quad L_{\text{int}} + (-L^j).$$

A problem will occur, if the phase path representation of the *Phasor* $\gamma \rightarrow L$ is not precise, i.e. cycle errors persist after unwrapping. Assuming a precise representation, the model and the residual L_0^j will depend linearly on the height. Linearity for the height dependence of f_0 then follows in analogy to eq.(3.11). The transformation from vertical distances h to ellipsoidal heights H does not alter the phase path, so linearity will not be affected. Based on the linear relation $H(f_0)$, a linear fit can be applied

$$H(f_0) \quad = \quad a\, f_0 + H_s.$$

which yields the surface height $H(0) = H_s$. In case of a precise unwrapping, as we found for the event on 2009/01/18, see Fig. 3.23, $H(0)$ can be estimated using a linear fit for both *Doppler* retrievals, see Fig. 3.27.
For this event both retrievals show similar results. In case of non-precise unwrapping, as we found for the event on 2009/01/14, see Fig. 3.24, the estimation of $H(0)$ fails for the Tracking Retrieval, see Fig. 3.28(a).
The lack of continuous tracks causes a failure of height estimation if the residual Doppler is retrieved. The estimates $H(0)$ clearly differs between L1 and L2 and they are out of the shown range. For the Spectral Retrieval, in contrast, an estimation $H(0)$ is possible and an agreement for L1 and L2 is shown, see Fig. 3.28(b). A broader comparison of the retrievals w.r.t. the performance for ocean roughness is postponed to the results.
Next to the surface height the fit provides the altimetric sensitivity deduced from the slope. The fitting results, heights and sensitivity are summarized in Tab. 3.1.
The dispersion between L1 and L2 is larger for the tracks, a reason could be the difference in the continuous tracks for both carriers, cf. Fig. 3.23. The comparison shows that L2 observations in general are less sensitive for altimetry. Recalling the sensitivity derived from $f(h)$, see Fig. 3.15, the comparison shows that for the presented example of retrievals the sensitivity is conserved within the limits [769...800]m per Hz that refer to 5° and 15°

(a)

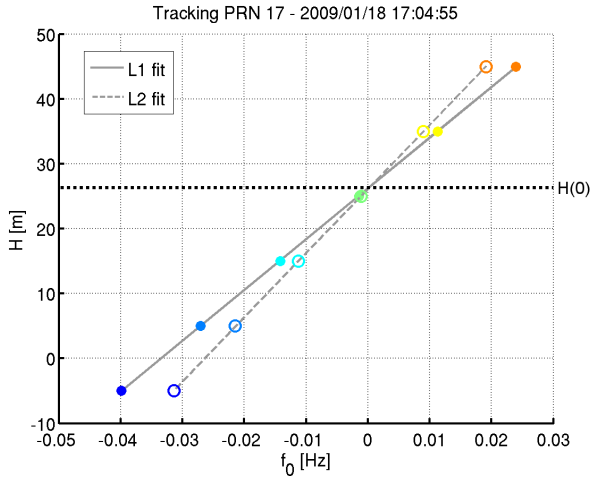

(b)

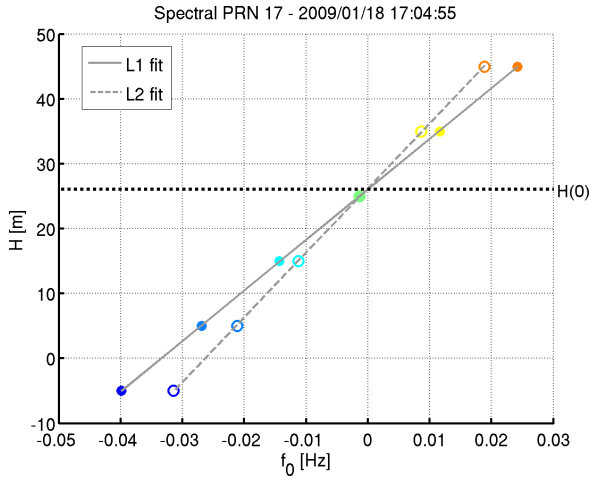

Figure 3.27: The height parameter H vs. the residual *Doppler* frequency f_0, for a smooth ocean on 2009/01/18. **(a)** The height is estimated using the Tracking Retrievals. **(b)** The height is estimated using the Spectral Retrievals. Height estimates in both cases are given for a vanishing residual *Doppler* at $H(0)$. Results from `L1` and `L2` show no obvious dispersion.

of elevation. A loss of correlation between model and observation is given by the fitting error

$$\begin{aligned} \epsilon_{\text{fit}} &= \frac{\sigma\left(f_{\text{fit}} - f_0^j\right)}{f(H_{\text{s}})} \\ f_{\text{fit}} &= (H^j - H_{\text{s}})/a \end{aligned}$$

where $f(H_{\text{s}})$ can be approximated by 0.8Hz according to Fig. 3.15 and the chosen example here. The correlation can be lost, for example, if the unwrapping operation creates cycle

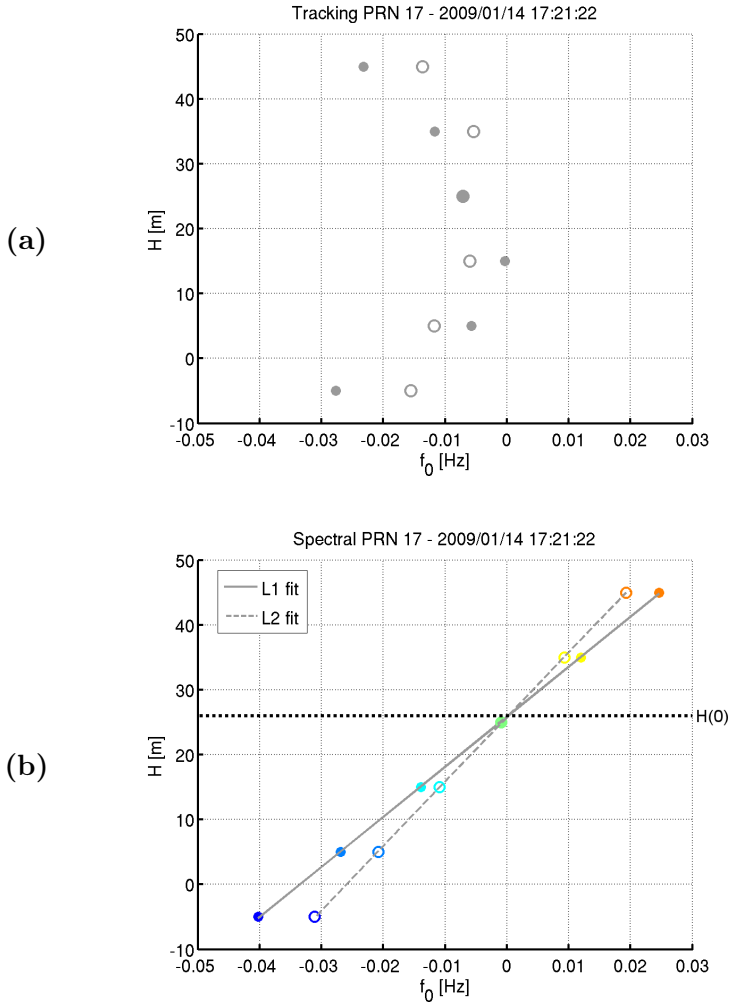

Figure 3.28: The height parameter H vs. the residual *Doppler* frequency f_0, for a rough ocean on 2009/01/14. **(a)** The height estimation fails using the Tracking Retrieval, as there is no correlation. **(b)** The height estimation using the Spectral Retrieval is successful. In this case a linear fit is applied for `L1` and `L2`, respectively, to estimate $H(0)$.

slips during the Tracking Retrieval which depend on the altimetric state. We claim in this method that the fitting error ϵ_{fit} is less than 10%. This restriction filters and removes outliers, i.e. observations that cannot be described by the specular model.

3.2.7 Airborne Application

Although this thesis concentrates on the ground-based *Godhavn* experiment. The focus is shifted for the last part of this chapter to a *Zeppelin* airship experiment. The use of a flying receiver platform complicates the retrieval of carrier observations. The concept of a stationary state allows us to correct the platform motion and to estimate the surface height simultaneously. Due to the absence of coherence in the raw data, a Spectral Retrieval will

be used.
In contrast to a rather small sector over the ocean for the ground-based setup, where reflection tracks are driven by changes of the transmitter elevation, in the flight experiment the trajectory guides the reflection tracks along the ground track of the airship (cf. Fig. 2.4 and Fig. 3.29).

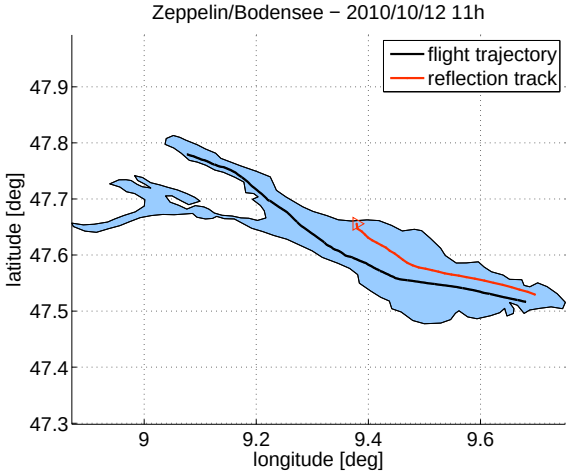

Figure 3.29: Ground track of the trajectory and the reflection track of PRN 2 over *Lake Constance*. For the initial epoch, 11h00 GPS time, the *Zeppelin* airship and the reflection point are located in the eastern end of the lake. Only that part of the reflection track is shown which is situated over the lake.

A comparable track in the same range of elevations [18...5]° is not achievable with a ground-based setup. The shown event is open for different tasks e.g. to retrieve the lake topography. But in agreement with the previous parts we will focus on the estimation of a single surface height.
To minimize baseline effects in the interferometric signal the up-looking and the down-looking antenna are separated by only 40cm. Then the crucial disturbance of the interferometric signal arise from variations in the receiver height. A precise estimation of the trajectory, as shown in Fig. 3.30, is needed to correct the interferometric observations.
A precise signal path requires the correction of various aspects, the antenna baseline, the tropospheric refraction, the ellipsoidal curvature etc. For a precise height estimate a ray tracing model as it was introduced above would be adequate. However, we focus here not on precision but on the concept of a stationary state and the following planar model of the interferometric path will be used

$$\begin{aligned} L(t) &= 2\,h(t)\,\sin E(t), \\ h(t) &= H_{\mathrm{R}}(t) - H_{\mathrm{S}}. \end{aligned}$$

where H_{R} is the height of the receiver platform and H_{S} is the height of the specular surface. In contrast to residuals in the ground-based case, see eq.(3.15), the counter-rotation in the

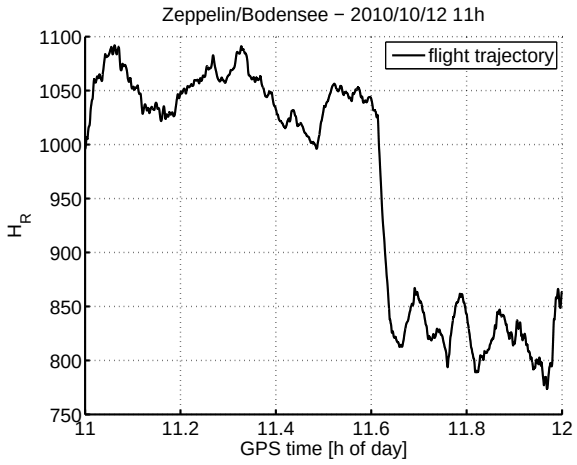

Figure 3.30: Ellipsoidal height of the receiver vs. GPS time. The trajectory of the whole flight was estimated using a kinematic retrieval, the part shown here refers to the duration of the reflection event in Fig. 3.29 above.

flight experiment has to compensate time variations of the receiver height H_{R}. To achieve pseudo-stationary states the evolution $E(t)$ and $H_{\mathrm{R}}(t)$ are considered

$$\begin{aligned}
\gamma_0^j &= \gamma_{int}\,\gamma^{j*} \\
&= \gamma_{int}\,{\gamma_{\mathrm{R}}}^*\,\gamma_{\mathrm{S}}^{j*}, \\
\gamma_{\mathrm{R}} &= \exp\left[-i\frac{2\pi}{\lambda}\,H_{\mathrm{R}}(t)\sin E(t)\right], \\
\gamma_{\mathrm{S}}^j &= \exp\left[+i\frac{2\pi}{\lambda}\,H^j \sin E(t)\right],
\end{aligned}$$

where γ_{R} denotes a *Phasor* model to correct for the changes induced by the receiver trajectory and γ_{S}^j is the state vector for different levels of the reflecting surface. Four equidistant height levels have been chosen in the interval of ellipsoidal height [0...600]m. For the whole reflection event of PRN 2 the Spectral Retrieval is used to obtain residual frequencies f_0 given by the peak maxima, see Fig. 3.31(a). Apart from the correction γ_{R} and the simplified model the procedure is equal to the ground-based experiment. The specular height H_{S} is determined using a linear fit, see Fig. 3.31(b).
A precise validation of the estimated height would require an integration of local tide gauges, that are available for *Lake Constance*, into the global WGS-84 system. This task is postponed to further analysis, a comparison for the estimated height is given by a GNSS reference station that was installed during the campaign and provides height estimates in WGS-84. The station was not located on the lake level but on a roof of a building close-by. The height difference between lake and reference station was not measured, what introduced a bias of [10...20]m. The location of the reference station is shown on the image in Fig. 3.32.
The estimation of the station height gives 462m above the ellipsoid, compared with the

(a)

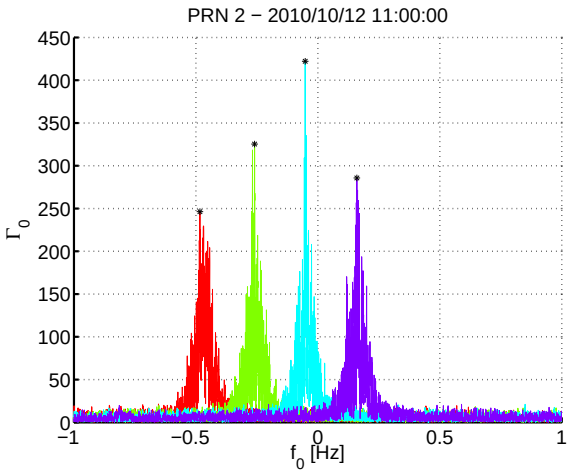

(b)

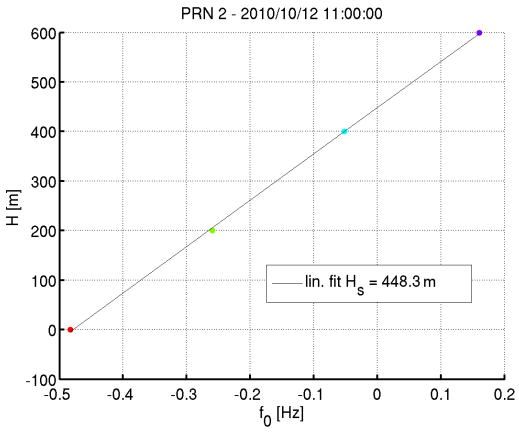

Figure 3.31: Spectral retrieval for an airborne reflection event of PRN 2. **(a)** Spectra of the residual states color-coded for different surface height levels. **(b)** Ellipsoidal surface height vs. residual frequency, a linear fit was applied to determine H_s.

estimated surface height 449m, the difference is well in the bias range.

Figure 3.32: Image of the EADS facilities in Immenstaad, Bodensee. The reference station was set up on the roof with a distance to the shore of about 450m, along the drawn line.

Chapter 4

Results

The first focus for the results will be the sensitivity of the *Doppler* retrievals to noise that is introduced by surface roughness. Based on simulations, differences of the Tracking and the Spectral Retrieval are analysed. In the second part the altimetric results are presented. The ocean roughness leads to a different performance of the retrievals. A formal precision is derived for both cases. A comparison to an ocean surface model and a tidal analysis follow for the longest time series. In the last part of the results the error sources for the height estimation are analysed.

4.1 Ocean Roughness

The influence of ocean roughness on the height estimation is different for the Tracking or the Spectral Retrieval. Using simulations we will show that an increasing standard deviations of the surface σ_ξ increases the noise in the observations. The sensitivity of the Tracking and the Spectral Retrieval to the noise will be compared.

4.1.1 Signal Path Model

The description of the method included a simple planar and a complex ray tracing model. We saw that both models provide a linear relation $f(h)$ and a height estimation is possible for both models. The ray tracing allows a precise modelling of refraction and the Earth's curvature but there is no benefit to use it to describe roughness. Therefore it is sufficient to consider the planar model for a simulated signal path that is written as

$$\begin{aligned} L_{\mathrm{sim}}(t) &= 2\,h_{\mathrm{sim}}(t)\,\sin E(t) \\ L^j(t) &= 2\,h^j\,\sin E(t) \\ h_{\mathrm{sim}}(t) &= h_{\mathrm{s}} + \xi(\sigma_\xi, t) \end{aligned} \tag{4.1}$$

where the path $L_{\mathrm{sim}}(t)$ depends on a variable vertical distance $h_{\mathrm{sim}}(t)$. The roughness term ξ corresponds to normally distributed noise with a standard deviation σ_ξ and zero mean. The vertical distance to the specular point h_{s} is constant and in fair agreement with the *Godhavn* experiment it is set to 700m. The signal path model $L^j(t)$ is defined at different

Scientific Technical Report STR 12/04
DOI: 10.2312/GFZ.b103-12049

height levels h^j from an interval [600...800]m. Kinematics of the transmitter are modelled for 25min in an elevation interval [5...15]°, assuming a constant rate of elevation dE/dt. Using the phase path $L_{\rm sim}$ and L^j, respective *Phasors* are built from the wrapped phase $\phi(t) = \mathrm{mod}[2\pi\, L/\lambda, 2\pi]$ in its complex form $\gamma(t) = \exp[-i\,\phi(t)]$. In agreement with the *Phasor* representation in eq.(3.15), a residual *Phasor* is derived from the simulation $\gamma_{\rm sim}(t)$ and the models $\gamma^j(t)$,

$$\gamma_0^j(t) \quad = \quad \gamma_{\rm sim}(t)\,\gamma^j(t)^* \tag{4.2}$$

where * indicates the complex conjugate of the *Phasor*. One realisation γ_0^j for each value of σ_ξ will be calculated. Based on each residual γ_0^j, the Tracking and the Spectral Retrieval of the residual *Doppler* will be performed. To characterise the simulations w.r.t. coherence of reflection, we use the Fraunhofer Criterion, cf. eq.(1.2), to calculate an elevation threshold $\hat{E}$, that gives an upper limit of coherence

$$\hat{E} \quad = \quad \arcsin \frac{\lambda_{\rm L}}{32\,\sigma_\xi}, \tag{4.3}$$

where $\lambda_{\rm L}$ denotes the *L-band* wavelength and σ_ξ is the standard deviation of the surface displacement ξ.

4.1.2 Tracking Mean Retrieval

The procedure to obtain an unwrapped phase and to derive a mean *Doppler* of the event is described by eq.(3.17) and eq.(3.18). For 5 roughness realisations with different $\sigma(\xi)^k$, unwrapped phase tracks ϕ_0^j are derived, respectively. Three realisations ($k = 1, 2, 3$) in the lower roughness regime are shown in Fig. 4.1, 4.2 and 4.3.

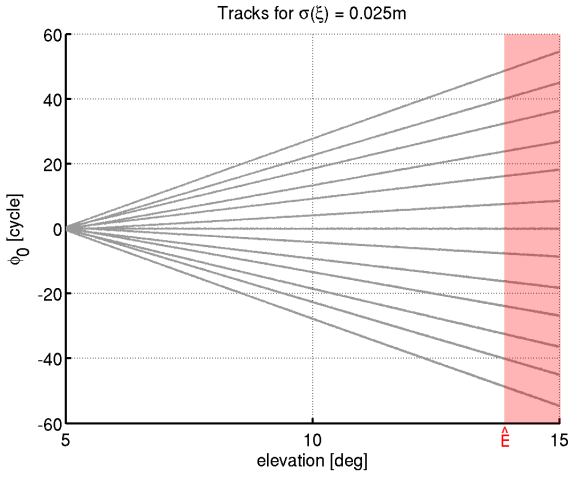

Figure 4.1: Residual phase vs. elevation of the transmitter. The tracks are continuous.

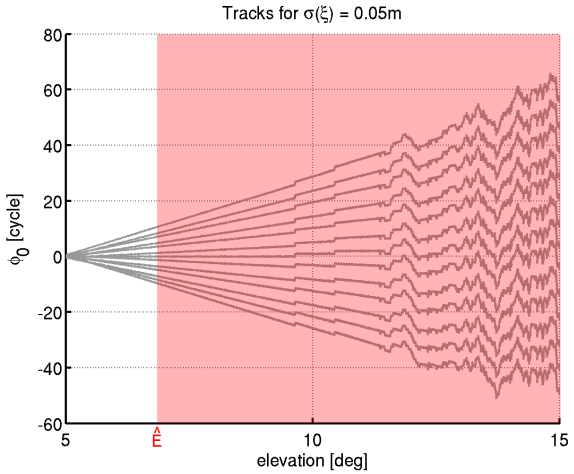

Figure 4.2: Residual phase vs. elevation of the transmitter. The tracks are continuous at low elevations but cycle slips occur at higher elevations.

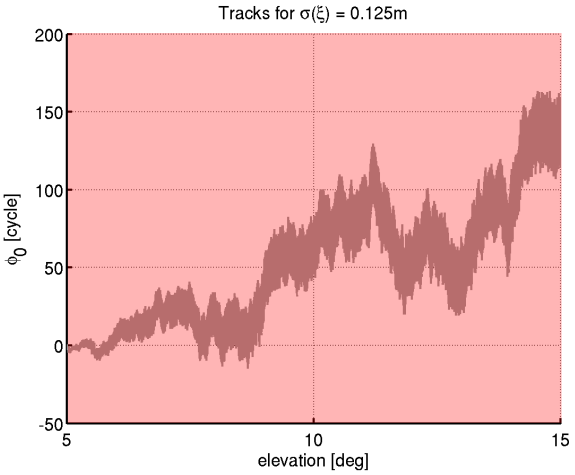

Figure 4.3: Residual phase vs. elevation of the transmitter. The tracks are not continuous.

The elevation axis is equivalent to a time axis, as a constant elevation rate can be assumed. According to 13 different levels h^j there are 13 curves in each plot. The roughness is increasing from plot to plot as indicated by $\sigma(\xi)$. For lowest roughness conditions ($\sigma(\xi) =$ 2.5cm in Fig. 4.1) continuous phase tracks are derived with a monotone slope in each track as it is expected for a specular reflection. At larger roughness conditions ($\sigma(\xi) > 5$cm, see e.g. Fig. 4.3), unpredictable cycle slips are produced by the unwrap algorithm and the continuous track is lost. A limiting case occurs at $\sigma(\xi) = 5$cm, shown in Fig. 4.2, when coherence is preserved at low elevations but cycle slips disturb the tracks a higher elevations.

4.1.3 Spectral Maximum Retrieval

The procedure to obtain a Fourier Transform and to determine the *Doppler* Peak of the event is described by eq.(3.19) and eq.(3.21). For 3 different roughness realisations the spectra Γ_0^j are shown in Fig. 4.4, Fig. 4.5 and Fig. 4.6.

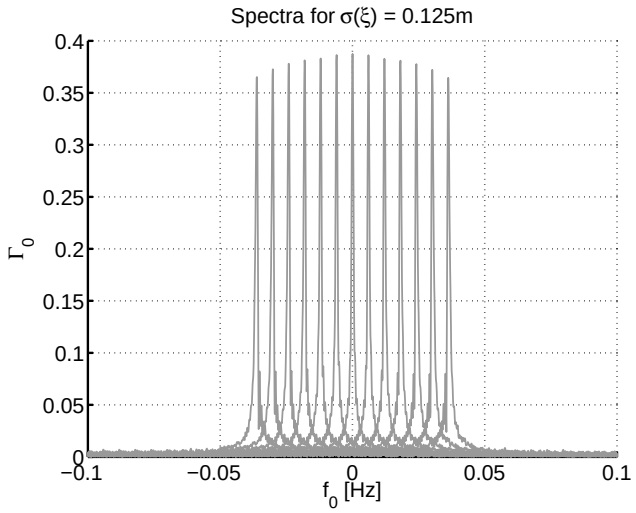

Figure 4.4: Spectra obtained from the residual *Phasor*. The distinct peaks are separated from the noise level.

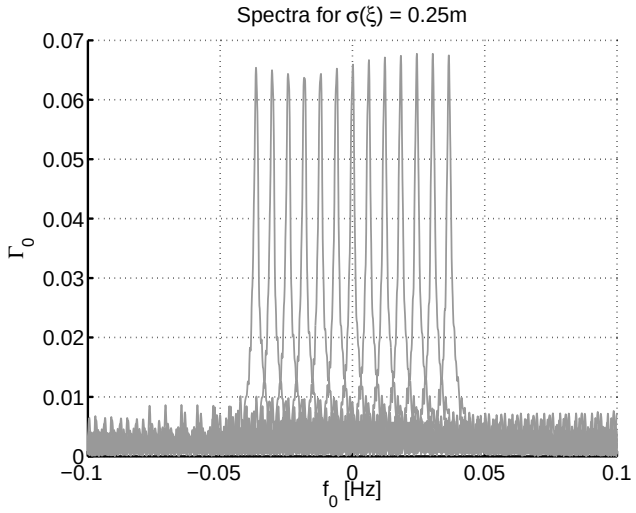

Figure 4.5: Spectra obtained from the residual *Phasor*. The distinct peaks are separated from the noise level.

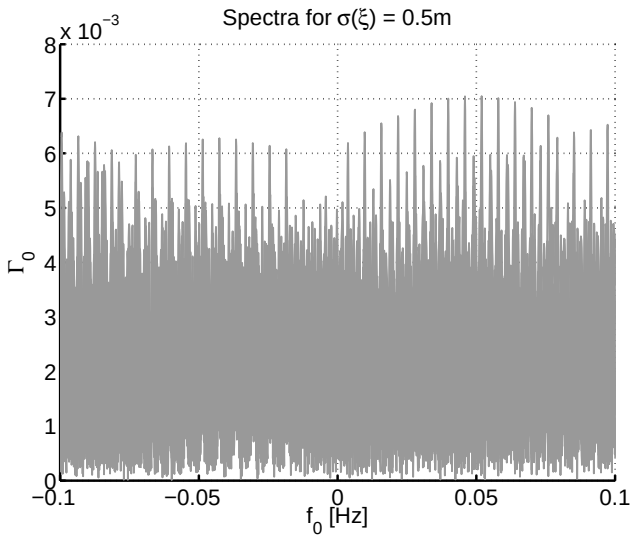

Figure 4.6: Spectra obtained from the residual *Phasor*. There are no distinct peaks that can be separated from the dominating noise.

The frequency axis has been transformed to *Doppler* frequencies. According to the 13 different levels h^j, 13 peaks raise from the noise level in the plots. The roughness is increasing from plot to plot as indicated by $\sigma(\xi)$. For all roughness conditions $\sigma(\xi) < 50$cm, e.g. Fig. 4.4 and Fig. 4.5 distinct peaks occur in the spectra and residual *Doppler* frequencies can be derived. Only for the largest roughness considered $\sigma(\xi) = 50$cm the noise dominates the spectra and no distinct peak can be seen.

4.1.4 Comparison of Estimates

The residual *Doppler* f_0^j has been derived by both retrievals. The same model that provides the linear relation $f(h)$ has been used. However correlation between the residual *Doppler* and the predefined levels h^j does not appear identically for the different retrievals. To quantify a bias in height estimation, a residual height is defined $\delta H^j = h_\mathrm{s} - h^j$. The correlation between f_0^j and δH^j is plotted for all roughness realisations in Fig. 4.7.

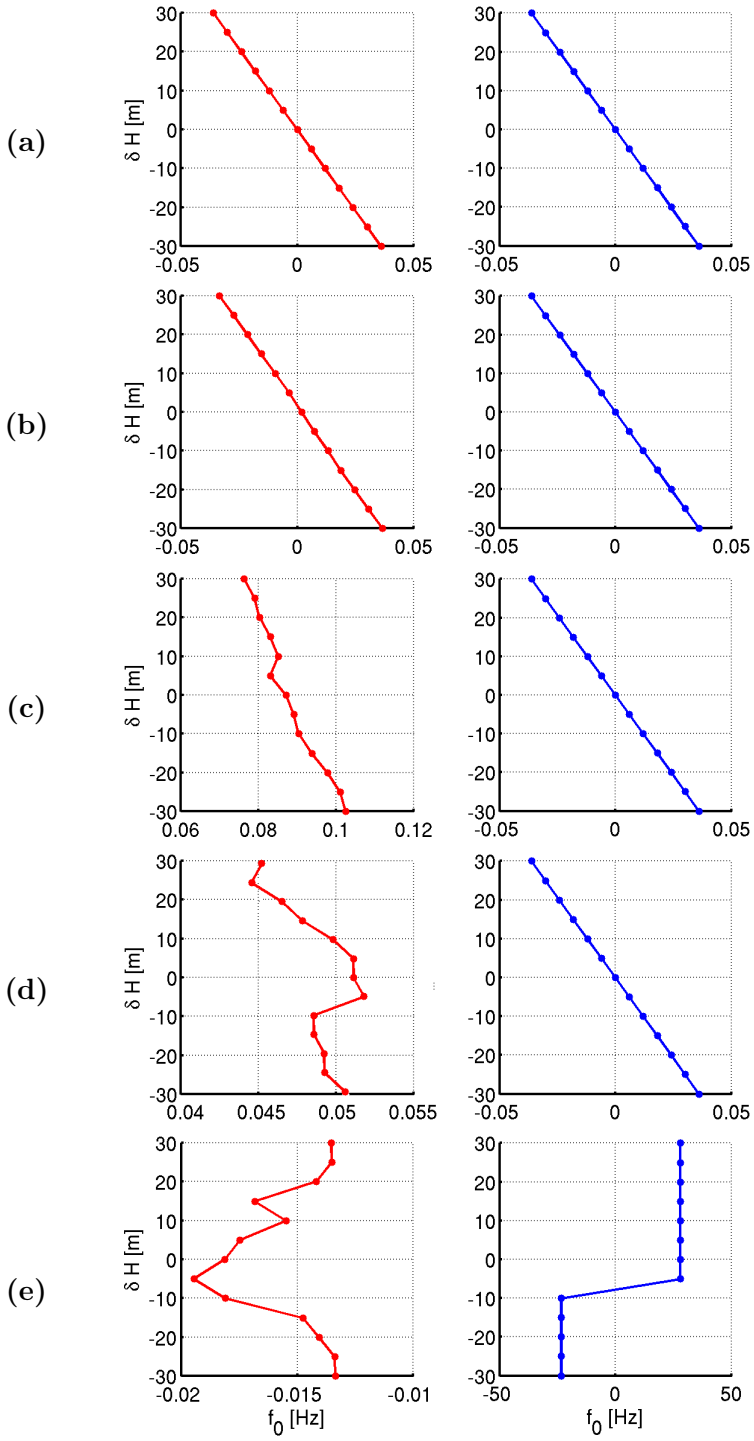

Figure 4.7: Correlation between residual *Doppler* and residual height for different roughness realisations. **(a)** $\sigma(\xi) = 2.5$cm, **(b)** $\sigma(\xi) = 5$cm, **(c)** $\sigma(\xi) = 12.5$cm, **(d)** $\sigma(\xi) = 25$cm, **(e)** $\sigma(\xi) = 50$cm. Tracking Retrievals are plotted in red, Spectral Retrievals are plotted in blue.

For a roughness larger than $\sigma(\xi) = 5$cm the correlation in the Tracking Retrieval is lost. For the Spectral Retrieval, however, the correlation still persist for a roughness 5 times larger $\sigma(\xi) = 25$cm. The retrieval is unbiased if the correlation curve crosses the origin. The Tracking Retrieval still shows a correlation at a roughness $\sigma(\xi) = 12.5$cm but it is biased by $\delta H > 50$m. The comparison between both retrievals shows that the Spectral one is less sensitive to roughness. The failure of the Tracking Retrieval is gradually, a continuous increase of cycle slips occurs in the tracks that corrupt the residual *Doppler*, see Fig. 4.1, 4.2, 4.3. In contrast to the gradual decline of the Tracking, the Spectral Retrieval fails abruptly, due to the noise level that finally overlap the specular peaks, see Fig. 4.6.

There are quantities for each retrieval that characterise the roughness performance. Fig. 4.8(a) shows the frequency standard deviation $\sigma(f)$, that is derived from the range rate along the track to characterise the Tracking Retrieval. Fig. 4.8(b) shows the peak to noise ratio `PNR` that is determined to characterise the Spectral Retrieval. Both characteristics are plotted vs. roughness.

The limiting case for the Tracking Retrieval at $\sigma(\xi) = 5$cm correspond to $\sigma(f) \approx 0.25$Hz, for a larger standard deviation coherence is lost and the retrieval fails. The limiting case for the Spectral Retrieval occurs when the peak amplitude is in the range of the noise level, e.g. the peak to noise ratio $\hat{\Gamma}_0/\epsilon$ is in the range $[1 \ldots 10]$. To define this limit, the noise level ϵ need to be determined. For the simulations it is sufficient to assume that the majority of Fourier Amplitudes Γ_0 falls upon the noise and the noise amplitude ϵ is determined from the histogram peak of Γ_0. Where we assume a distribution of Γ_0, that is similar to the Dirac-Delta-Distribution with only one distinct peak.

(a)

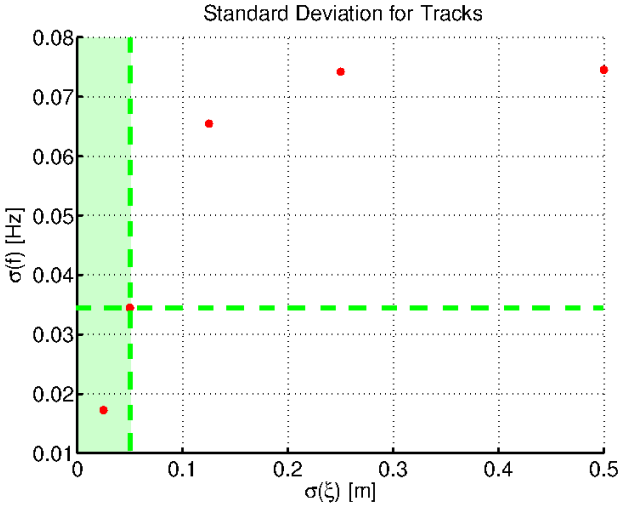

(b)

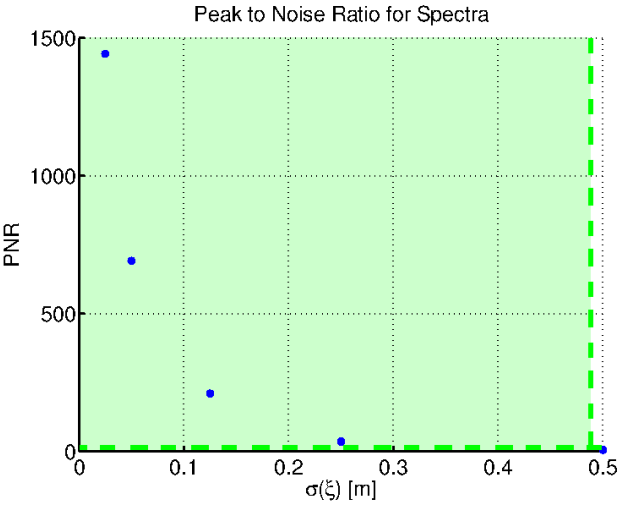

Figure 4.8: Characteristics of the retrievals. **(a)** standard deviation along the *Doppler* track, **(b)** peak to noise ratio in the spectrum. Each vs. standard deviation of the surface. The green shaded area shows the roughness regimes, where the retrievals preserve the correlation between residual *Doppler* and surface height.

4.2 Altimetry

In the previous part simulations predicted that the Spectral Retrieval rather than the Tracking Retrieval can be applied for height estimations of a rough ocean surface. Considering the reflection events during the *Godhavn* campaign, the performance under experimental conditions will be shown in the up-coming part. The application of both retrievals will be evaluated regarding the occurrence of continuous tracks on the one hand and the occurrence of spectral peaks on the other hand. Altimetric time series of different lengths will be presented using the Tracking and the Spectral Retrieval. A formal precision for both retrievals and the deviation from an ocean surface model will be calculated. Finally a tide spectrum is derived for the *Godhavn* location using estimates from the long time series of the Spectral Retrieval.

4.2.1 Application of the Retrievals

The simulation results in Fig. 4.7 have shown, that a loss of phase continuity due to cycle slips leads to a failure of the Tracking Retrieval. The detection algorithm of continuous tracks, used to filter phase data, has been explained on p.60 ff. Hence the occurrence of coherent observations restricts the application of this retrieval. Unfortunately during the major part of the campaign, observations were not coherent. Fig. 4.9 shows the distribution of coherent observations during the campaign.

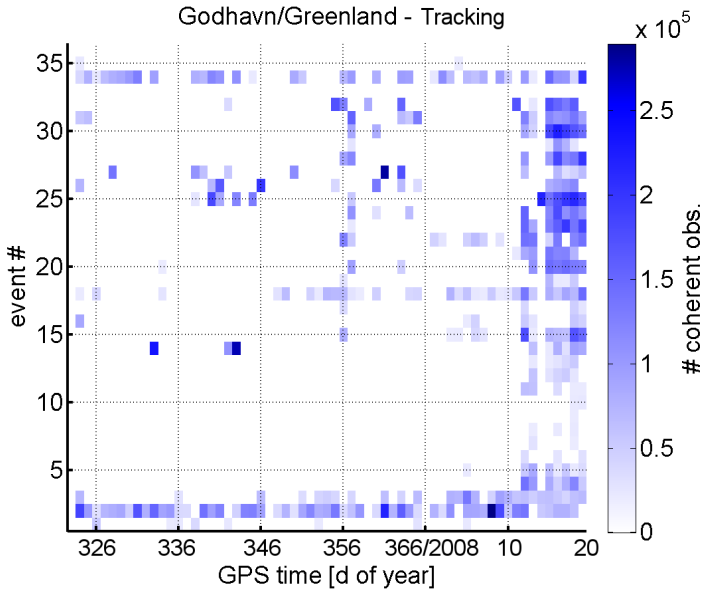

Figure 4.9: Number of coherent observations vs. day of the year 2009 and event number. The whole campaign is considered. Events are sorted by azimuth. The event number is assigned clockwise from East.

From the 56 events that are recorded 36 events are chosen that occur regularly and have

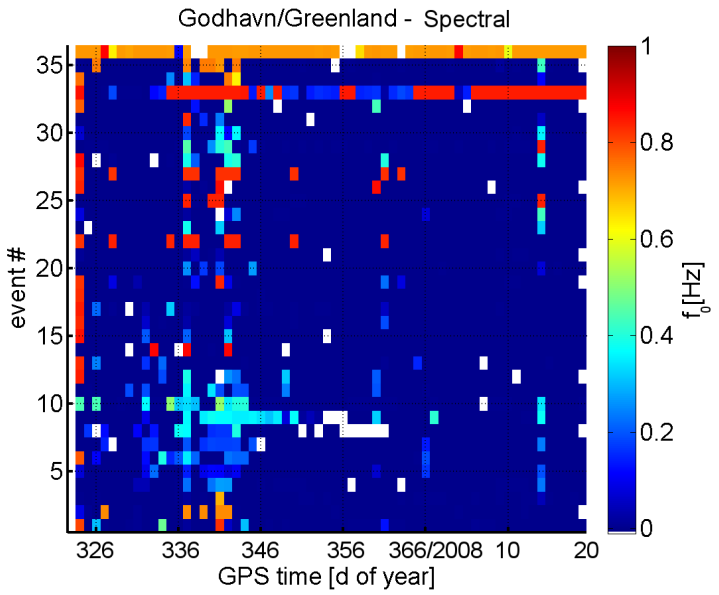

Figure 4.10: Absolute value of the residual frequency vs. day of the year and event number. The whole campaign is considered. Events are sorted by azimuth. The event number is assigned clockwise from East. Events that are running mostly over land were left out.

a track over the ocean. The number of coherent observations reaches a level, which is sufficient for the Tracking Retrieval, only during the last days. Those days coincide with the onset of sea-ice coverage (cf. Fig. 2.7). There is an important relation between phase coherence and early sea-ice coverage. The Tracking Retrieval for non-coherent observation during the period of the open ocean is not possible.
The application of the Spectral Retrieval is less restricted. Retrieving the stationary state, in the spectrum a residual peak at zero will remain, cf. Dirac-Delta-Distribution in eq.(3.20). The residual *Doppler* frequencies for all observed events are shown in Fig. 4.10.

The same selection of 36 events has been chosen. The stationary state was created for each event in form of the residual *Phasor* γ_0^J with J being the index of the reference height $H^J = G_{\mathrm{R}}$ given by the *Geoid* undulation at the receiver position. The dominating blue color in Fig. 4.10 shows the consistency of the Spectral Retrieval, i.e. stationary states using the specular model are retrieved throughout the campaign. A bias from the stationary state occurs sparsely, in particular in the beginning of Dec. (`DoY` [-30...-20]). In general the broader application of the Spectral Retrieval compared to the Tracking Retrieval is confirmed in the experiment.
Next to the temporal distribution, the plots in Fig. 4.9 and Fig. 4.10 provide the azimuthal distribution of specular events. Coherent observations occur almost continuously in event # 2 and 34, i.e. at the eastern and western edge. The number of coherent observations is permanently low for event # 5 to 17 in the south-east. The spectral peak of the most western event # 36 is permanently shifted and the peak of event # 33 is predominantly

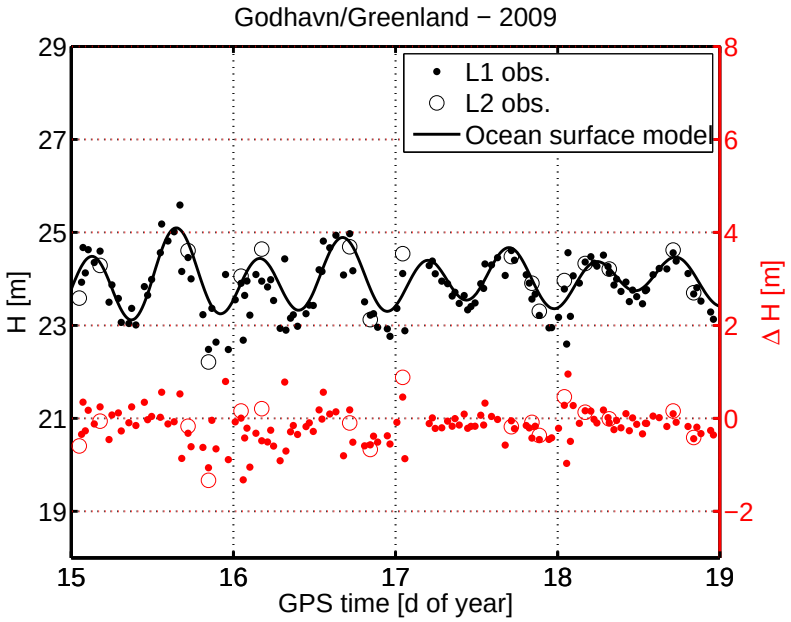

Figure 4.11: Estimated ellipsoidal heights derived from the tracked *Doppler* vs. GPS time in day of year 2009. Observations on L1 and L2 can be distinguished. For comparison an ocean surface model is added. The deviation of estimates from the model is shown in red.

shifted. The reason is probably a strong multipath that exceeds the the peak from the specular ocean reflection. A smaller shift in various events occurs in the beginning of Dec. It is clustered especially for the events # 5 to 17 in the south-east.
Undisturbed tracks, with a residual *Doppler* that is correlated with the surface height, were only retrieved during the last days of the campaign. Within this period 145(17) events on L1(L2) could be used for the Tracking Retrieval. The ellipsoidal height estimates for those events are shown in Fig. 4.11.

The variance of estimates is decreasing in the second half, when the sea-ice coverage reaches a compact state, cf. Fig. 2.7.
For the Spectral Retrieval a disturbance of the tracks is neglected. The correlation was analysed for 2157(450) events on L1(L2) throughout the campaign. Ellipsoidal heights are estimated as shown in Fig. 4.12.

For clarity, the estimations on L1 and L2 are plotted separately. The ocean surface model H_z is omitted in the plots but it was used to determine the height deviation $\Delta H = H - H_z$. The model is composed of a permanent *Geoid* undulation G and a tidal variation z and reads $H_z = G_\mathrm{R} + z(t)$, where G_R denotes the undulation at the receiver position. The *Geoid* undulation is obtained from EGM-96. The tidal variations are predicted by AODTM-5. For modelling the shallow water equations were solved for 8 harmonics (e.g. M2, S2, K1), more details are given in [Padman and Erofeeva, 2004].

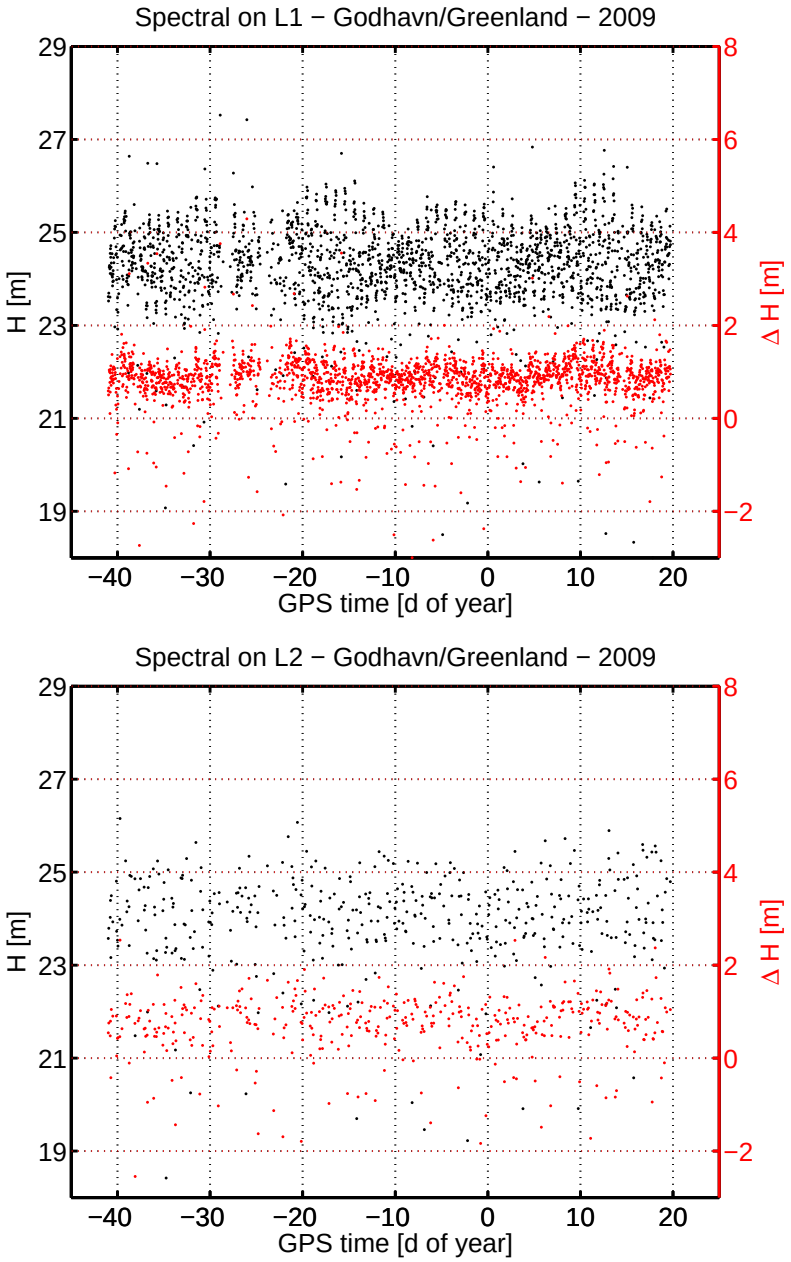

Figure 4.12: Estimated ellipsoidal heights derived from the *Doppler* spectrum vs. GPS time in day of year 2009. The difference of estimations and the ocean surface model are shown in red. The upper plot refers to observations on L1 and the lower plot to observations on L2.

4.2.2 Surface Model Deviation

A validation of the results using independent measurement is not possible, as no sea-level data (e.g. tide gauge data) was acquired at *Godhavn* during the campaign. The accuracy

	$\sigma(\Delta H)$ [cm]
best event `L1`	18
best event `L2`	26
worst event `L1`	177
worst event `L2`	155

Table 4.1: Standard deviation of events belonging to the same trace for a Spectral Retrieval on `L1` and `L2`.

of both retrievals can not be compared. The deviation from the ocean surface model will be considered instead. The ocean surface model has two contribution, temporal variations given by tides and a permanent offset given by the *Geoid*. The tidal variations predicted by `AODTM-5` have a small error of about 12cm. The permanent offset, however, given by the *Geoid* has a large error. The undulations obtained from `EGM-96` do not resolve spacial variations. If the undulation is interpolated, it varies about 40cm between the receiver position $G_{\mathrm{R}} = 24$m and the lowest value in the observed range at 5° of elevation, as we will see later in Fig. 4.37. So far a constant height in the *Geoid* model is assumed.
The deviation ΔH is obviously larger for the Spectral Retrieval than for the Tracking Retrieval. We have no explanation for that. For a better evaluation of Spectral Retrieval estimates, the standard deviation $\sigma(\Delta H)$ and the mean deviation $\mu(\Delta H)$ are determined for all estimates of an event that recurs on its trace every day. Values of σ for the best and worst agreement of events are given in Tab. 4.1.
The difference between `L1` and `L2` results is negligible. An azimuthal distribution of μ and σ emerges, when all events are considered. It varies largely between the traces, as shown in Fig. 4.13.

(a)

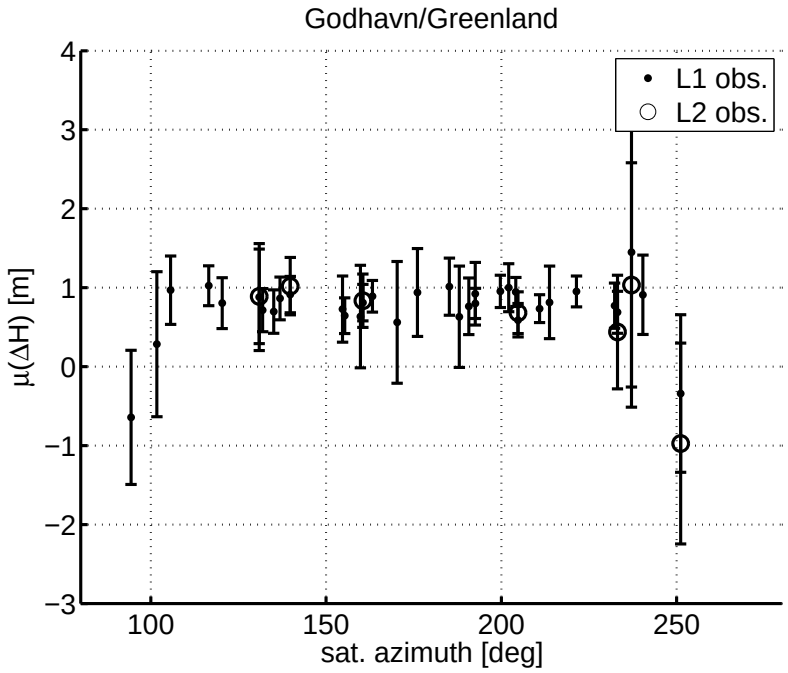

(b)

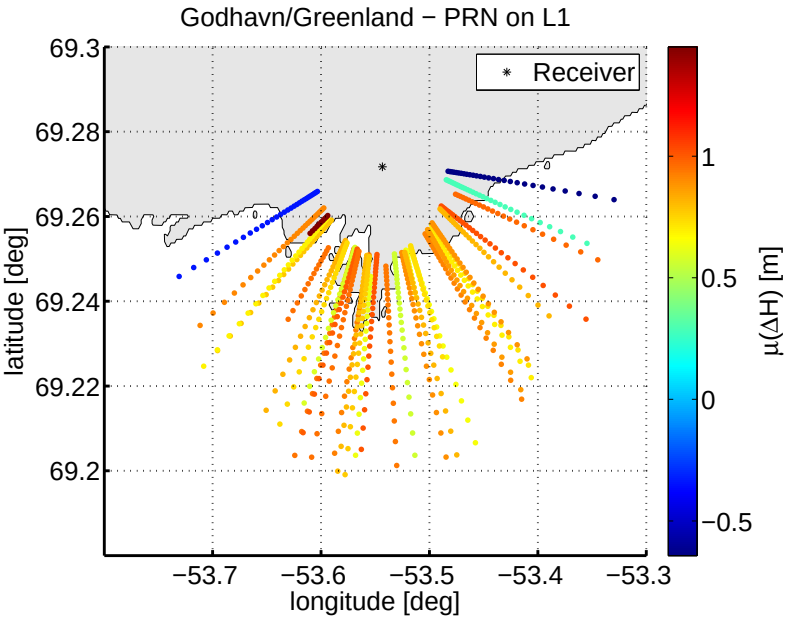

Figure 4.13: Mean deviation from the ocean surface model. The mean is calculated over the whole campaign for each trace separately. Only results from the Spectral Retrieval are considered. **(a)** the mean μ is plotted for `L1` and `L2` vs. the azimuth of the sat. trace. The error bars indicate the standard deviation. **(b)** the mean deviation is assigned to the reflection trace over *Disko Bay* for `L1` events.

In southern direction the mean deviation is about 1m. A decrease of μ occurs for events on

the edge in western and eastern direction. The difference indicates an influence of the *Geoid* undulation. In western and eastern direction, where the tracks are parallel to the coast, the undulation is predicted to be significantly smaller. The distribution of μ, however, is not a strict evidence for *Geoid* undulations, as other effects (e.g. the troposphere) might occur and standard deviation of those tracks on the edge is considerably increased.

4.2.3 Formal Precision

A significant deviation of the results and the ocean surface model was found. Before uncertainties are assessed, the effect of noise on the formal precision is determined. For specular reflection events a linear relation $f_0(H)$ holds between the residual *Doppler* and the surface height. The example of event PRN 17 in Fig. 3.27 showed, that the linear slope obtained for residual observations f_0 is within the range of slopes predicted for the model $f(h)$, see Fig. 3.15. The linear relation, that holds for the *Doppler* model $f(h)$ and the residual *Doppler* $f_0(H)$ has already been discussed. The slope of the linear relation defines the altimetric sensitivity of the retrieval in the following way

$$\frac{\delta H}{\delta f_0} = \left| \frac{df_0}{dH} \right|^{-1}, \tag{4.4}$$

where the absolute value of the slope is used to treat rising and setting reflection events, that have opposite sign, equally. According to the sensitivity in eq.(4.4) the formal altimetric precision is written,

$$\delta H = \left| \frac{df_0}{dH} \right|^{-1} \delta f_0, \tag{4.5}$$

where δf_0 is the uncertainty of the residual *Doppler* that is dependent on the retrieval. For the Tracking Retrieval the uncertainty is derived from the standard deviation $\sigma(\Delta\phi_0)$

$$\begin{aligned} \delta f_0 &= \left| \frac{\partial f_0}{\partial \Delta\phi_0} \right| \sigma(\Delta\phi_0) \\ &= \frac{1}{n\,T_c}\,\sigma(\Delta\phi_0), \end{aligned} \tag{4.6}$$

where the relation between f_0 and the phase difference $\Delta\phi_0$ in eq.(3.18) is used. It is worth noting that the uncertainty decreases with an increasing number of continuous samples n and an increasing coherent integration time T_c.
For the Spectral Retrieval the uncertainty is set by the spectral resolution, which is given according to a discrete Fourier Transformation by,

$$\delta f_0 = \frac{1}{T},$$

where T denotes the time of the considered event. The number of continuous samples has no influence in this case. The precision of the residual *Doppler* dominates the altimetric

	L-band	$\delta H/\delta f_0$ [m/Hz]	δf_0 [E^{-3}Hz]	δH [E^{-2}m]
Tracking	L1	780	0.03	3
	L2	996	0.04	4
Spectrum	L1	777	0.68	53
	L2	997	0.68	68

Table 4.2: Comparison for event PRN 17 - 2009/01/18 17:04:55. Different retrievals and carrier frequencies are considered.

precision. A comparison for both retrievals based on the example event is given in Tab. 4.2.
For both retrievals the altimetric sensitivity $\delta H/\delta f_0$ is similar. There is a carrier dependency, L1 observations are more sensitive to altimetric changes than L2 observations. A large difference in δf_0 occurs for both retrievals. The coherence filter and the coherent integration used for the Tracking Retrieval reduce the noise and lead to a high formal precision in the centimeter range. The precision then is strongly dependent on the considered event. For the Spectral Retrieval the formal precision is in the decimeter range. The advantage, however, lies in its general validity. Furthermore uncertainties in the decimeter range remain even for the Tracking Retrieval as it is indicated by the comparison to the surface model.
For the Spectral Retrieval the slope of the linear correlation is used to determine the altimetric sensitivity throughout the campaign, see Fig. 4.14.

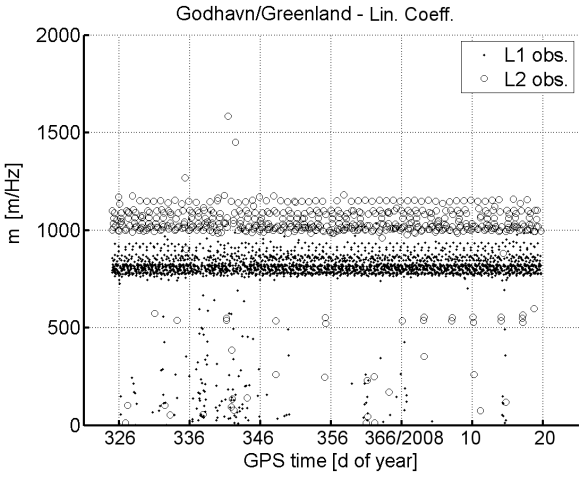

Figure 4.14: Altimetric sensitivity vs. GPS time. Specular events are located in a constant range between [700...1200]m/Hz, outliers refer to non-specular events. The specular events forms classes of L1 and L2 observations.

Most events cluster at a constant sensitivities for L1 and L2 respectively. A few outliers occur in the beginning of Dec. (DoY [-30...-20]), they indicate a failure of the model that assumes specular reflections. The applicability on the Spectral Retrieval is confirmed

throughout the campaign.

4.2.4 Tide Spectrum

The robust height estimation with the Spectral Retrieval results in an altimetric time series, that extends over more than 60 days and 2157(450) events on L1(L2). A further investigation of tidal components is possible. The number of considered events per day is about 36 for L1 and 7.5 for L2 observations. The resolution of semidiurnal tides requires a sampling of at least 4 events per day according to the Nyquist Theorem. That means theoretically semidiurnal tide components can be observed for L1 and even for the much smaller amount of events on L2. The time series $H(t)$, see Fig. 4.12 above, are used to obtain a tide spectrum. The following steps are made. The mean height $\overline{H(t)}$ is subtracted from the time series. The difference $H(t) - \overline{H(t)}$ is interpolated on an equidistant time axis with a spacing $\Delta t = 15$min, that is close to the spacing of the records [15...30]min. The spectrum is calculated using a Fast Fourier Transform and the results are shown in Fig. 4.15.

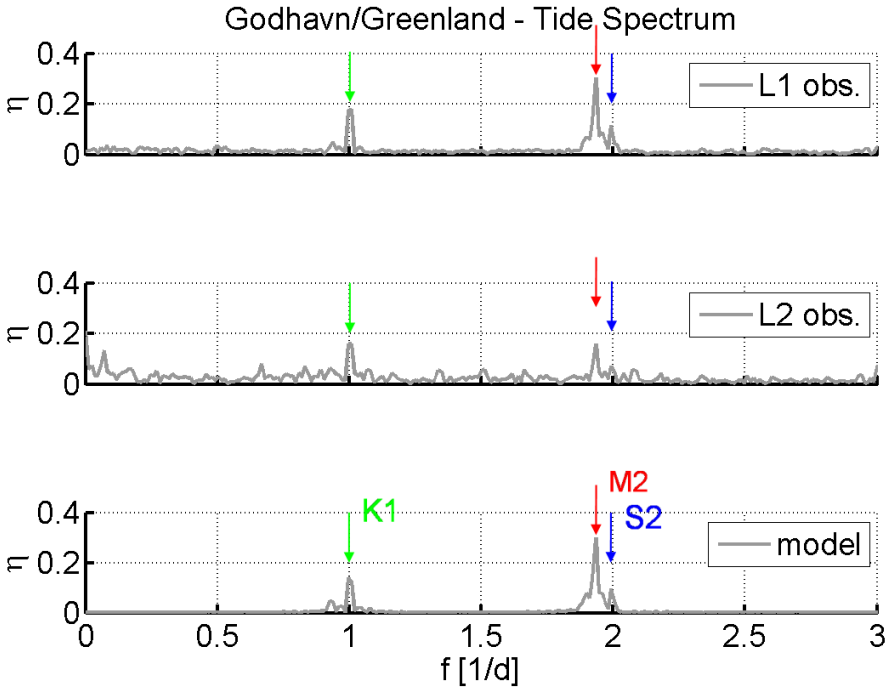

Figure 4.15: Tide spectrum vs. tidal frequency for time series on L1 and L2 (cf. Fig. 4.12). For comparison a spectrum based on a modelled time series using the AODTM-5 tide model is added. Different tidal components are marked in different colours.

The semidiurnal components S2 and M2 are identified in the L1 and L2 observations. The diurnal component K1 is also observed. Aliasing peaks occur at higher frequencies.

4.3 Uncertainties

The comparison of the altimetric results with an ocean surface model revealed a bias, which is larger than the formal precision would explain. Different error sources will be considered in the following. Simulations estimate i.a. the influence of tropospheric and ionospheric refraction, the influence of receiver position accuracy and transmitter orbit precision and the influence due to *Geoid* undulations of the ocean surface. Those uncertainties belong either to parameters that are already included in the model or to further uncertainties that were not yet considered. According to both groups a slightly different procedure is used in the simulations.

Model Uncertainty

Different aspects that affect the altimetric results have been included as parameters in the model. There are remaining uncertainties that contributes to the altimetric error. The aspects comprise, i.a. the tropospheric refraction, the receiver position, the transmitter orbit and the ellipsoidal curvature. In the altimetric model the state vector consists of states with different surface heights. Other parameters, like the refractivity, are fixed. The uncertainty in any of the model parameters can be denoted Δ. Represented by the interferometric path, the state vector of the bias altimetric model reads then,

$$L^j_{\mathrm{alt}}(\Delta) \;=\; L^j_r(\Delta) - L_d(\Delta), \tag{4.7}$$

where the index j refers to states with different surface heights H^j and Δ is a measure for the uncertainty of another parameter in the model. The path lengths are calculated with the ray tracing integrals, cf. eq.(3.8), that generally will depend on Δ of course,

$$\begin{aligned} L^j_r(\Delta) &= \int\limits_{\Lambda^J_r(\Delta)} N(\Delta)dl, \\ L_d(\Delta) &= \int\limits_{\Lambda_d(\Delta)} N(\Delta)dl, \end{aligned} \tag{4.8}$$

where Λ_r, Λ_d denote the ray traces, dl is the infinitesimal length along the trace and N is the refractivity. To obtain residuals, a reference event is simulated using the unbiased state of the model L^J_{alt}, where the index J is fix at the reference height $H^J = G_{\mathrm{R}}$ set by the *Geoid* undulation at the receiver position. The absence of ambiguities in the reference path allows us to retrieve unambiguous path residuals by the difference,

$$L^j_0(\Delta) \;=\; L^J_{\mathrm{alt}} - L^j_{\mathrm{alt}}(\Delta) \tag{4.9}$$

a usage of *Phasor* notation is not necessary. Due to the uncertainty Δ, a path bias will remain even if the reference height $H^j = H^J$ is assumed. The bias is given by,

$$\delta L \quad = \quad -L_0^{j=J}(\Delta). \tag{4.10}$$

The negative sign is just a convention.
The mean phase rate can be derived without restrictions due to coherence. The residual *Doppler* is determined in a Tracking Retrieval,

$$f_0(\Delta, H^j) \quad = \quad -\frac{2\pi}{\lambda_{\mathrm{L}}} \overline{\frac{dL_0^j}{dt}}(\Delta), \tag{4.11}$$

where the wavelength of the L-band carrier is denoted λ_{L}. The time average, here indicated by the bar, covers intervals of 1min in the event. Therefore a temporal resolution within the simulated event is achieved, whereas for real observations the integration covers a whole event (about 25min) and allows no detailed resolution. The height bias for each interval is then defined,

$$\delta H \quad = \quad H(f_0 = 0, \Delta) - H^J,$$

where $H(f_0, \Delta)$ is the fit function of the correlation between H^j and f_0^j.
Next to the height bias δH, that is normal to the surface, a bias δS of the specular point S tangent to the surface can be derived. The distance S refers to the arc length between S and the receiver position R projected on the *Osculation* sphere,

$$S \quad = \quad \theta_{\mathrm{RS}}\, R_c, \tag{4.12}$$

where θ_{RS} denotes the angular distance between R and S in the CC frame and R_c is the radius of the osculating sphere. Both parameters θ_{RS}, R_c result from ray tracing calculations. Provided that $S(\Delta)$ refers to the biased model and S_{ref} is the arc length of the simulated reference, the tangent arc bias is defined,

$$\delta S \quad = \quad S(\Delta) - S_{\mathrm{ref}}. \tag{4.13}$$

The bias δL, δH and δS will be derived for uncertainties in different parameters.

4.3.1 Tropospheric Refraction

An important bias emerges by mismodelling of refraction. The non-dispersive refractivity N^o, dominant in the troposphere is the first source we consider. To quantify the expected uncertainty, we compare the tropospheric delay given by the model with slant delays T_{slant} that were estimated as described in [Bender et al., 2009]. The modelled delay is calculated as follow,

$$T \;=\; L - L(N=0)$$

where L is the interferometric path calculated with the predicted refractivity N^o and $L(N^o = 0)$ is the one that neglects a refractivity N^o. The slant delays $T_{\text{slant}}(E)$ were estimated in a specific range of elevations. The modelled delay uses the same range. The absolute value of the deviation between both delays predicts the tropospheric error that is mapped to *Zenith* direction,

$$\delta T_{\text{zenith}} \;=\; |T_{\text{slant}} - T| \sin E$$

where the inverse of the simple mapping function $T(E) = T_{\text{zenith}} \sin^{-1} E$ is used, that approximates the mapping in the ray tracing. The mapping to *Zenith* is necessary to compare the tropospheric error δT for events at different elevations. Fig. 4.16(a) shows the results of the comparison for 35 events that were processed with the `EPOS` software day by day in Jan. 2009. The maximum error for the *Zenith* direction is about 2cm. That is about 1% of the total delay in *Zenith* direction (`TZD`), $T_{\text{zenith}} \approx 2$m. The modelled `TZD` for the period in Jan. 2009 is shown in Fig. 4.16(b).
The uncertainty of the delay in *Zenith* direction δT_{zenith} follows from the relative uncertainty of refractivity $\Delta = \delta N^o / N^o$. The corresponding *Zenith* path integration it is written,

$$\begin{aligned} \delta T_{\text{zenith}} &= \int_{\Lambda_{\text{zenith}}} \delta N^o dl \\ &= \Delta \int_{\Lambda_{\text{zenith}}} N^o dl \\ &= \Delta\, T_{\text{zenith}} \end{aligned} \tag{4.14}$$

where the bias Δ is separated from the linear integration. Now we can define the refractivity bias Δ in the range [-1, -0.5, 0, 0.5, 1]%. Using eq.(4.10),(4.12),(4.13) biases δL, δH, and δS are determined, see Fig. 4.17, 4.18 and 4.19. There is a symmetric bias for the underestimated ($\Delta < 0$) and the overestimated ($\Delta > 0$) troposphere. The bias in all observables δL, δH and δS increases with decreasing elevations. There is an obvious relation between the slope of δL and the run of δH in Fig. 4.17 and 4.18. The path can be used to derive the *Doppler*, cf. eq.(4.11). Accordingly the bias of the *Doppler* is written

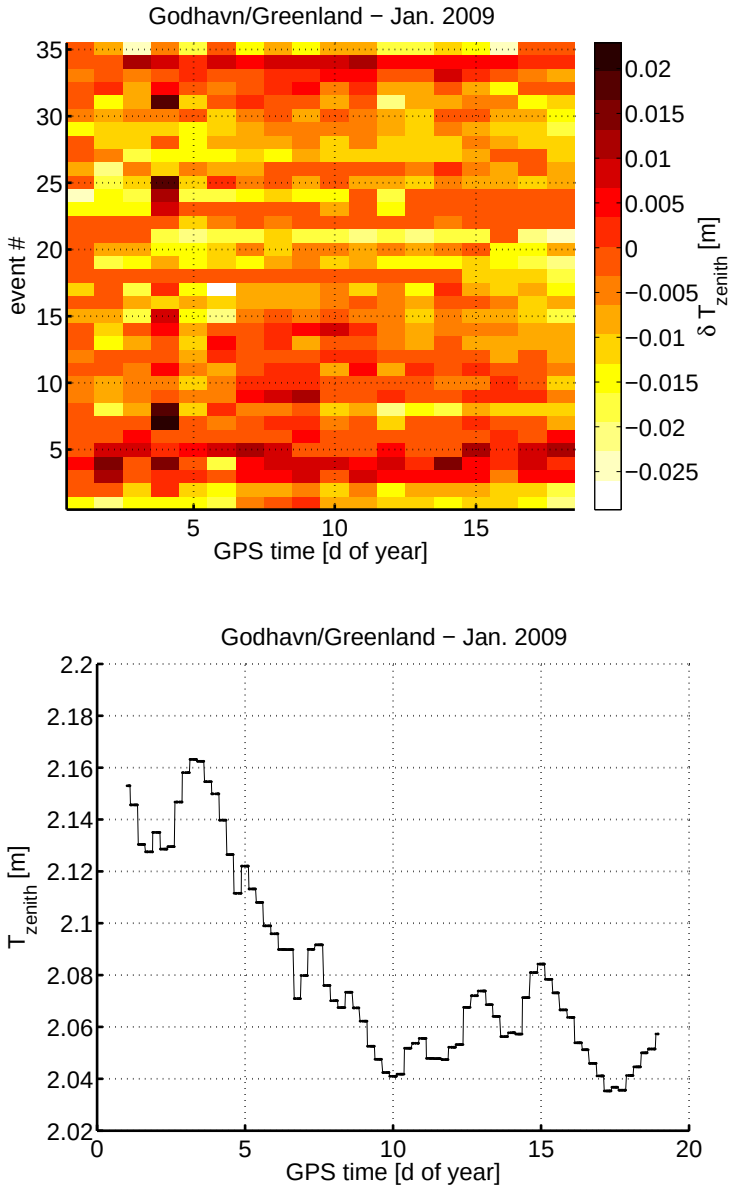

Figure 4.16: Tropospheric delay at *Godhavn* in Jan. 2009. **(a)** The bias in *Zenith* direction vs. GPS time and event number. Events are sorted by azimuth. The event number is assigned clockwise from East. **(b)** The TZD vs. GPS time obtained from ECMWF data.

$$\begin{aligned} \delta f &= -\frac{1}{\lambda_L}\frac{d\delta L}{dt} \\ &= -\frac{1}{\lambda_L}\frac{\partial \delta L}{\partial E}\frac{\partial E}{\partial t}, \end{aligned}$$

for the second line it is used that temporal changes in L are introduced by the time dependence of the elevation E. The elevation rate $\partial E/\partial t$ is almost constant in the range of observed elevations [5...15]°. Using the linearity between f and H, that has been shown already, we obtain the following relation for the elevation dependence of the height bias,

$$\delta H(E) \approx \text{const.}\,\frac{\partial \delta L}{\partial E}. \tag{4.15}$$

It explains the run in Fig. 4.18. This relation is more general and holds not only for a tropospheric bias. The maximum bias relevant for our experiment is reached at an elevation of 5°, where $|\delta H| \approx 20$cm for $|\Delta| = 1\%$. The arc bias δS is about several meters for the observed elevation range. The tangent precision is not of major concern, as it is assumed that the surface is constant on a much larger footprint.

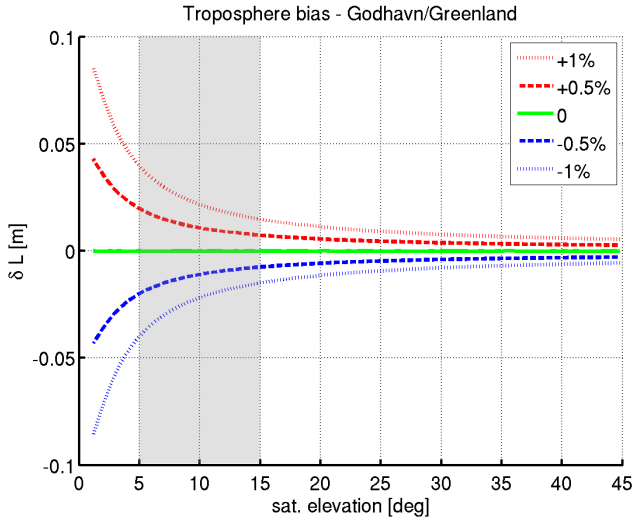

Figure 4.17: Simulations of tropospheric bias in the phase path vs. elevation of the satellite. The elevation range of observed reflections is shaded in grey.

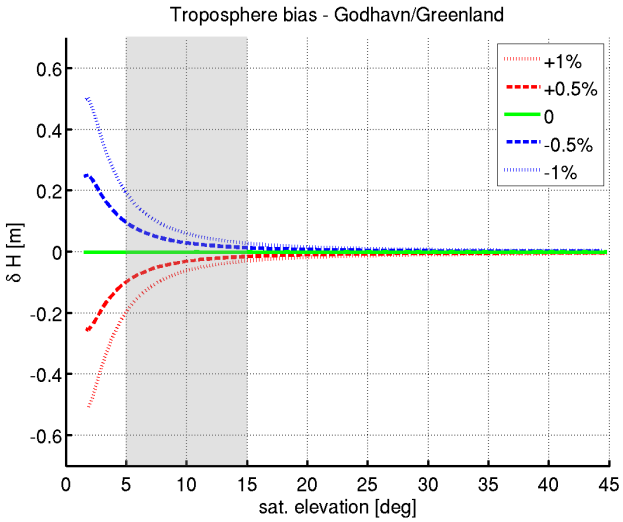

Figure 4.18: Simulations of tropospheric bias in the height vs. elevation of the satellite. The elevation range of observed reflections is shaded in grey.

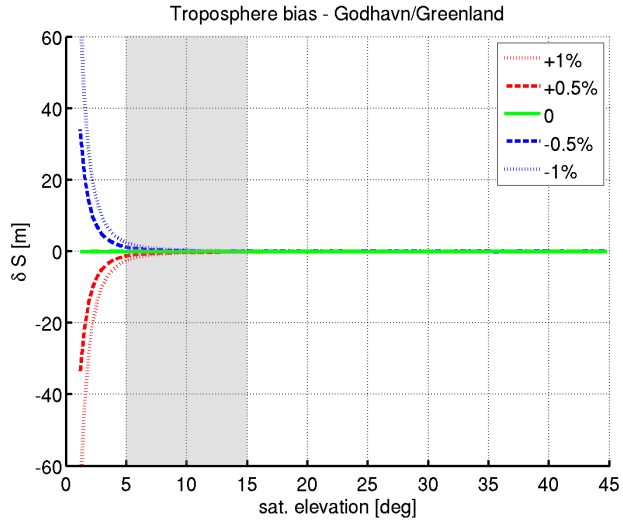

Figure 4.19: Simulations of tropospheric bias in the tangent arc vs. elevation of the satellite. The elevation range of observed reflections is shaded in grey.

4.3.2 Receiver Position

The analogy to differential positioning suggests that the accuracy of the receiver position is a crucial limit for the accuracy of the reflection ranging. Unfortunately there is no independent measurement of the receiver position, so the accuracy can not be determined. Effects that contribute to the positioning error can be found in literature. The effect of solid Earth tides on Greenland reaches up to 30cm [Xu and Knudsen, 2000]. For *Godhavn* ocean loading models predict a periodic bias of up to 2cm [Ramatschi, 1998]. Both effects, solid Earth tides and ocean loading, were modelled in the `EPOS` processing of the direct signal and the residual error for the receiver position will be below 30cm. To evaluate the altimetric error, the reference event is biased with an offset Δ in the height component of the receiver position. The altimetric model still uses the unbiased position. The corresponding results for δL, δH and δS are shown in Fig. 4.20, 4.21 and 4.22. There is obviously a prolongation of the signal path due to a positive bias Δ and a shortening due to a negative bias. In the present experiment the path bias induced by the offset Δ can be described in a planar approximation

$$\begin{aligned} \delta L &= L^J_{\mathrm{alt}}(\Delta) - L^J_{\mathrm{alt}} \\ &\approx 2 \sin E \, \Delta. \end{aligned}$$

Then the bias in the receiver height translates to a bias in the surface height with the same magnitude. The elevation dependency is negligible and the height bias is related to the path bias, cf. eq.(4.15). An overestimation in the receiver height yields an overestimated surface height, whereas an underestimation yields an underestimated surface height.

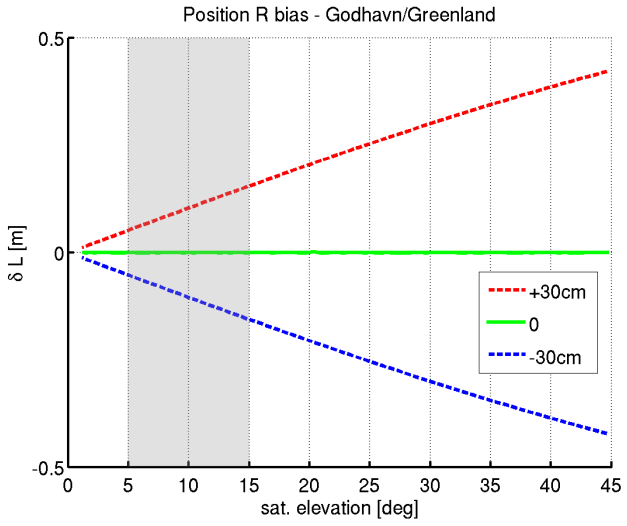

Figure 4.20: Simulations of a receiver position bias in the phase path vs. elevation of the satellite. The elevation range of observed reflections is shaded in grey.

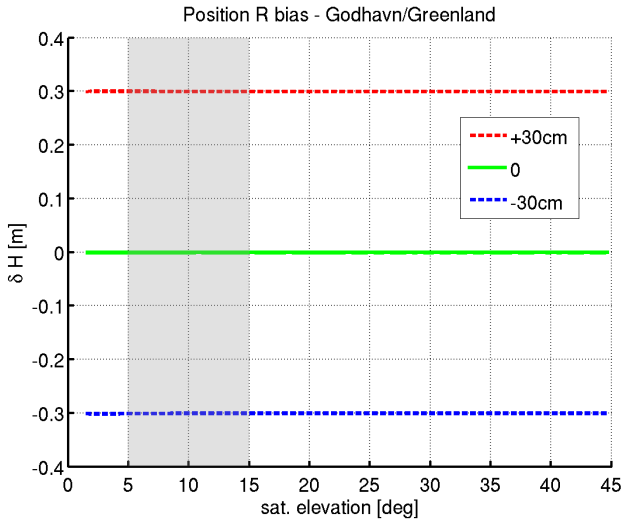

Figure 4.21: Simulations of a receiver position bias in the height vs. elevation of the satellite. The elevation range of observed reflections is shaded in grey.

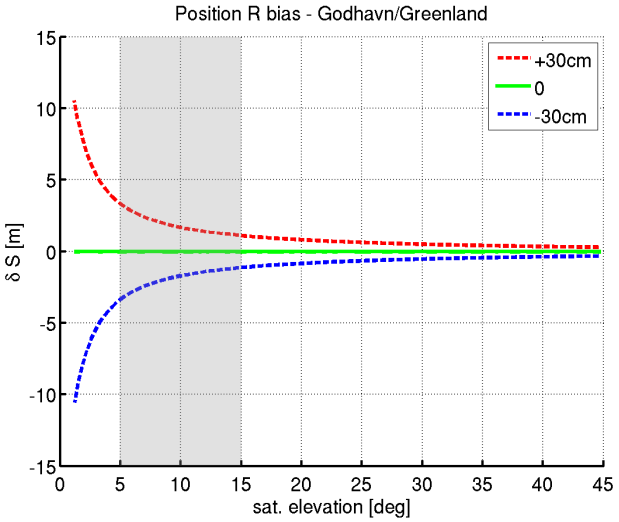

Figure 4.22: Simulations of a receiver position bias in the tangent arc vs. elevation of the satellite. The elevation range of observed reflections is shaded in grey.

4.3.3 Transmitter Orbits

The differential character of interferometric observations decrease the bias that arise from the uncertainty of the transmitter orbit. For the ray tracing model broadcast orbits determined by orbital elements are used. They allow a fast computation but are non-validated predictions.
Precise orbits in contrast are determined using validation measurements, e.g. Satellite Laser Ranging, in post-processing by IGS. It is an important question whether the precision of reflection ranging will significantly improve if precise orbits are used instead of broadcast orbits. To answer this question a reflection event is simulated using precise orbits. The altimetric model, however, still uses broadcast orbits. The bias in this case emerges due to the distance between precise and broadcast orbits, that is written,

$$\Delta \quad = \quad |\vec{r}_{\mathrm{prc}} - \vec{r}_{\mathrm{brc}}| \,,$$

where $|\cdot|$ denotes the Euclidean length of the vector. The transmitter position in ITRF, using precise or broadcast orbits, are denoted $\vec{r}_{\mathrm{prc}}$ and $\vec{r}_{\mathrm{brc}}$, respectively. The distance Δ for the example event PRN 17 is shown in Fig. 4.23.

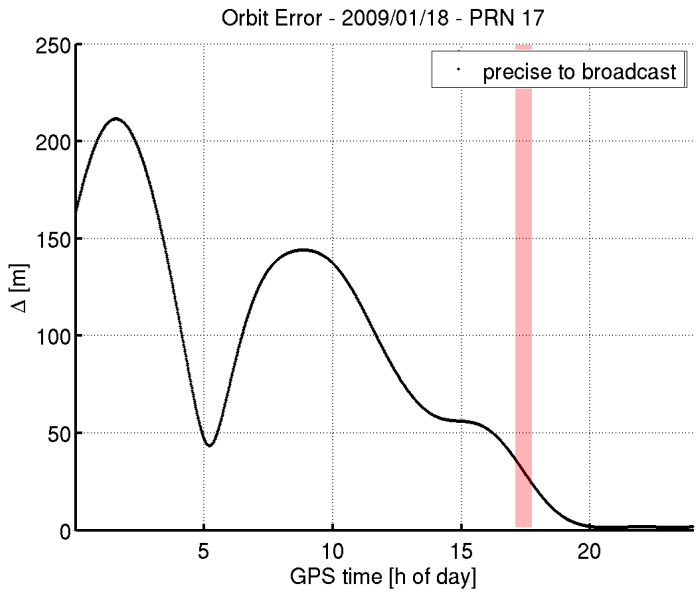

Figure 4.23: Distance between precise and broadcast orbit vs. GPS time. It is an estimate of the orbit error. The time interval of event PRN 17 - 2009/01/18 17:04:55 is shaded.

The distance varies over this specific day reaching about 200m at most. During the considered event it is rather small ≈30m. The actual distance will be of minor importance due to the differential character of the observation. But the rate error given by $d\Delta/dt$ is of interest. Considering the plot in Fig. 4.23, the maximum rate that occurs on 2009/01/18 is 1m per minute. Compared to the satellite velocity ≈4km per second (cf. [Xu, 2007] Sec. 5.5) this error is small. The model in the simulation switches between broadcast and

precise orbits. The reference is the broadcast orbit. The corresponding results for δL, δH and δS are shown in Fig. 4.24, 4.25 and 4.26. The bias that arises from comparison of broadcast and precise orbits is negligible for all observables. In the observed range of elevation the height bias is far below the significant centimeter range.

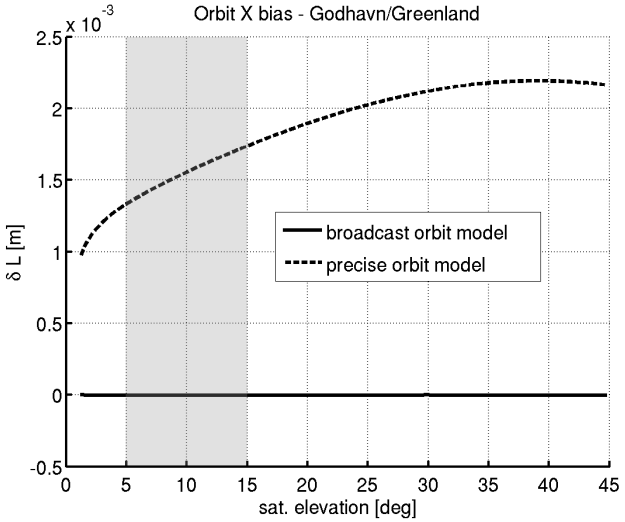

Figure 4.24: Simulations of an orbit bias in the phase path vs. elevation of the satellite. The elevation range of observed reflections is shaded in grey.

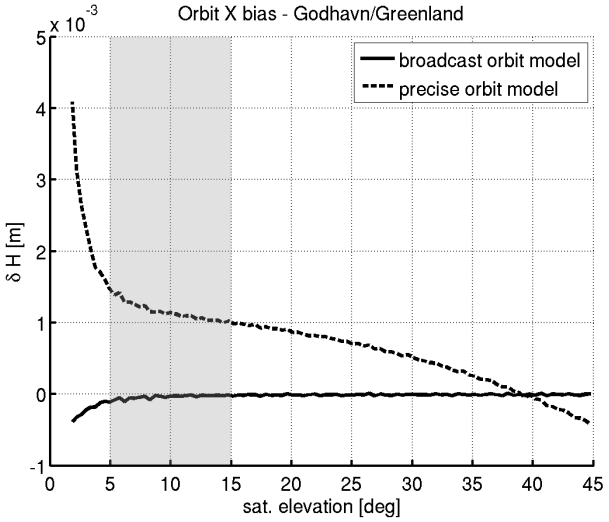

Figure 4.25: Simulations of an orbit bias in the height vs. elevation of the satellite. The elevation range of observed reflections is shaded in grey.

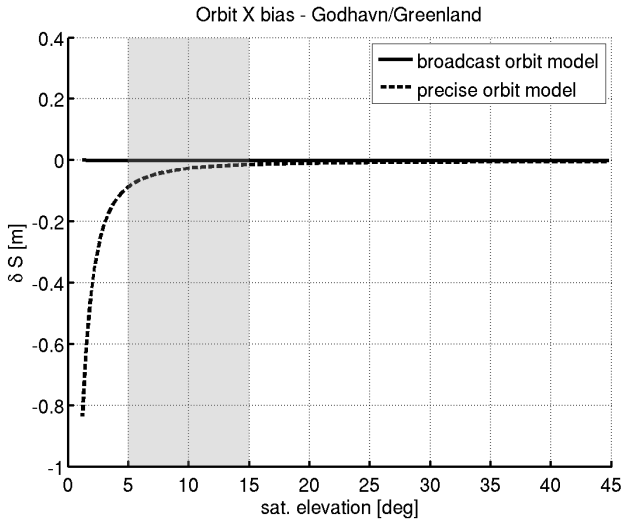

Figure 4.26: Simulations of an orbit bias in the tangent arc vs. elevation of the satellite. The elevation range of observed reflections is shaded in grey.

4.3.4 Ellipsoidal Curvature

The curvature of the ellipsoid is already considered in the model. A spherical surface is assumed. The best fit of ellipsoid and sphere is achieved by *Osculation*, i.e. the spherical surface agrees with the ellipsoidal curvature in vicinity of a base point B, see Fig. 4.27. The location of the base point influences the altimetric results. Two different locations B will be compared, either the *Osculation* is based at the receiver location R or it is based at the specular point, see Fig. 4.27.

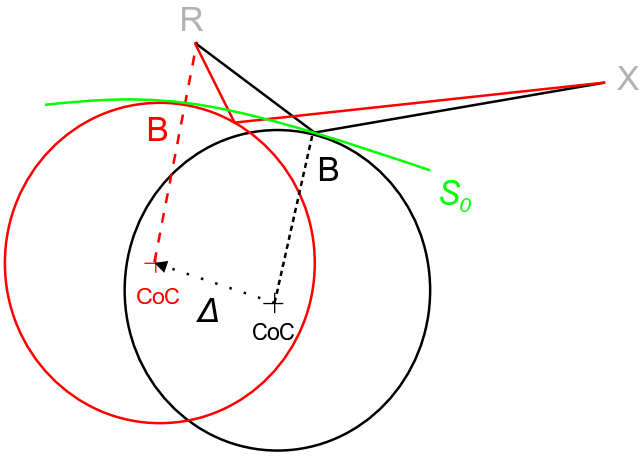

Figure 4.27: Transect of two spherical surfaces in the reflection plane. The spheres osculate the ellipsoid in different base points B. The base point at the receiver is known apriori, the base point at the specular reflection requires an apriori approximation. For simplicity *Geoid* undulations were neglected, i.e. the specular point coincides with the according base point.

The receiver based *Osculation* is easy to achieve, as the location R is known apriori. Changes in the curvature along the arc distance S to the specular point are neglected then. The specular based *Osculation* is more complicated, it requires an apriori location A of the specular point for each epoch (cf. Sec. 3.1.2). In the present experiment the arc distance S is rather small, it is in the range $[2.5 \ldots 7.5]$km for a typical event. However, a specular based *Osculation* was performed for height estimations in the *Godhavn* experiment. In the following the bias is estimated, that emerges, if the model was simplified and a receiver based *Osculation* would be used. Accordingly, the uncertainty, introduced in the model, is the distance Δ of both spherical `CC` frames with the origin in different `CoC`, see Fig. 4.27. The ongoing procedure is the same as before and the bias δL, δH and δS are shown in Fig. 4.28, 4.29 and 4.30.

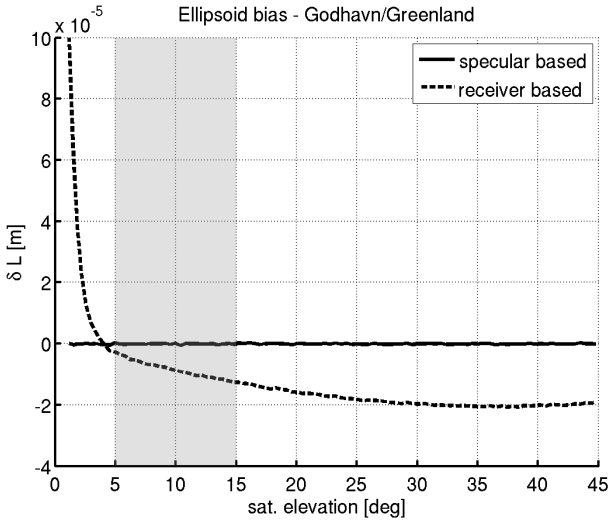

Figure 4.28: Simulations of ellipsoidal bias in the phase path vs. elevation of the satellite. The elevation range of observed reflections is shaded in grey.

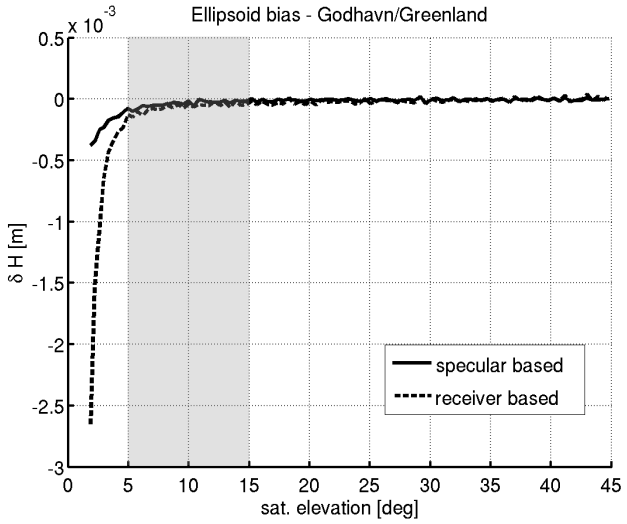

Figure 4.29: Simulations of ellipsoidal bias in the height vs. elevation of the satellite. The elevation range of observed reflections is shaded in grey. For the specular based case there should be no bias. The inconsistency is related to a negligible imprecision of the model.

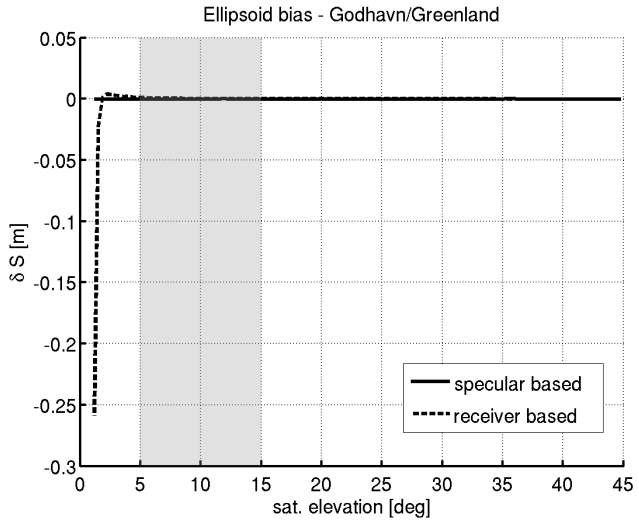

Figure 4.30: Simulations of ellipsoidal bias in the tangent arc vs. elevation of the satellite. The elevation range of observed reflections is shaded in grey.

The estimated bias due to simplification is negligible in such a ground-based experiment. In the observed range of elevation angles the height bias is far below a significant centimeter range. The bias might be significant for a spaceborne reflection event, when the distance S reaches hundreds of kilometers.

Further Uncertainties

Further aspects were not modelled for height estimation but potentially affect the altimetric results. They comprise, i.a. ionospheric refraction and *Geoid* undulations. In contrast to uncertainties in the model, considered above, the unmodelled aspects require a small change in bias estimation. The parameter Δ is now introduced in the simulated reference $L^J_{\text{alt}}(\Delta)$ and not in the model. This change is important to predict the sign of the bias. The path lengths $L_r(\Delta, H^J)$ and $L_d(\Delta)$ that contribute to the reference event formally agree with eq.(4.8). The state vector of the altimetric model remains unbiased $L^j_{\text{alt}} = L_r(H^j) - L_d$. Due to the absence of ambiguities in the reference event, the residual path is retrieved unambiguously, $L^j_0 = L^J_{\text{alt}}(\Delta) - L^j_{\text{alt}}$ in correspondence to eq.(4.9). The determination of biases δL, δH and δS are completely analog. Those biases will be considered for ionospheric refraction and *Geoid* undulations in the following.

4.3.5 Ionospheric Refraction

We assume that the non-dispersive part of the refractivity N^o is unbiased. The refractivity bias Δ is now made up by the dispersive refraction that was neglected so far. Assuming an *F-layer* the electron density distribution η is computed according to eq.(3.5). The corresponding dispersive refractivity is written

$$N^{\mathtt{F}} = -\frac{40.3}{f_{\mathtt{L}}^2}\,\eta^{\mathtt{F}},$$

where $f_{\mathtt{L}}$ denotes the dependence on the *L-band* frequency. The density distribution is not observed but observations of the integrated electron density given by the total electron content (TEC) are available,

$$\mathtt{TEC} = \int_{\Lambda} \eta dl,$$

where Λ denotes the path of integration, i.e. the trace of the direct signal. The TEC can be used to estimate the peak density $\hat{\eta}$ leaving the other parameters of the layer in eq.(3.5) unchanged. We introduce Δ as a scaling factor of the peak $\hat{\eta} = \Delta\,\eta_0$. If the other layer parameters are constant, η_0 can be chosen to obtain a vertical TEC of 1TEC-unit for $\Delta = 1$. The vertical TEC is then formally written, as follows

$$\begin{aligned} \text{vTEC} &= \int_{\Lambda_{\text{zenith}}} \eta\, dl \\ &= \Delta \int_{\Lambda_{\text{zenith}}} \eta_0\, e^{f(H,H_0,D)} \end{aligned}$$

The integration is done along a path Λ_{zenith} in zenith direction. Observed values of the vertical TEC in Jan. 2009 are shown in Fig. 4.31.

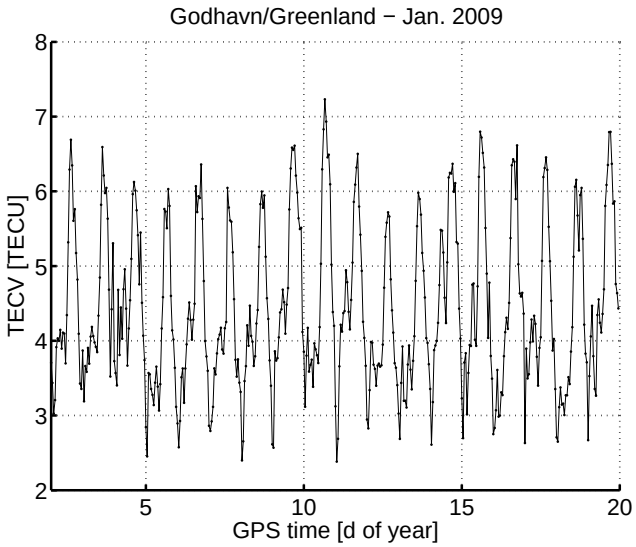

Figure 4.31: Vertical TEC vs. day of year in Jan. 2009. There is a diurnal periodicity induced by the sun. Maxima occur at local noon at about 14h GPS time.

The TEC observations are used to confine Δ in the following simulations. A moderate vertical TEC lies at about 5TEC-units. Over the whole campaign a maximum of 15TEC-units was not exceeded and serves as an upper limit for the simulations. Results with Δ in the interval [0, 5, 15] are shown in Fig. 4.32, 4.33 and 4.34 for the different observables.

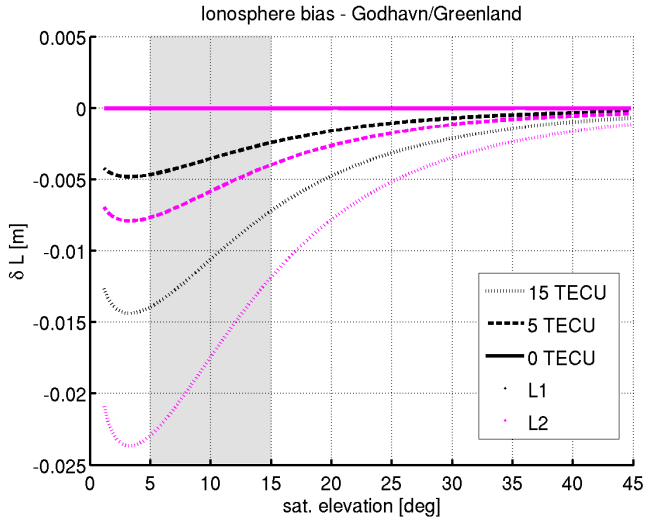

Figure 4.32: Simulations of ionospheric bias in the phase path vs. elevation of the satellite. The elevation range of observed reflections is shaded in grey.

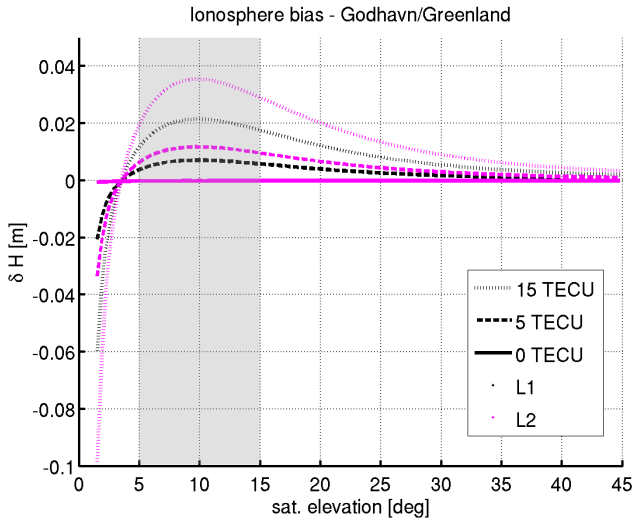

Figure 4.33: Simulations of ionospheric bias in the height vs. elevation of the satellite. The elevation range of observed reflections is shaded in grey.

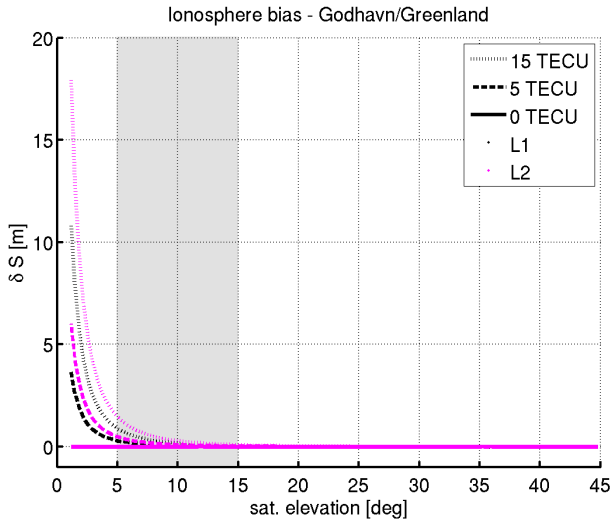

Figure 4.34: Simulations of ionospheric bias in the tangent arc vs. elevation of the satellite. The elevation range of observed reflections is shaded in grey.

Biases due to ionospheric refraction are dispersive, they are larger for `L2` than for `L1`. The magnitude of δL changes with the elevation and increases linearly with an increasing vertical `TEC`. An extremum of δL occur at about 3° of elevation. The decrease of the magnitude at smaller elevations could be explained by the convergence of direct and reflected rays, which reduces the ionospheric influence. For the relevant elevation range $[5 \ldots 15]°$ a positive height bias is predicted. In agreement with eq.(4.15) the bias δH reaches a maximum of about 2cm for `L1` and about 3cm for `L2`. The height bias simulated for a constant iono-

spheric *F-layer* is one order of magnitude smaller than the tropospheric bias we observed before. For the arc bias δS it is worth noting, that the constant *F-layer* will increase the distance S. The shift of a few meters is not of interest for our estimation.

4.3.6 Geoid Undulations

To quantify the bias in the presented height estimation that emerges from *Geoid* undulations requires a slightly different approach. In contrast to other parameters the *Geoid* influences directly the surface height, that means the reference event with a constant height as it was considered for the other parameters is no longer useful. The altimetric method assumes a constant surface height during the event, the *Geoid*, however, describes a surface undulation within the footprint of the event (about 5km long), see Fig. 4.37. According to the `EGM-96` model the surface height decreases by $\Delta \approx 30$cm from the nearest end of the footprint (at $E \approx 15$deg) to the farthest end (at $E \approx 5$deg). In this short range the model provides only interpolated values. The real gradient close to the steep coast at *Godhavn* could be even larger.
The interferometric path of a simulated event is calculated by ray tracing for a specular point on the *Geoid* reference, $L_{\mathrm{ref}}(G) = L_r(G) - L_d$. Using the unbiased model L^j_{alt} the path in the pseudo-stationary states $L_0(G)^j$ is determined and the biases δL and δS are derived, see Fig. 4.35 and 4.36. The height $H(f_0 = 0, G)$ is estimated using the Tracking Retrieval. A comparison to the *Geoid* model G and to the constant reference height H^J is shown in Fig. 4.37. An overestimation of up to 30cm for the height in the observed range results from the difference $H(f_0 = 0, G) - G$.

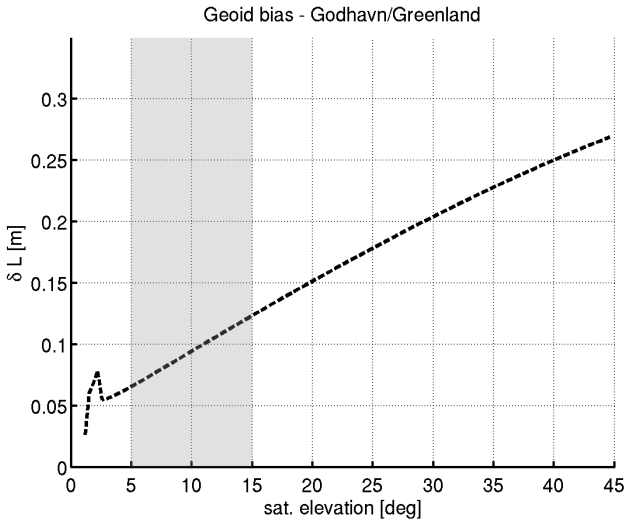

Figure 4.35: Simulations of topographic bias in the phase path vs. elevation of the satellite. The elevation range of observed reflections is shaded in grey.

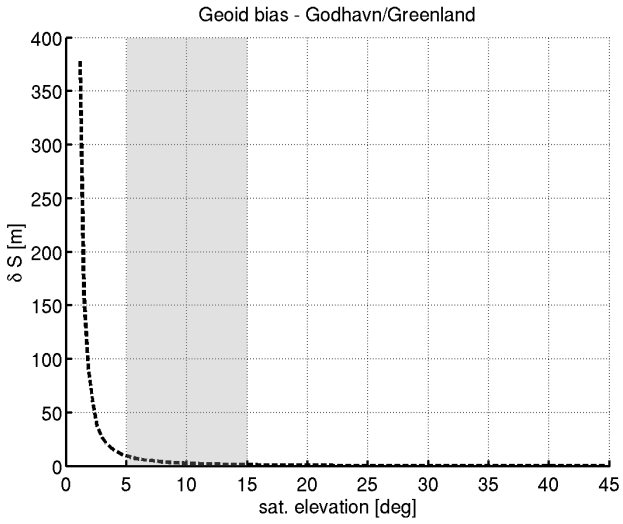

Figure 4.36: Simulations of topographic bias in the tangent arc vs. elevation of the satellite. The elevation range of observed reflections is shaded in grey.

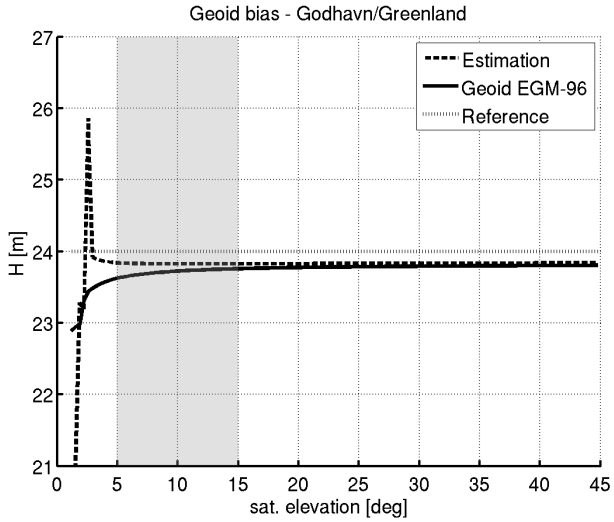

Figure 4.37: Simulations of topographic bias in the height vs. elevation of the satellite. The elevation range of observed reflections is shaded in grey.

4.3.7 Carrier Phase Windup

The circular polarisation of GNSS signals leads to a dependence of carrier phase measurements on the relative orientation between receiving and transmitting antennas. This so-called carrier phase *Windup* effect has been studied by [Wu et al., 1993]. Consequences for interferometric phase observations in a ground-based reflectometry setup were analysed in [Beyerle, 2008]. Crucial for the *Windup* in the *Godhavn* experiment is the 45° tilt of the receiving RHCP antenna w.r.t. *Zenith* direction. The *Windup* phase path for the interferometric signal is written

$$\Delta = \frac{\lambda_L}{2\pi}(\phi^{\mathrm{rfl}} - \phi),$$

where λ_L denotes the wavelength and ϕ^{rfl}, ϕ is the unwrapped phase on the reflected and the direct link, respectively. Expressions for both links assuming straight-line ray propagation (no refraction) are deduced in [Beyerle, 2008].
To quantify the bias in the height estimation, the path of a biased reference state is $L_{\mathrm{ref}}(\Delta, H^J) = L_r(H^J) - L_d + \Delta$, where the interaction between *Windup* and ray tracing is neglected. The path bias then simply reads $\delta L = \Delta$ and a bias in the tangent arc is not considered. The height estimation using the unbiased states of the altimetric model L^j_{alt} follows. Biases δL and δH are derived, see Fig. 4.38 and 4.39.

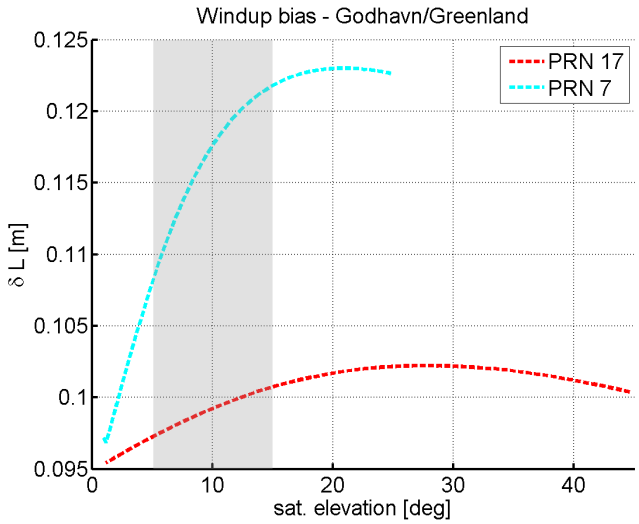

Figure 4.38: Simulations of *Windup* bias in the phase path vs. elevation of the satellite. The elevation range of observed reflections is shaded in grey.

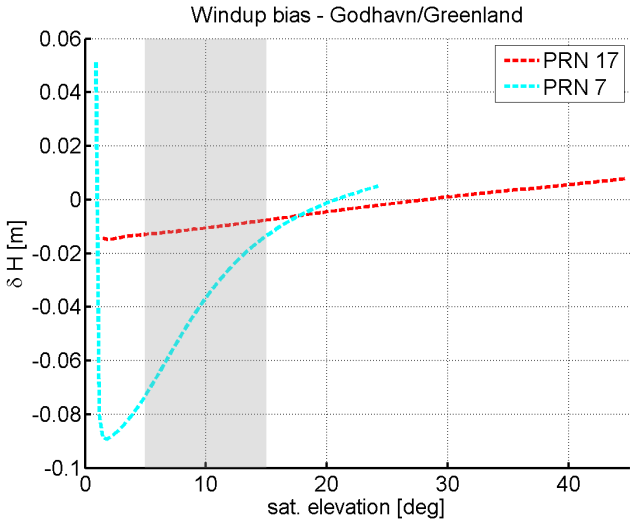

Figure 4.39: Simulations of *Windup* bias in the height vs. elevation of the satellite. The elevation range of observed reflections is shaded in grey.

Two reflection events are considered to account for differences in the geometry. The standard example, event `PRN 17 - 2009/01/18 17:04:55`, lies in southern direction near the antenna boresight. A different example, event `PRN 7 - 2009/01/18 18:21:45`, lies in the eastern direction with a difference in azimuth of about 80° to the antenna boresight. The changes of the *Windup* in the observed range are larger for the eastern event (13mm) than for the southern event (4mm). The corresponding height bias for the southern event is small (<1cm) but it is considerably large for the eastern event (6cm).

4.3.8 Receiver and Transmitter Clock

So far uncertainties of model parameters and further parameters have been regarded. A third aspect of clock uncertainties will be briefly discussed here, that is not directly related to the signal path model. Assuming a stable satellite clock the uncertainty of the receiver clock will be examined first. An interferometric acquisition on a single front-end means that direct and reflected signals are acquired simultaneously. The unbiased superposition arriving at the front-end has the interferometric frequency

$$\begin{aligned} f &= (f_{\mathrm{L}} + f_r) - (f_{\mathrm{L}} + f_d) \\ &= f_r - f_d \end{aligned}$$

where only the difference of the *Doppler* shifts remain. Its actual measurement by the receiver will be biased due to the unstable receiver clock. For the time standard the `GORS` receiver uses a quartz oscillator. A typical event at *Godhavn* last 20min ($\tau \approx 10^3$s). The stability of the oscillator during such an event is described by the Allan Deviation $\sigma_y(\tau = 10^3\mathrm{s}) \approx 10^{-9}$. The values are adopted from [Ashby, 2003], where also a brief explanation of the Allan Deviation can be found. The measured interferometric frequency,

typically $f \approx 1$Hz for the *Godhavn* experiment, has an uncertainty $\delta f \approx 10^{-9}$Hz. Recalling the altimetric sensitivity dH/df_0 in Tab. 3.1, the corresponding height error is in the sub-μm-range and can be neglected. However, a potential bias not characterized by the Allan Deviation is a drift of the clock. This effect has not been investigated yet.
We turn the focus now to the stability of the transmitter clock. The interferometric signal is acquired simultaneously at the receiver, i.e. the transmission epoch of the direct signal t_d and of the reflected signal t_r are not equal. The retardation $t_r - t_d$ of the reflected signal for the *Godhavn* setup it is about 1μs. The Allan Deviation does not refer to such small time intervals, the intrinsic noise processes of the transmitter clock must be considered to predict the uncertainty. Further analysis of the transmitter clock is necessary.

4.4 Conclusion

The conclusions are guided by the questions that have been raised already at the end of the introduction. A discussion and evaluation of each question will follow.

Is it possible to find an altimetric method for ocean roughness beyond the Fraunhofer Limit?

The significant wave height of the open ocean reaches several meters in Baffin Bay. It may decrease close to the coastal setup at *Godhavn* but still exceeds the Fraunhofer Limit. According to [Anderson, 1999], surface roughness is not a critical factor in using interferometry to determine the antenna height above water. The author gives the following arguments. In the capillary wave regime the effect of surface roughness is a reduction in the amplitude of the reflected component. For gravity waves there is essentially no effect as the time average of height of the waves is zero.
A crucial point in this statement is the time average. Not for all observations an averaging is possible to reduce the roughness effect of gravity waves. The simulations showed that the retrieval of heights is affected by the noise introduced on the surface. A Continuous Tracking of interferometric phase observation during the *Godhavn* campaign revealed to be useless. Continuous tracks are sparse and interrupted by fading. An empirical tracking of height changes is pointless. The altimetric method proposed here creates stationary reflection states that allow an averaging. The residual *Doppler* can be regarded as the result of the averaging. The surface height is discriminated from the height correlation of the residual *Doppler*.
A Tracking Retrieval and a Spectral Retrieval of the residual *Doppler* are distinguished. Simulations show a different altimetric performance for a rough ocean surface. The Tracking Retrieval, that is restricted to continuous phase tracks, can be applied only during the last days of the campaign. The Spectral Retrieval in the frequency domain is not restricted to continuous tracks and can be applied throughout the *Godhavn* campaign.
Furthermore the Spectral Retrieval requires no additional filters. The *Doppler* precision is then only dependent on the spectral resolution, which is the inverse of the observation period. The formal altimetric precision is in the decimeter range (e.g. Tab. 4.2). To achieve a centimeter precision, an interval that is at least 5 times longer is needed. But such an interval is out of scope for the present experiment, as the duration of events is limited by the elevation interval $[5...15]^\circ$. A retrieval including the intervals of different events could be considered to improve precision in future studies.
The application of the Tracking Retrieval is more sensitive. The formal precision for a chosen event with continuous phase tracks can be in the centimeter range (e.g. Tab. 4.2) but it fails for monitoring under common roughness conditions of the open ocean. The number of coherent observations determines the precision, cf. eq.(4.6). The application of the Tracking Retrieval at the onset of sea-ice formation is described in [Semmling et al., 2011]. Its sensitivity to ocean roughness, as an indicator for the occurrence of sea-ice, and the height estimates for tidal analysis were exploited.

Can we observe the onset of sea-ice formation and an increasing *Freeboard* height?

A decrease in surface roughness is connected with the transition from open water to sea-ice coverage. The transition that is shown in the ice charts (Fig. 2.7), coincides with an increase of coherent observations (Fig. 4.9). Unfortunately the observation period with a presence of sea-ice was too short to study the development of the ice *Freeboard*. A temporary loss of coherence in the presence of close drift ice occurs for DoY 14 in 2009 (Fig. 4.9). An explanation is provided by a significant peak in the wind component from southern direction (Fig. 2.6). A strong wind from this direction pushes the ice floes towards the coast and may influence the surface roughness.
Next to the number of coherent observations, the residual in the *Doppler* is related to surface roughness. It indicates a bias from the specular model. The offset in the residual, for instance between DoY [336...346]/2008 and DoY 14/2009 (Fig. 4.10), coincides with south wind (Fig. 2.6). The direction dependence for wind driven waves and ice floes is remarkable. A dedicated model relating the residual *Doppler* to wave properties is required. The Spectral Retrieval in particular is suited not only for altimetry but also to study other properties of the ocean and sea-ice surface.
Roughness is described statistically and is not localized in the footprint of the reflection. Topographic effects, e.g. icebergs of a larger category, are a local phenomenon in the footprint. They might corrupt the specular surface model but locating them is difficult. The occurrence of icebergs during the *Godhavn* experiment is most likely. The proof of single events, however, was not possible due to a leakage of ancillary iceberg data. A dedicated study on icebergs is required.

Is it possible to resolve ocean tides from the altimetric time series?

Ocean tides were observed during the whole campaign, even when compact sea-ice occurs in the area (indicating that it is still not fastened onshore). The tides are easier to analyse using reflection events than other phenomena. A localization w.r.t. the footprint is not necessary. Furthermore tide models, e.g. AODTM-5, are available and provide predictions with a high resolution. The tide spectrum, that was derived from the long altimetric time series, stresses the monitoring qualities of GNSS reflections.

Can we prove an effect of *Geoid* undulations in the altimetric results?

An effect on altimetry is expected due to the *Geoid* undulations that occur at the steep coast of *Disko Island*. Variations in the gravity field change the ocean topography as described by a *Geoid* model. The ray tracing used in the altimetric method neglects undulations of the *Geoid* model. A bias induced by such an undulation within the footprint of a reflection event was simulated. An overestimation due to the *Geoid* is predicted, that reaches up to 20cm, see Fig. 4.37. An undulation profile deduced from the observations is not feasible. But the *Geoid* bias as a source of overestimation is supported by Fig. 4.13. A large overestimation of the surface height occurs for events in southern direction.

The effect decreases for events in eastern and western direction that lie along the coast. An explanation gives the *Geoid* which has a gradient perpendicular to the coast line and therefore affects in particular events in southern direction.

Which altimetric bias persists due to the uncertainty in the tropospheric model?

The ray tracing computes the optical phase path considering the refractivity in the troposphere. The refractive delay is modelled. The comparison of the slant delay estimates and model calculations based on `ECMWF` profiles reveals an remaining error <1% in the refractivity model. The respective bias for altimetric results due to over- or underestimation of the refractivity reaches up to 20cm at lowest elevation angles. Observations at higher elevation angles are recommended for future experiments.

Is there a dispersion in the altimetric results and is the bias predictable by the ionospheric model?

No dispersion in the altimetric results is observed. Taking into account that the precision for a single event lies in the decimeter range, a dispersive bias in centimeter range may remain unresolved. To model ionospheric refractivity an *F-layer* was assumed with a given distribution of electrons. The total electronic content (`TEC`) was observed during the campaign. The vertical `TEC` typically lies at about 5`TEC`-units and never exceeded 15`TEC`-units. In the altimetric retrieval ionospheric refraction was ignored. Simulations show that a dispersive altimetric bias that can be expected by a constant *F-layer* reaches 3.5cm at most for `L2` and 2cm for `L1`. Within the observed range of elevation the maximum bias occurs at 10°. The dispersion predicted for `L1` and `L2` is below the precision and is not relevant for such a ground-based setup. A fading due to ionospheric scintillation especially at low elevation may occur but cannot be distinguished from fading induced by roughness. The deviation of continuous tracks filtered on `L1` and `L2` could be either related to the ionospheric dispersion or to ocean roughness.

Can we use Slant Interferometry on a flying platform?

An averaging of carrier observation to overcome the influence of ocean roughness is especially complicated if the receiver is in motion. A precise trajectory can be used to model the effect of receiver motion and to create pseudo-stationary reflection states also for a flight experiment. The correlation of the residual *Doppler* yields estimates of the surface height. That means the method, that was extensively described here for a coastal setup, could be even more valuable to use Slant Interferometry on a flying platform.

4.5 Outlook

There are objectives that could not be achieved within the *Godhavn* experiment. In particular an increase of the surface height caused by the *Freeboard* of sea-ice could not be observed. There was no data for in-situ validation available and the observation interval coinciding with a presence of sea-ice is short. Progress in this issue can be achieved if the large number of observed events is continued in the sea-ice period. Referring to the other receiver setup in the *Godhavn* experiment [Fabra et al., 2011], a comparison of altimetric results and ancillary `MODIS` data w.r.t. sea-ice thickness can be found. There a smaller number of reflection traces on ground but over a longer interval was recorded.
A general drawback of interferometric observations is the low `SNR` due to residual noise. A precise retrieval is not achieved in a short time, long time averaging is required. The concept of a stationary reflection state, that was widely used in this work, offers one possibility to average and to amplify the specular part of the signal in the frequency domain. A better understanding of non-specular contribution in the residual spectrum is needed. The simulation study showed that the Peak-to-Noise-Ratio is related to surface roughness. The retrieval of the significant wave height is feasible. An early detection of a tsunami pattern within the ocean-clutter will be, however, difficult. The residual peak dominates the spectrum but scatterers with a geometry different from the specular point contribute to the spectrum as well. The detection of scatters, like icebergs or ships, using the Spectral Retrieval is worth more investigations.
A significant peak in the residual spectrum occurs in the *Godhavn* experiment that can be related to solid ground reflections close to the receiver. Such a coherent multipath is a common bias in geodetic observations and has been exploited in interferometric studies (classified as Multipath Interferometry in Sec. 1.2). Especially the influence of soil moisture [Larson et al., 2010], snow [Larson et al., 2009] and vegetation coverage [Rodriguez-Alvarez et al., 2011] are currently investigated and offer further applications.
In general there is broad potential for carrier observations in reflectometry. A code observation pays off only for a sufficient retardation of the reflection. Even with modernised codes such a retardation is only achieved in airborne or spaceborne setups. Also the codeless approach [Rius et al., 2011] requires such a setup to achieve a discrimination of transmitters using the Delay or *Doppler*. Carrier observations in contrast are widely studied: ground-based to use the large infrastructure of existing reference stations and spaceborne in combination with other sensor e.g. `RO` receivers. A dedicated receiver (e.g. the `GORS` receiver) in combination with a dedicated method permits also airborne applications, as we saw for the proof-of-concept in the *Zeppelin* experiment.

Appendix A

Tables

Positioning

x	=	1,345,499.748	m
y	=	-1,821,228.257	m
z	=	5,943,413.881	m

Table A.1: Precise Point Position estimate of up-looking antenna in `ITRF-2000` coordinates.

$\Delta\phi$	=	-3 E^{-6}	°
$\Delta\lambda$	=	6 E^{-6}	°
ΔH	=	-42	cm

Table A.2: Relative position estimate of the tilted antenna w.r.t the up-looking antenna in `WGS-84` coordinates. A decimeter precision is sufficient for North and East components that are less important than the height.

Setup Parameters

ϕ_{R}	=	69.271694	° N	geodetic latitude of the `GORS` antenna (`WGS-84`)
λ_{R}	=	53.543487	° W	geodetic longitude of the `GORS` antenna (`WGS-84`)
H_{R}	=	691.62	m	ellipsoidal height of the `GORS` antenna (`WGS-84`)
H_{A}	=	24.00	m	apriori surface height given by the *Geoid*
$E_{\max}$	=	15	°	max. elevation angle of observation limited by the coast line
$E_{\min}$	=	5	°	min. elevation angle of observation limiting the coupling

Table A.3: Parameters of the *Godhavn* setup. A decimeter precision is sufficient for ϕ_{R} and λ_{R}, that are less important than H_{R}.

Scientific Technical Report STR 12/04
DOI: 10.2312/GFZ.b103-12049
Deutsches GeoForschungsZentrum GFZ

Ellipsoidal Height Axis

H_1	=	-2	km	minimum height
H_N	=	1500	km	maximum height
$H_{j+1} - H_j$	=	25	m	height resolution
$\hat{H}$	=	7	km	scale height of atmosphere

Table A.4: Parameters defining a uniform height axis for the troposphere and ionosphere model.

Ionospheric Layers

$H_0^{\mathtt{F}}$	=	300	km	height of *F-Layer* peak
$D^{\mathtt{F}}$	=	60	km	thickness of *F-Layer*
$\hat{\eta}^{\mathtt{F}}$	=	3 E^{12}	m^{-3}	peak density of *F-Layer*
$H_0^{\mathtt{E}}$	=	105	km	height of *E-Layer* peak
$D^{\mathtt{E}}$	=	5	km	thickness of *E-Layer*
$\hat{\eta}^{\mathtt{E}}$	=	2 E^{11}	m^{-3}	peak density of *E-Layer*

Table A.5: Parameters for the ionosphere model.

Shell Thickness

dH	$\geq$	10	m	shell thickness in the troposphere
H	$\geq$	10	km	lower boundary of the stratosphere
dH	$\geq$	50	m	shell thickness in the stratosphere
H	$\geq$	100	km	lower boundary of the ionosphere
dH	$\geq$	100	m	shell thickness in the ionosphere

Table A.6: Thresholds to limit the shell thickness.

Appendix B

Signal Path Model

Specific remarks on the signal path model are attached here. For a spherical surface the arc distance and its relation to the spherical latitude and longitude are deduced using a spherical triangle. A detailed case study for direct, incident and scattered rays is added, that goes beyond the Godhavn experiment. Changes in trace path monotony are considered, that generalize the concept even for rays with negative elevation angles.

Spherical Surface

The Haversine Formula provides the relation of a reference angle and all sides in an spherical triangle. We use the fundamental form in terms of sin and cos

$$\cos a = \cos b \cos c + \sin b \sin c \cos \alpha. \tag{B.1}$$

The small letters denote the sides and α the reference angle lying opposite to side a. This formula can either be used to determine the latitude and longitude position of a point using the distance and bearing from a starting point or to calculate the arc distance of to points lying on a spherical surface. In the following a spherical triangle is defined by three points R, A and P lying on a spherical surface of the Earth, see Fig. B.1.
The azimuth bearing α in R is the angle opposite to the side given by the co-latitude $90^\circ - \phi_A$. The side opposite to A is the co-latitude $90^\circ - \phi_R$, respectively. The angle in P is the difference in longitude $\Delta\lambda = \lambda_A - \lambda_R$ and the side opposite to P is the arc distance d. For determination of the position ϕ_A, λ_A, the position of the receiver ϕ_R, λ_R are needed as well as azimuth bearing α and the distance d. Eq.(B.1) can be written referring to the angle α and the angle $\Delta\lambda$

$$\begin{aligned} \cos(90^\circ - \phi_A) &= \cos(90^\circ - \phi_R) \cos\frac{d}{r} + \sin(90^\circ - \phi_R) \sin\frac{d}{r} \cos\alpha, \\ \cos\frac{d}{r} &= \cos(90^\circ - \phi_A) \cos(90^\circ - \phi_R) \\ &\quad + \sin(90^\circ - \phi_A) \sin(90^\circ - \phi_R) \cos(\lambda_A - \lambda_R). \end{aligned} \tag{B.2}$$

On the unit sphere the arc distance d is normalized by the Earth radius r. The sin of the co-latitude can be substituted with the cos of the latitude and vice versa. Then the equations are solved for the coordinates of A

Scientific Technical Report STR 12/04
DOI: 10.2312/GFZ.b103-12049

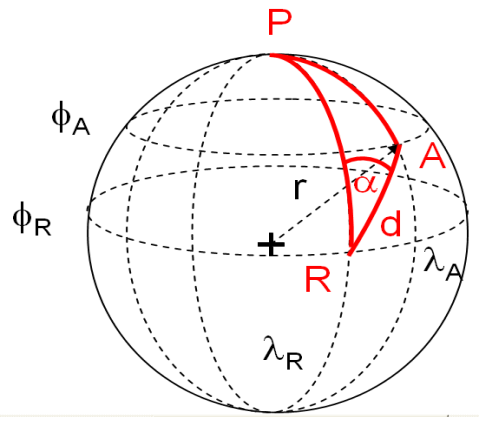

Figure B.1: Spherical triangle consisting of the receiver position R, an a priori point A and the North pole denoted P. It is lying on the Earth surface, approximated with a sphere of radius r.

$$\begin{aligned} \phi_{\mathrm{A}} &= \arcsin\left(\cos\alpha\cos\phi_{\mathrm{R}}\sin\frac{d}{r}+\sin\phi_{\mathrm{R}}\cos\frac{d}{r}\right), \\ \lambda_{\mathrm{A}} &= \arccos\left(\frac{\cos\frac{d}{r}-\sin\phi_{\mathrm{R}}\sin\phi_{\mathrm{A}}}{\cos\phi_{\mathrm{R}}\cos\phi_{\mathrm{A}}}\right)+\lambda_{\mathrm{R}}. \end{aligned}$$

The arc distance is approximated with the horizontal distance d. The azimuth α of the transmitter is used for the bearing of A. For determination of the arc distance between R and A the coordinates ϕ_{R}, λ_{R} and ϕ_{A}, λ_{A} are given. From eq.(B.2) the arc distance is derived

$$d = r\arccos\left(\sin\phi_{\mathrm{R}}\sin\phi_{\mathrm{A}}+\cos\phi_{\mathrm{R}}\cos\phi_{\mathrm{A}}\cos\Delta\lambda\right).$$

Propagation of Direct Ray

The propagation of the direct signal in a concentric distribution $N(\rho)$ is determined by the location of the transmitter X, the receiver R and the tangent point T. The tangent point is located in the perigee of the ray, Fig. B.2. The impact parameter P of the ray relates to the corresponding T

$$P_{\mathrm{T}} = \rho_{\mathrm{T}}\, N(\rho_{\mathrm{T}}).$$

The radius of the tangent point is here denoted ρ_{T}. The impact parameter is preserved along the propagation of the direct ray. However, the calculation of $\Theta_{\mathrm{XR}}(P)$ requires a case-by-case analysis. A first case is shown in Fig. B.2 and a second one in Fig. B.3.
In the first case the signal propagates monotonously from X to R_1. The integration path needs not be divided in this case. In the second case signal propagation is not monotone from X to R_2. The signal path reaches a minimum in ρ at the tangent point. The path

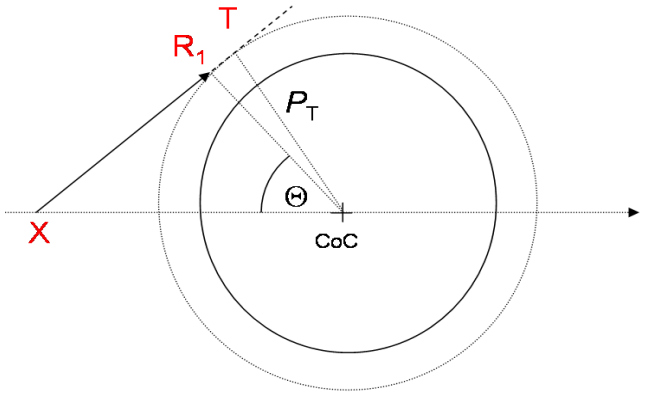

Figure B.2: First case of direct ray propagation. The receiver lies before the tangent point. Propagation is monotone in the radius ρ. For simplicity signal bending is neglected in this scheme.

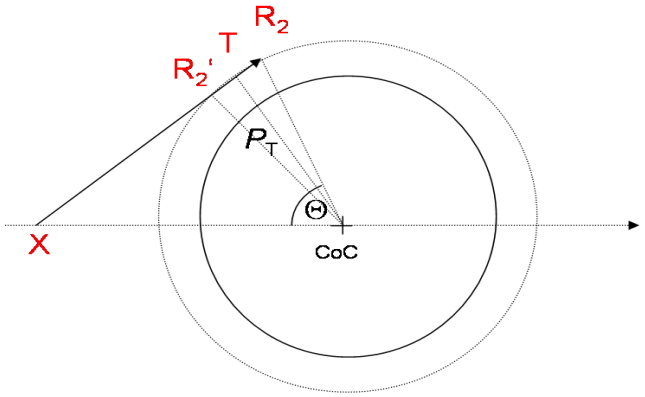

Figure B.3: Second case of direct ray propagation. The receiver lies after the tangent point. Propagation is non-monotone in the radius ρ. The path of integration needs to be divided. For simplicity signal bending is neglected in this scheme.

decreases monotonously from X to T and increases monotonously from T to R_2. For integration a split-up of the path is required in the second case. If R'_2 is chosen in a symmetric position to R_2 w.r.t. the tangent point, the path can be divided as follows

$$\Theta_{XR} = \Theta_{XR'} + 2\,|\Theta_{TR}|\,. \tag{B.3}$$

It is used that $\Theta_{R'T} = \Theta_{TR}$. A clear distinction between the first case and the second case is given by the tangent point. If T is excluded from the path, propagation is monotone. If T is included in the path, propagation is non-monotone and needs to be split up. According to this case studies the angular distance $\Theta_{XR}(P)$ can be calculated provided that refractivity $N(\rho)$, constellation {X,R} and the impact parameter P are known. Apriori the impact parameter is not known but an iterative ray tracing algorithm uses a residual trace $\Delta\Theta$ to

find P_{T}.

$$\Delta\Theta(P) = \Theta_{\mathrm{XR}}(P) - \Theta$$

For the trace integral $\Theta_{\mathrm{XR}}(P)$ an apriori impact parameter P is assumed. The angle Θ is given by the constellation.

$$\Theta = \arccos\left(\frac{\vec{\rho_{\mathrm{X}}}}{\rho_{\mathrm{X}}} \cdot \frac{\vec{\rho_{\mathrm{R}}}}{\rho_{\mathrm{R}}}\right) \tag{B.4}$$

The residual trace $\Delta\Theta$ vanishes for the trace integral with the impact parameter of tangent point T. The impact parameter P is adjusted iteratively to minimize $\Delta\Theta$.

$$\Delta\Theta|_{P=P_{\mathrm{T}}} = 0$$

Once P_{T} is determined, the optical phase path of the direct signal is calculated according to eq.(3.8). For the first case when T is excluded, the following is obtained.

$$L_d = L_{\mathrm{XR}}$$

In the second case when T splits up the integration path, the optical path can be written as follows.

$$L_d = L_{\mathrm{XR'}} + 2\,|L_{\mathrm{TR}}|$$

Propagation of Incident and Scattered Ray

The propagation of the reflected signal, which obeys Snell's Law, has an additional constraint given by the specular point S. Apart from grazing elevation angles, ρ_{S} is the minimum radius within the propagation of the reflected signal. We neglect the exception of grazing angles and consider the case of an incident ray, monotonously decreasing in ρ from X to S, and a scattered ray, that monotonously increases from S to R, as shown in Fig. B.4. The propagation of each ray is determined by a tangent point T which is excluded from the signal path. A reflecting surface that is tangent to `CoC`, yields a symmetric propagation of the incident and the scattered ray. The impact parameter P_{T} is then equal for both rays. A reflecting surface, that has a slope w.r.t. the tangent, breaks symmetry yielding different impact parameters for the incident and the scattered ray. It is assumed that the reflecting surface is tangent. Using symmetry, a point R' is found that fulfills $\Theta_{\mathrm{R'S}} = \Theta_{\mathrm{SR}}$, then the path can be split up into segments analogously to the direct signal in eq.(B.3).

$$\Theta_{\mathrm{XR}} = \Theta_{\mathrm{XR'}} + 2\,|\Theta_{\mathrm{SR}}|\,. \tag{B.5}$$

The ray tracing is then similar to the algorithm for the direct signal. An additional constraint is set by the radius $\rho_{\mathrm{S}} = H_{\mathrm{S}} + R_c$ of the specular point, that comprises the height of the reflecting surface. Multiple impact parameters P^k are determined for preset heights H_{S}^k. Analogously to the direct signal, P^k is determined by iteration minimizing the residual trace.

$$\Delta\Theta(P^k, H_{\mathrm{S}}^k) = \Theta_{\mathrm{XR}}(P^k, H_{\mathrm{S}}^k) - \Theta$$

The angle Θ is given by the constellation and is computed according to eq.(B.4). Further calculation are performed for the different height levels, the index k is dropped for convenience. The impact parameter P determined by the ray tracing is used according to eq.(3.8), to calculate the optical phase path of the reflected signal.

$$L_r \quad = \quad L_{\mathrm{XR'}} + 2\, L_{\mathrm{SR}} \tag{B.6}$$

The angle Θ_{RS} is traced analogously using eq.3.8. It is used to derive the latitude ϕ_{S} and longitude λ_{S} of the specular point for a given radius ρ_{S} in the CC frame.

$$\begin{aligned} \phi_{\mathrm{S}} &= \arcsin\left(\cos\alpha\cos\phi_{\mathrm{R}}\sin\Theta_{\mathrm{RS}} + \sin\phi_{\mathrm{R}}\cos\Theta_{\mathrm{RS}}\right) \\ \lambda_{\mathrm{S}} &= \arccos\left(\frac{\cos\Theta_{\mathrm{RS}} - \sin\phi_{\mathrm{R}}\sin\phi_{\mathrm{S}}}{\cos\phi_{\mathrm{R}}\cos\phi_{\mathrm{S}}}\right) + \lambda_{\mathrm{R}} \end{aligned}$$

Strictly speaking, a transformation of ellipsoidal coordinates ϕ, λ in WGS-84 to spherical coordinates in the CC frame is required. The loss of precision in ϕ, λ is accepted here, as only the height precision is of interest.

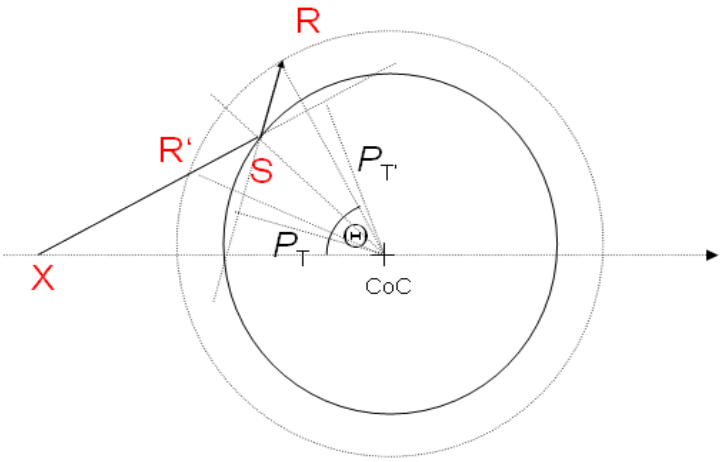

Figure B.4: Ray propagation of the reflected signal. The reflection is specular, the propagation of the incident ray from X to S and the reflected ray from S to R are symmetric. The tangent points T and T' are excluded.

Appendix C

Acronyms & Glossary

Acronyms

AODTM-5	Arctic Ocean Dynamics-based Tidal Model on 5-km regular grid
C/A	Coarse Acquisition code
CC	Curvature Centered
CDMA	Code Division Multiple Access
ChaMP	Challenging Mini-satellite Payload
CL	Civilian Long length code
CM	Civilian Moderate length code
CoC	Centre of Curvature
DLL	Delay Lock Loop
DLR	Deutsches Zentrum für Luft- und Raumfahrt
GC	GeoCentric (Earth Centered)
GeSOC	German Space Operations Center
EADS	European Aeronautic Defence and Space Company
ECMWF	European Centre for Medium-Range Weather Forecasts
EGM-96	Earth Gravitational Model 1996
EPOS	European Plate Boundary Observing System
ESA	European Space Agency
DMI	Danmarks Meteorologiske Institut
DoY	Day of the Year
GFZ	GeoForschungsZentrum Potsdam
GNSS	Global Navigation Satellite System
GOLD-RTR	GPS Open Loop Differential Real-Time Receiver
GORS	GNSS receiver for Occultation Reflectometry and Scatterometry
GPS	Global Positioning System
IEEC	Institut d'Estudies Espacial de Catalunya
IF	Intermediary Frequency
IFE	Institut für Erdmessung Hannover
IGG	Institut für Geodäsie und Geoinformationstechnik
IGS	International GNSS Service
ITRS	International Terrestrial Reference System

Scientific Technical Report STR 12/04
DOI: 10.2312/GFZ.b103-12049

K1	lunisolar diurnal tide constituent
LEO	Low Earth Orbiter
L1, L2	GPS carriers in L-band
L2C	L2 Civilian code
M2	principal lunar semidiurnal tide constituent
MODIS	Moderate-resolution Imaging Spectroradiometer
NASA	U.S. National Aeronautics and Space Administration
OSO	Onsala Space Observatory
PLL	Phase Lock Loop
PNR	Peak to Noise Ratio
PRN	Pseudo Random Noise
RaDaR	Radio Detection and Ranging
RHCP	Right-Handed Circular Polarisation
RO	Radio Occultation
S2	principal solar semidiurnal tide constituent
SIDS	Sea-Ice and Dry Snow
SNR	Signal to Noise Ratio
SWH	Significant Wave Height
TC	TopoCentric (Location Centered)
TEC	Total Electron Content
TZD	Total Zenith Delay
WGS-84	World Geodetic System 1984
ZLT	Zeppelin LuftschiffTechnik GmbH & Co. KG

Glossary

Crater Lake	lake filling a 655m deep caldera located in Oregon (USA), the Cloudcap Lookout lies about 480m above the lake level
Disko Island	large island off the west coast of Greenland, to the south of the island lies *Disko Bay*
Doppler	short form for the interferometric observation of the carrier frequency that results from the changing geometry of transmitter, receiver and specular point
E-layer	middle layer of the ionosphere, ionizing radiation with wavelengths 1-10nm
F-layer	uppermost layer of the ionosphere with the highest density of charges, ionizing radiation with wavelengths 10-100nm
Freeboard	height of an ice floe above the water surface
Geoid	equipotential surface w.r.t. the Earth's gravity field, that coincides with the Earth's mean ocean surface, assuming that oceans are in equilibrium
Godhavn	(Inuit: Qeqertarsuaq) a port and a town on the south coast of *Disko Island* and location of the experiment
Jamming	interference of radio signals that lead to a loss of signal information
Königsstuhl	limestone rock at the coast on Rügen island (Germany), offering a view at about 118m over the Baltic Sea
La Mola	highest mountain in the nature park Sant Llorenç del Munt, with the form of a millstone
Master Correlation	specific implementation in the `GORS` receiver to acquire the correlation sum of the direct signal
Nadir	indicates the downward direction perpendicular to the astronomical horizon, from the Arabic word for foot point
Oosterschelde	river delta in Zeeland (Netherlands) at the confluence of Rhein, Maas and Schelde, the Zeelandbrug crosses the delta with an height of about 18m
Osculation	in the geometrical sense it is an approximation of a complex curve/surface by a simpler one
Phasor	complex representation of a signal including amplitude and phase information
Prompt Correlation	common implementation in `GPS` receivers to acquire the correlation sum of the signal
Replica	local copy of the `PRN` code in common `GPS` receivers
Radio Occultation	remote sensing technique to measure physical properties of atmosphere, when the signal of a radio source is at low elevation angles
Scripps Pier	pier belonging to the Scripps Institution of Oceanography in La Jolla (USA), leading in about 10m height from the beach to the sea

Slave Correlation	specific implementation in the GORS receiver to acquire the correlation sum of the reflected signal
Sputnik	first spacecraft and radio transmitter in orbit, launched on 4 October 1957
Transit	first operational satellite navigation system, developed for the U.S. Navy
Windup	bias in the phase measurement of the circular polarised GNSS signal induced by antenna orientation
Wipeoff	element of signal processing to remove code or carrier signatures
Zenith	indicates the upward direction perpendicular to the astronomical horizon, derived from the Arabic expression for above the head
Zeppelin	rigid airship pioneered by Graf Ferdinand von Zeppelin in the early 20th century that is continued today as a semi-rigid type

Bibliography

D. C. Agnew and K. M. Larson. Finding the repeat times of the GPS constellation. *GPS Solutions*, 11: 71–76, 2007.

K. D. Anderson. Determination of water level and tides using interferometric observations of GPS signals. *Journal of Atmospheric and Oceanic Technology*, 17:1118–1127, 1999.

N. Ashby. Relativity in the Global Positioning System. *Living Reviews in Relativity*, 6, 2003.

P. Beckmann and A. Spizzichino. *The Scattering of Electromagnetic Waves from Rough Surfaces*. Artech House, Inc., Nordwood, MA, 1987. Reprint. Originally published: Oxford [Oxfordshire]; New York : Pergamon Press, 1963. (International Series of Monographs on Electromagnetic Waves; 4).

M. Belmonte Rivas and M. Martin-Neira. Coherent GPS Reflections From the Sea Surface. *IEEE Geoscience and Remote Sensing Letters*, 3(1):28–31, 2006.

M. Bender, G. Dick, J. Wickert, M. Ramatschi, M. Ge, G. Gendt, M. Rothacher, A. Raabe, and G. Tetzlaff. Estimates of the information provided by GPS slant data observed in Germany regarding tomographic applications. *Journal of Geophysical Research*, 114, 2009.

M. Bevis, S. Businger, S. Chiswell, T. A. Herring, R. A. Anthes, C. Rocken, and R. H. Ware. GPS meteorology: Mapping zenith delays onto precipitable water. *Journal of Applied Meteorology*, 33:379–386, 1994.

G. Beyerle. Carrier phase wind-up in GPS reflectometry. *GPS Solutions*, 2008. doi: 10.10007/s10291-008-0112-1.

G. Beyerle, K. Hocke, J. Wickert, T. Schmidt, C. Marquardt, and C. Reigber. GPS radio occultations with CHAMP: A radio holographic analysis of GPS signal propagation in the troposphere and surface reflections. *Journal of Geophysical Research*, 107(D24):4802–4815, 2002. doi: 10.1029/2001JD001402.

M. Born and E. Wolf. *Principles of optics*. Cambridge University Press, 1999.

K. Borre, D. M. Akos, N. Bertelsen, P. Rinder, and S. Holt Jensen. *A Software-defined GPS and Galileo Receiver*. Birkhäuser, 2007.

M. Caparrini, L. Ruffini, and G. Ruffini. PARFAIT: GNSS-R coastal altimetry. In *Workshop on Oceanography with GNSS Reflections*, 2003.

E. Cardellach, C. O. Ao, M. de la Torre Juarez, and G. A. Hajj. Carrier phase delay altimetry with GPS-reflection/occultation interferometry from low earth orbiters. *Geophysical Research Letters*, 31: L10402, 2004. doi: 10.1029/2004GL019775.

D. J. Cho, C. Park, and S. J. Lee. An assisted GPS acquisition method using L2 civil signal in weak signal environment. *Journal of Global Positioning Systems*, 3(1-2):25–31, 2004.

T. A. Croft and H. Hoogasian. Exact Ray Calculations in a Quasi-Parabolic Ionosphere With No Magnetic Field. *Radio Science*, 3(1):69–74, 1968.

D. Diemand. Icebergs. *Encyclopedia of Ocean Sciences*, pages 1255–1264, 2003. doi: 10.1006/rwos.2001.0002.

F. Fabra, E. Cardellach, A. Rius, S. Ribó, S. Oliveras, M. Belmonte, M. Semmling, and S. D'Addio. Phase Altimetry with Dual Polarization GNSS-R over Sea Ice. *IEEE Trans. Geosci. and Remote Sens.*, 50(6):10, 2011. doi: 10.1109/TGRS.2011.2172797.

R. Fontana, W. Cheung, P. M. Novak, and T. Stansell. The New L2 Civil Signal. In *Proceedings of the ION 2001 International Technical Meeting*, pages 617–631, 2001.

O. K. Garriott and R. N. Bracewell. Satellite Studies of the Ionization in Space by Radio. *Advances in Geophysics*, 8:85–135, 1961.

G. Gendt, G. Dick, and W. Soehne. GFZ analysis center of IGS - annual report 1998. Technical report, IGS, 1998.

D. C. Ghiglia and M. D. Pritt. *Two-Dimensional Phase Unwrapping: Theory, Algorithms, and Software*, chapter Phase Data, Quality Maps, Masks, and Filters, pages 59–100. John Wiley & Sons, inc., 1998.

K. Q. Hansen, H. S. Andersen, S. H., H. G. Karlsen, and J. Bille-Hansen. Distribution and Variability of Icebergs in Eastern Davis Strait 63deg N to 68deg N. Technical report, Danish Meteorological Institute, Greenland Survey, ASIAQ, 2001.

A. Helm. *Ground-Based GPS Altimetry with the L1 OpenGPS Receiver Using Carrier Phase-Delay Observations of Reflected GPS Signals.* Technische Universität Berlin, Fakultät VI Bauingenieurwesen und Angewandte Geowissenwissenschaften, Fachgebiet Satellitengeodäsie und Erdsystemforschung, GFZ, Scientific Technical Report STR08/10, 2008.

A. Helm, O. Montenbruck, J. Ashjaee, S. Yudanov, G. Beyerle, R. Stosius, and M. Rothacher. GORS - a GNSS occultation, reflectometry and scatterometry space receiver. In *ION GNSS 2007, pp. 2011-2021*, 2007.

K. M. Larson, E. E. Small, E. D. Gutmann, A. L. Bilich, J. J. Braun, and V. U. Zavorotny. Use of GPS receivers as a soil moisture network for water cycle studies. *Geophysical Research Letters*, 35:L24405, 2008. doi: 10.1029/2008GL036013.

K. M. Larson, E. D. Gutmann, V. U. Zavorotny, J. J. Braun, M. W. Williams, and F. G. Nievinski. Can we measure snow depth with GPS receivers? *Geophysical Research Letters*, 36:L17502, 2009. doi: 10.1029/2009GL039430.

K. M. Larson, J. Braun, E. Small, V. Zavorotny, E. Gutmann, and A. Bilich. GPS Multipath and Its Relation to Near-Surface Soil Moisture Content. *IEEE J. Sel. Top. Appl. Earth Observ. Remote Sens.*, 3(1):91 – 99, 2010.

J. S. Löfgren, R. Haas, and J. M. Johansson. Monitoring coastal sea level using rerflected GNSS signals. *Advances in Space Research*, 47:213–220, 2011.

S. T. Lowe, C. Zuffada, Y. Chao, P. Kroger, L. E. Young, and J. L. LaBrecque. 5-cm-precision aircraft ocean altimetry using GPS reflections. *Geophysical Research Letters*, 29(10):1375–1378, 2002. doi: 10.1029/2002GL014759.

M. Martin-Neira. A passive reflectometry and interferometry system (PARIS): Application to ocean altimetry. *ESA Journal*, 17:331–355, 1993. Radio-Frequency Division, ESTEC, Noordwijk, The Netherlands.

M. Martin-Neira, P. Colmenarejo, G. Ruffini, and C. Serra. Altimetry precision of 1 cm over a pond using the wide-lane carrier phase of GPS reflected signals. *Canadian Journal of Remote Sensing*, 28(3):394–403, 2002.

D. Meschede. *Gerthsen Physik*. 19. Auflage. Springer-Verlag, 2002.

P. Misra and P. Enge. *Global Positioning System - Signals, Measurements, and Performance*. Ganga-Jamuna Press, Lincoln, Massachusetts, 2001.

O. Nogues-Correig, E. Cardellach, J. Sanz Campderros, and A. Rius. A GPS-reflections receiver that computes doppler/delay maps in real-time. *IEEE Transactions on Geoscience and Remote Sensing*, 45 (1):156–174, 2007. doi: 10.1109/TGRS.2006.882257.

L. Padman and S. Erofeeva. A barotropic inverse tidal model for the Arctic Ocean. *Geophys. Res. Lett.*, 31:L02303, 2004. doi: 10.1029/2003GL019003.

B. W. Parkinson, T. Stansell, R. Beard, and K. Gromov. A history of satellite navigation. *Navigation*, 42(1):109–164, 1995.

J. A. Pierce. True height of an ionospheric layer. *Physical Review Letters*, 71(10):698–706, 1947.

M. Ramatschi. *Untersuchung von Vertikalbewegungen durch Meeresgezeitenauflasten an Referenzstationen auf Grönland*. PhD thesis, Technische Universität Clausthal, 1998.

E. J. M. Rignot. Effect of Faraday Rotation on L-band Interferometric and Polarimetric Synthetic-Aperture Radar Data. *IEEE Trans. Geosci. and Remote Sens.*, 38(1):383–390, 2000.

A. Rius, E. Cardellach, and M. Martin-Neira. Altimetric analysis of the sea surface GPS reflected signals. *IEEE Transactions on Geoscience and Remote Sensing of Environment*, 10, 2010.

A. Rius, E. Cardellach, S. Oliveras, E. Valencia, H. Park, A. Camps, H. van der Marel, R. van Bree, B. Altena, S. Nogues-Corréig, O.and Ribó, J. Tarongí, and M. Martín-Neira. Altimetry with GNSS-R interferometry: first proof of concept experiment. *GPS Solutions*, pages 1–11, 2011. doi: 10.1007/s10291-011-0225-9.

I. S. Robinson. *Measuring the Oceans from Space: The principles and methods of satellite oceanography*. Springer, Praxis, 2004.

C. D. Rodgers. *Inverse Methods for Atmospheric Sounding*. World Scientific Publishing Co Pte Ltd, 2000.

N. Rodriguez-Alvarez, X. Bosch-Lluis, A. Camps, A. Aguasca, M. Vall-llossera, E. Valencia, I. Ramos-Perez, and H. Park. Review of crop growth and soil moisture monitoring from a ground-based instrument implementing the Interference Pattern GNSS-R Technique. *Radio Science*, 46:RS0C03, 2011.

A. M. Semmling, G. Beyerle, R. Stosius, G. Dick, J. Wickert, F. Fabra, E. Cardellach, S. Ribo, A. Rius, A. Helm, S. Yudanov, and S. d'Addio. Detection of Arctic Ocean tides using interferometric GNSS-R signals. *Geophys. Res. Letters*, 38:L04103, 2011. doi: 10.1029/2010GL046005.

R. Stosius, G. Beyerle, A. Helm, A. Hoechner, and J. Wickert. Simulation of space-borne tsunami detection using GNSS-reflectometry applied to tsunamis in the indian ocean. *Natural Hazards and Earth System Science*, 10(6):1359–1372, 2010.

R. N. Treuhaft, S. T. Lowe, C. Zuffada, and Y. Chao. 2-cm GPS altimetry over Crater Lake. *Geophysical Research Letters*, 22(23):4343–4346, 2001.

F. T. Ulaby, R. K. Moore, and A. K. Fung. *Microwave Remote Sensing - Active and Passive*, volume 2, Radar Remote Sensing and Surface Scattering and Emission Theory of *Remote Sensing*. Addison-Wesley, Boston, 1982.

J. Wu, S. Wu, G. Hajj, B. W., and S. Lichten. Effects of antenna orientation on GPS carrier phase. *Manuscripta Geodaetica*, 18(2):91–98, 1993.

G. Xu. *GPS: Theory, Algorithms and Applications*. Springer, 2007.

G. Xu and P. Knudsen. Earth Tide Effects on Kinematic/Static GPS Positioning in Denmark and Greenland. *Phys. Chem. Earth (A)*, 25:409–414, 2000.

C. Yang and A. Porter. GPS Multipath Estimation and Mitigation Via Polarization Sensing Diversity: Parallel Iterative Cross Cancellation. *Proceedings of the 18th International Technical Meeting of the Satellite Division of The Institute of Navigation (ION GNSS 2005)*, pages 2707–2719, 2005.

S. M. Yionoulis. The Transit Satellite Geodesy Program. *John Hopkins APL Technical Digest*, 19:36–42, 1998.

ISSN 1610-0956